

AD-A281 469



Semiannual Technical Report

Interface Properties of Wide Bandgap Semiconductor Structures

Supported under Grant #N00014-92-J-1477
Office of the Chief of Naval Research
Report for the period 1/1/94-6/30/94

DISTRIBUTION STATEMENT A

Approved for public release;
Distribution Unlimited

DTIC
ELECTE
JUL 12 1994
S B D

Robert F. Davis, Salah Bedair,* Jerry Bernholc,**
Jeffrey T. Glass and R. J. Nemanich**
c/o Materials Science and Engineering Department
*Electrical and Computer Engineering Department
and **Department of Physics
North Carolina State University
Campus Box 7907
Raleigh, NC 27695-7907

1329 94-21204



June, 1994

DTIC QUALITY INSPECTED 1

94 7 11 174

REPORT DOCUMENTATION PAGE			Form Approved OMB No. 0704-0188	
Public reporting burden for this collection of information is estimated to average 1 hour per response, including the time for reviewing instructions, searching existing data sources, gathering and maintaining the data needed, and completing and reviewing the collection of information. Send comments regarding this burden estimate or any other aspect of this collection of information, including suggestions for reducing this burden to Washington Headquarters Services, Directorate for Information Operations and Reports, 1215 Jefferson Davis Highway, Suite 1204, Arlington, VA 22202-4302, and to the Office of Management and Budget Paperwork Reduction Project (0704-0188), Washington, DC 20503.				
1. AGENCY USE ONLY (Leave blank)		2. REPORT DATE June, 1994		3. REPORT TYPE AND DATES COVERED Semiannual Technical 1/1/94-6/30/94
4. TITLE AND SUBTITLE Interface Properties of Wide Bandgap Semiconductor Structures			5. FUNDING NUMBERS uri41114a-01 1114SS N00179 N66005 4B855	
6. AUTHOR(S) Robert F. Davis and R. J. Nemanich				
7. PERFORMING ORGANIZATION NAME(S) AND ADDRESS(ES) North Carolina State University Hillsborough Street Raleigh, NC 27695			8. PERFORMING ORGANIZATION REPORT NUMBER N00014-92-J-1477	
9. SPONSORING/MONITORING AGENCY NAME(S) AND ADDRESS(ES) Sponsoring: ONR, 800 N. Quincy, Arlington, VA 22217-5660 Monitoring: Office of Naval Research Resider The Ohio State University Research Center 1960 Kenny Road Columbus, OH 43210-1063			10. SPONSORING/MONITORING AGENCY REPORT NUMBER	
11. SUPPLEMENTARY NOTES				
12a. DISTRIBUTION/AVAILABILITY STATEMENT Approved for Public Release; Distribution Unlimited			12b. DISTRIBUTION CODE	
13. ABSTRACT (Maximum 200 words) The structure and electronic properties of 1x1 and 2x1 H-terminated and clean C(100)2x1 surfaces have been calculated with <i>ab initio</i> molecular dynamics. A negative electron affinity was found for these surfaces; a positive electron affinity was found for the C(100) surface. In related growth calculations for ALE of diamond, the desorption of the HF molecule was found to be critical for H- and F-based growth mechanisms. Ni ₃ Si and Ni substrates were compared for the deposition of diamond films under the same conditions. Diamond (C) particles were obtained on the Ni ₃ Si, but only diamond-like C and graphite on the latter. C films deposited on via CVD. Field emission showed very high stability as well as high current densities. Step bunching occurred at the outset of the initial stage of SiC growth using C ₂ H ₄ /Si ₂ H ₆ ratios of 1, 2 or 10 and gas source (GS) MBE. Subsequent growth occurred via island formation (C ₂ H ₄ -rich) or step-flow (1:1 ratio). β-SiC or 6H-SiC deposited using high or 1:1 C/Si ratios, respectively. Unintentionally doped films are n-type with n=(0.2 - 1.0)×10 ¹⁷ cm ⁻³ . Similar atomic and hole concentrations of 5×10 ¹⁸ and 1.2×10 ¹⁸ cm ⁻³ , respectively, were measured in Al-doped, p-type films. Electrical contacts of Co exhibited rectifying behavior with n<1.06 and leakage currents of 2.0×10 ⁻⁸ at -10 V. After annealing at 1000°C for 2 min, ohmic-like behavior was observed as a result of interface reaction. Single crystals of AlN were grown on 6H-SiC substrates via sublimation from an AlN source. AlN films with essentially atomically flat surfaces, indicative of two-dimensional growth, were deposited on on-axis 6H-SiC(0001) surfaces at 1050°C via GSMBE. Island features, the coalescence of which caused defects and influenced film quality, were observed on the vicinal surface. AlN deposited on 6H-SiC(0001) possess a negative electron affinity. The surface Fermi level of the AlN is ~3.5 eV above the valence band maximum. I-V and C-V measurements of an MIS structure with AlN as the insulator revealed a 13.4 MV/cm breakdown field and a dielectric constant of ~14. Operation of the MIS devices at 300°C with only a slight reduction in the breakdown field to 13 MV/cm. A study of AlN for SAW devices has been initiated. GaN thin films have been grown on vicinal α(6H)-SiC(0001) and sapphire(0001) wafers via OMVPE. Photoluminescence revealed a donor bound exciton at 357.6 nm for films thicker than 1 μm. Peaks at 375-378 nm and 540 nm were also present. Al and CuGe contacts were deposited on Ge-doped GaN and both Mg-doped GaN and Ge-doped AlN, respectively. The former were ohmic with low contact resistivity and stable to 500°C. The latter were ohmic but with high resistivities. RIE has been used to dry etch GaN with Cl ₂ and BCl ₃ plasmas. Etch rates to 18 and 15 nm/min were achieved with the two respective chemicals. A special OMVPE system for deposition of InGaN-based films has been designed and fabricated. STEM, XRD, PIXIE and Raman scattering have revealed that GaP films grown at low temperatures via GSMBE contain excess P of ~0.6-2.0 at %.				
14. SUBJECT TERMS Ni ₃ Si, Ni, diamond, Si field emitters, β-SiC, 6H-SiC, step bunching, MBE, Co, ohmic contacts, AlN, GaN, InGaN, two-dimensional growth, step bunching, island growth, negative electron affinity, surface Fermi level, MIS device, breakdown field, dielectric constant, SAW devices, photoluminescence, donor bound exciton, Al contacts, CuGe contacts, RIE, Cl ₂ plasma, BCl ₃ plasma, GaP, STEM, XRD, PIXIE, Raman scattering, GSMBE			15. NUMBER OF PAGES 156	
			16. PRICE CODE	
17. SECURITY CLASSIFICATION OF REPORT UNCLAS		18. SECURITY CLASSIFICATION OF THIS PAGE UNCLAS		19. SECURITY CLASSIFICATION OF ABSTRACT UNCLAS
			20. LIMITATION OF ABSTRACT SAR	

Table of Contents

I.	Introduction	1
	Carbon-based Materials	
II.	Surface Structures and Electron Affinities of Clean and Hydrogenated Diamond C(100) Surfaces <i>Z. Zhang, M. Wensell, and J. Bernholc</i>	3
III.	Flourine-based Mechanisms for ALE Growth on Diamond (110) <i>M. G. Wensell, Z. Zhang and J. Bernholc</i>	23
IV.	Growth of Diamond Particles on a Ni ₃ Si Substrate <i>D. Tucker</i>	38
V.	Diamond Thin Film Coated Si Field Emitters <i>S. D. Wolter, M. T. McClure and J. T. Glass</i>	44
VI.	Effects of Gas Flow Ratio on the Growth Mode of Silicon Carbide by Gas-source Molecular Beam Epitaxy <i>S. Tanaka and R. F. Davis</i>	48
VII.	Growth and Characterization of Thin, Epitaxial Silicon Carbide Films by Gas-source Molecular Beam Epitaxy <i>R. S. Kern and R. F. Davis</i>	54
VIII.	Chemistry, Microstructure, and Electrical Properties at Interfaces between Thin Films of Cobalt and Alpha (6H) Silicon Carbide (0001) <i>L. Porter and R. F. Davis</i>	62
	Nitrogen-based Materials	
IX.	Native Defects in Wurtzite GaN and AlN <i>P. Boguslawski, E. Briggs, T. A. White, M. G. Wensell and J. Bernholc</i>	76
X.	Growth of Aluminum Nitride Single Crystals Via Sublimation Method <i>C. Balkas and R. F. Davis</i>	82
XI.	Initial Stage of Aluminum Nitride Film Growth on 6H-Silicon Carbide by Plasma-Assisted, Gas-source Molecular Beam Epitaxy <i>S. Tanaka and R. F. Davis</i>	88
XII.	Properties of Heteroepitaxial AlN/SiC Interface <i>M. C. Benjamin and R. J. Nemanich</i>	94
XIII.	Application of Epitaxial Aluminum Nitride (AlN) in Metal-Insulator-Semiconductor Structures <i>C. Wang and R. F. Davis</i>	102
XIV.	Application of Epitaxial AlN Films in Surface Acoustic Wave Devices <i>C. Wang and R. F. Davis</i>	107
XV.	Growth and Characterization of GaN Thin Films Grown by OMVPE <i>W. Weeks and R. F. Davis</i>	112
XVI.	Luminescence Studies of the GaN, AlN and Their Solid Solutions <i>B. Perry and R. F. Davis</i>	119
XVII.	Contact Formation in GaN and AlN <i>L. Smith and R. F. Davis</i>	125
XVIII.	Reactive Ion Etching of GaN, AlN and InN <i>K. Gruss and R. F. Davis</i>	137

XIV.	Growth System for the Metalorganic Chemical Vapor Deposition of InN and InGaN Solid Solutions for Optical Semiconductor Device Applications <i>D. Hanser and R. F. Davis</i>	144
	Phosphorous-based Materials	
XV.	Determination of Excess Phosphorous in Low-Temperature GaP Grown by Gas Source Molecular Beam Epitaxy <i>Y. He, and S. Bedair</i>	149
XVI.	Distribution List	156

Accession For	
NTIS GRA&I	<input checked="checked" type="checkbox"/>
DTIC TAB	<input type="checkbox"/>
Unannounced	<input type="checkbox"/>
Justification	
By	
Distribution/	
Availability Codes	
Dist	Avail and/or Special
A-1	

I. Introduction

Heteroepitaxy is the growth of a crystal (or a film) on a foreign crystalline substrate that determines its orientation. Such oriented growth requires that lattice planes in both materials have similar structure. In general, an epitaxial relationship is probable whenever the orientation of the substrate and overgrowth produces an interface with a highly coincident atomic structure having low interfacial energy relative to a random arrangement.

During the past decade, nonequilibrium techniques have been developed for the growth of epitaxial semiconductors, superconductors, insulators and metals which have led to new classes of artificially structured materials. In many cases, the films were deposited on substrates having a different chemistry from that of the film, and heteroepitaxy was achieved. Moreover, layered structures with a periodicity of a few atomic layers have also been produced by the sequential heteroepitaxial deposition of a film of one type on another. Metastable structures can be generated which possess important properties not present in equilibrium systems. A consideration of the materials under consideration for next generation electronic and optoelectronic devices, e.g., the III-V nitrides show that only a few of them can currently be grown in bulk, single crystal form having a cross-sectional area of $>3\text{cm}^2$. Thus other, commercially available substrates must be used. This introduces a new set of challenges for the successful growth of device quality films which are not present in homoepitaxial growth and which must be surmounted if these materials are to be utilized in device structures.

In addition to providing structures which do not exist in nature, applications of advanced heteroepitaxial techniques permit the growth of extremely high quality heterostructures involving semiconductors, metals, and insulators. These heterostructures offer the opportunity to study relationships between the atomic structure and the electrical properties of both the film itself and the interface between the two dissimilar materials. They also allow the study of epitaxial growth between materials exhibiting very different types (ionic, covalent, or metallic) of bonding.

While the potential of heteroepitaxial deposition has been demonstrated, significant advances in theoretical understanding, experimental growth and control of this growth, and characterization are required to exploit the capabilities of this process route. It is particularly important to understand and control the principal processes which control heteroepitaxy at the atomic level. It is this type of research, as well as the chemistry of dry etching via laser and plasma processing, which forms the basis of the research in this grant.

The materials of concern in this report are classified as wide bandgap semiconductors and include diamond, the III-V nitrides, SiC, GaP and AlP. The extremes in electronic and thermal properties of diamond and SiC allow the types and numbers of current and conceivable applications of these materials to be substantial. However, a principal driving

force for the interest in the III-V nitrides and GaP and AlP is their potential for solid-state optoelectronic devices for light emission and detection from the visible through the far ultraviolet range of the spectrum.

The principal objectives of the research program are the determination of (1) the fundamental physical and chemical processes ongoing at the substrate surface and substrate/film interface during the heteroepitaxial deposition of both monocrystalline films of the materials noted above, as well as metal contacts on these materials, (2) the mode of nucleation and growth of the materials noted in (1) on selected substrates and on each other in the fabrication of multilayer heterostructures, (3) the resulting properties of the individual films and the layered structures and the effect of interfacial defects on these properties, (4) the development and use of theoretical concepts relevant to the research in objectives (1-3) to assist in the fabrication of improved films and structures and (5) the determination of process chemistry which leads to the laser assisted and plasma etching of these wide bandgap compound semiconductors.

This is the fourth bi-annual report since the initiation of the project. The following sections introduce each topic, detail the experimental approaches, report the latest results and provide a discussion and conclusion for each subject. Each major section is self-contained with its own figures, tables and references.

Carbon-based Materials

II. Surface Structures and Electron Affinities of Clean and Hydrogenated Diamond C(100) Surfaces

Z. Zhang, M. Wensell, and J. Bernholc

Department of Physics

North Carolina State University

Raleigh, North Carolina 27965-8202

Abstract

The structure and electronic properties of the 1x1 and 2x1 H-terminated and the clean C(100) 2x1 surfaces have been calculated with *ab initio* molecular dynamics. Stable 2x1 structures were found for both clean and monohydride surfaces. The 1x1 dihydride phase was found to be energetically unfavorable relative to H₂ desorption, although a local minimum could be found. The stability of the 1x1:2H phase was studied by simulated annealing at 300K, resulting in a canting of the dihydride pairs. The 1x1:2H and 2x1:H structures were found to have a negative electron affinity. However, a positive electron affinity was found for the clean C(100) surface.

Introduction

Among the three low-index surfaces of diamond, only the (100) orientation sustains high quality growth of homoepitaxial and heteroepitaxial films[1-5]. The flatness of the grown surfaces in this direction could be on a nanometer-to-micrometer scale, making C(100) a good candidate for theoretical modeling. The C(100)(2x1):H surface has been found to have a negative electron affinity (NEA), a property that has strong technical and theoretical appeal. Thus, the C(100) surface has recently attracted more theoretical and experimental attention.

Normally, a polished C(100) surface shows a 1x1 LEED pattern when heated from 500K to 700K in an UHV environment. At temperatures above 1300 °K the surface reconstructs to a 2x1 structure[6]. The 2x1 phase is believed to be either monohydride or bare surface. While no consensus has been reached on the observed 1x1 structure, the surface has been suggested as either a dihydride or a disordered phase. In their ESD-TOF, Hamza and co-workers[6] found two distinct velocities of ions emerging from the 1x1 surface, indicating the existence of CH₂ dihydride unit. The slower peak, which persists to higher temperatures (~1530K) after the 2x1 reconstruction are attributed to the hydrogen desorption from monohydride pairs. Oxygen was also found on the 1x1 surface by both ESD-TOF and Auger techniques and appears to inhibit the ability of the surface to reconstruct[6] [7]. Previous theoretical efforts have been aimed mainly at resolving the atomic and electronic structures of the 1x1 and 2x1 surfaces. A relatively common agreement on the 1x1 phase is that full dihydride coverage cannot be responsible for the observed structure[8, 9]. The calculated steric repulsions of the dihydride surface are large, although a local minimum energy structure can still be found[10, 11]. A more stable 1x1 structure consisting of alternating dihydride and

monohydride C(100)1x1 was obtained by Frauenheim *et al* [12] using semiempirical SA-MD calculations. The 2x1 phase was found to be stable with or without adsorbed hydrogen. The MD simulations by Frauenheim *et al* indicates that the 2x1 monohydride structure is stable around CVD growth temperatures $\sim 1200\text{K}$ [12]. However, Lee and Apai[13] recently found from their EELS measurements of the C-H vibrations modes, that H readily desorbs from C(100) surface upon heating to $\sim 1473\text{ K}$. A better understanding about the role of hydrogen on this surface is needed.

Certain diamond surfaces may exhibit negative electron affinity (NEA), thus electrons at the conduction band edge can be emitted into vacuum. This effect could potentially make diamond useful in applications such as cold cathode emitters and UV detectors. NEA for diamond surfaces has been observed in photoemission spectra when a distinct peak appears at low energy end of the valence band[14]. For C(111) diamond surfaces, negative electron affinities were found to be associated with the 1x1 phase, whereas the (2x1) reconstructed phase exhibited a positive electron affinity[15]. Recently in their UV photoemission experiments, van der Weide and Nemanich[7] found that the hydrogenated C(100)2x1 surface exhibits negative electron affinity while the C(100)1x1 does not. In general, the measured electron affinities may have contributions from two relatively different mechanisms - band bending (the space charge) and surface dipole adjustment. Band bending occurs over a range of about 1000\AA around the surface and is due to the occupation of the surface states by the impurity carriers in the solid[16, 17]. Surface dipole adjustment is a variable on the atomic scale and strongly depends on the surface structures and adsorption species. In this paper we have studied the effect of hydrogen adsorption on electron affinity, leaving aside the space charging effect. The calculated electron affinity, in conjunction with experimental measurements, can also give information about surface structures[7].

Previous theoretical studies of these surfaces have mostly used empirical or semiempirical methods[9, 10] [11, 12, 18, 19]. However, there are some disagreement

among the various methods about surface geometries and surface electron states. We have performed large scale LDA calculations using the *ab initio* pseudopotentials and the Car-Parrinello[20] method for C(100):2x1(bare), C(100)(2x1):H and C(100)(1x1):2H surfaces, to study their electron affinities and resolve the surface geometries.

Methodology

The total energy $E[\{\psi_i\}, \{\bar{R}_I\}]$ of a system is expressed as

$$E[\{\psi_i\}, \{\bar{R}_I\}] = \sum_i^{\text{occ}} \int d\bar{r} \psi_i^*(\bar{r}) \left(-\frac{1}{2} \nabla^2 \right) \psi_i(\bar{r}) + \int d\bar{r} V^{\text{ext}}(\bar{r}) n(\bar{r}) + \frac{1}{2} \iint d\bar{r} d\bar{r}' \frac{n(\bar{r}) n(\bar{r}')}{|\bar{r} - \bar{r}'|} \\ + E^{\text{xc}}[n] + \frac{1}{2} \sum_{I \neq J} \frac{Z_I Z_J}{|\bar{R}_I - \bar{R}_J|}$$

Here $\{\psi_i\}$'s are the one-electron wavefunctions which are expanded in plane-waves and subject to orthonormality constraints. $\{\bar{R}_I\}$'s are the atomic coordinates. In the Car-Parrinello[20] formalism both $\{\bar{R}_I\}$'s and $\{\psi_i\}$'s vary simultaneously under the conditions that $\{\bar{R}_I\}$'s are on the Born-Oppenheimer surface and $\{\psi_i\}$'s orthonormalized. Thus the forces on atoms are

$$-\frac{\partial E}{\partial \bar{R}_I}$$

and the "forces" on the electron degrees of freedom are

$$-\frac{\delta E}{\delta \psi_i}$$

. This method has been proven to be very efficient for *ab initio* MD and total energy minimization[21, 22].

Soft-core, norm-conserving pseudopotentials for hydrogen and carbon were generated by a modified Hamann procedure[23, 24]. The energy cutoff in the plane wave expansion was 35 Rydbergs. The diamond surfaces were modeled by using supercells containing ten layers of diamond. The slabs were separated by 10 Å of vacuum in order

to avoid interactions between slab surfaces. Since both sides of the slab have the same surface, it is equivalent to five layers of the actual surface. We believe that this is a more accurate choice than passivating one side of the slab with hydrogen (a method often used to model a thicker slab), because it avoids dipole interactions between surfaces due to differences in their workfunctions. The clean C(100)2x1 surface supercell contains a total of 80 carbon atoms with eight atoms per layer. The monohydride C(100)2x1:H surface was modeled by a supercell containing ten layers of diamond with twelve carbon atoms per layer. One hydrogen atom was attached to every surface carbon atom according to the C(100)2x1:H stoichiometry. For the C(100)1x1:2H dihydride surface, two hydrogen atoms were attached to each of the nine surface carbon atoms. Due to the sizes of our supercells, only Γ point sampling was used. Starting from an estimated structure, the zero temperature geometries were obtained by steepest descents and/or fast-relax methods of ion dynamics[25]

The electron affinity of a semiconductor surface is defined as the energy separation between the conduction band minimum inside the solid and the vacuum level. Normally, two factors may affect the electron affinity value: the surface dipole moment at the first few atomic layers of the surface and the space-charge due to the occupation of the surface states by impurity carriers in the bulk. The effect of hydrogen adsorption on the positions of bulk energy levels relative to the vacuum level can be directly analyzed using the present calculations. However the space-charge, which extends hundreds of angstroms from the surface and depends on bulk doping, must be studied by a different formalism.

By definition, the electron affinity

$$\begin{aligned}\chi &= v(\infty) - E_C \\ &= v(\infty) - E_C - V_{\text{bulk}} + V_{\text{bulk}} \\ &= D - (E_C - V_{\text{bulk}}).\end{aligned}$$

Here, $(E_c - V_{\text{bulk}})$ is the position of the conduction band edge relative to the bulk averaged electrostatic potential (V_{bulk}) which is purely a bulk property. And $D = V(\infty) - V_{\text{bulk}}$ is defined as the surface dipole strength which determines the relative positions of the bulk electron states and the vacuum level[26]. To ensure the proper convergence, we computed the position of the valence band maximum E_v using a bulk diamond calculation, which gives the value of $(E_v - V_{\text{bulk}})$. Then E_c is determined by using the experimental band gap value (5.47 eV) since LDA underestimates the bandgap value. The dipole strength D can be obtained directly from the difference of the electrostatic potentials across the surfaces. It is the electrostatic charge distributions at the surface that are responsible for the different dipole strengths. More illustratively, D could also be calculated by integrating the one dimensional Poisson's equation:

$$d^2V/dz^2 = -4\pi\rho(z)$$

where $\rho(z)$ is the total charge (electronic and nuclear) averaged in the plane at z .

Results and Discussions

Surface geometries and energetics

Both clean and monohydride surfaces can have stable 2×1 structures (Figure 1), but the C-C dimer bond length was shorter on a clean surface (1.38\AA) than on a monohydride surface (1.63\AA). This difference is expected when compared to typical C-C double and single bond lengths. Much larger vertical relaxations were found for the clean surface than for the hydrogenated surfaces. For all three surfaces, spacing between the first and second layers was compressed (by -26%, -10% and -6.7% respectively), while spacing between second and third layers was stretched (+5.6%, +1.1% and +2.2%) (Table 1). However only small displacements (less than 0.02\AA) from ideal bulk positions

were found on the third and fourth layers - an indication that the ten-layer slab used in the calculation is adequate for studying the physics of these surfaces. Due to steric repulsion, the hydrogen atoms tend to avoid each other. This is the reason for the change in angle between the C-H bond and the surface normal on the monohydride surface from its starting value 54.7° to its relaxed value of 23.1°

On the dihydride surface the steric repulsion is even stronger. Starting from symmetric initial positions and using the steepest descents method, a symmetric dihydride structure was obtained (Figure 2a). The stability of the dihydride surface was then examined by finite temperature simulation where the surface was heated to 300K for about 0.02 ps (~ 3 times the period of C-H vibrations). During the simulation the hydrogen atoms deviated from the symmetric positions but no dissociation from the surface was observed. A subsequent steepest decent calculation led to a canted and twisted structure which is lower in energy than the symmetric structure by 0.12 eV per 1×1 unit. Similar twisting of the dihydride pairs was found by Yang and D'Evelyn[27, 28]. Due to the prohibitive computational cost, we did not attempt higher temperature simulations or a search for a global minimum for the dihydride surface.

Hydrogen desorption from the surfaces was analyzed by using the following end-point energetics:

$$\delta E = (E_{\text{substrate}} + E_{\text{H atom}}) - E_{\text{system}}$$

Here, E_{system} and $E_{\text{substrate}}$ are the energies of the fully relaxed hydrogenated surfaces (C:(100) 2×1 :H or C(100) 1×1 :2H) and surfaces with less hydrogen (clean C(100) 2×1 or C(100) 2×1 :H). $E_{\text{H atom}}$ is the energy of a free hydrogen atom, 13.03 eV within the LDA approximation. The δE then reflects the strength of hydrogen binding. In Table II, we compare our calculated δE 's with existing works. Large differences (4.36 eV/ H atom) in the δE 's were found between the monohydride and dihydride surfaces. The dihydride

surface is energetically unfavorable by 2.3 eV/H₂ with respect to H₂ desorption although it is still favored relative to atomic H by 1.13 eV. The much smaller δE for the dihydride surface implies a lower desorption energy than the monohydride. This is in qualitative agreement with the ESD-TOF measurement[6] [7]. However the true binding energy should be the energy required to remove a single atom from the surface. This depends on the specific surface site and surface coverage. Moreover, there will be energy barriers for the various desorption paths, thus dynamic simulations are necessary to make quantitative correlation to the measured desorption temperatures.

Accurate experimental measurements of hydrogen coverage on diamond (100) surfaces are not currently available, possibly due to experimental difficulties[6, 28]. In the cases of Si(100) surfaces, Cheng and Yates found a saturation coverage of 1.9ML (1 ML is defined as one H per surface Si atom) and suggested that the Si(100)1x1 surface was a disordered phase containing monohydride, dihydride, and trihydride structures. Compared to silicon, the diamond lattice is 34% smaller. Thus, the larger steric repulsion will inhibit high coverage density. Yang and D'Evelyn[27, 28] suggested that a disordered dihydride with local (2n+1)x1 structure will most likely give rise to a 1x1 LEED pattern[6]. This model eliminates the large repulsion between two adjacent dihydride units and implies a maximum coverage of 1.33 ML at which a 3x1 structure results. In principle the fully covered surface (the dihydride) can exist at zero temperature. Although the repulsion is the highest, calculations indicate that it is still lower in energy relative to the free atom and bare surface, and that a barrier exists for H₂ desorption. However, the conditions required for this phase to occur may be very different from normal laboratory conditions.

Electronic Structure

The electronic wavefunctions were analyzed by examining their Millikan populations and plane-averaged square modulus. Information on the charge distribution

and the bond orientations could be determined from the Millikan populations. Surface states could be identified by the wavefunctions being heavily weighted at the surface region.

Figures 3a&b describe the electronic structures of the clean and monohydride surfaces. The bare surface is characterized by having both filled and empty surface states in the band gap. They mainly consist of π bonding and anti-bonding orbitals on the dimer atoms. The energy separation between the filled and empty surface states is 1.5 eV. For the monohydride surface, no occupied surface states were found in the band gap. The C-H bonding states lie about 4 eV below VBM. However, a broad band of unoccupied states, which are related to the C-H anti-bonding, were found to be between 1.5 to 2.5 eV below the conduction band edge. Due to the well known inadequacy of LDA in describing the excited states, the position of these states cannot be precisely determined.

In their tight-binding calculation for the bare C(100)(2x1) surface Davidson *et al* [11] found a 2 eV gap between the highest occupied and the lowest unoccupied states, similar to our value of 1.5 eV. However, Yang *et al*[9] and Mehandru *et al*[10] found the bare surface to be nearly metallic. While the unoccupied states inside the band gap didn't appear in the empty band gap of another theoretical monohydride surface calculation [10], our result is very similar to theoretical and experimental findings on the monohydride silicon Si(100)2x1:H surface. In their STM spectroscopy, Hammers *et al*[29] attributed the peak 1.0 eV above E_f to the Si-H anti-bonding states that were computed by the empirical tight-binding method by Ciraci *et al*[30]. Although a strong C-H bond means large separation between bonding and anti-bonding states (typically ~9 eV in small molecules such as CH₄), the interactions on the surface may broaden the band so that the empty states drop below the bulk the conduction band edge.

Experimentally for the 2x1 diamond surface, Hamza *et al*[6] found occupied states over a 1.5 eV range of the energies above the valence band maximum (VBM) and

no empty states from 1.2 to 5.5 eV above the Fermi level. Neither of the present calculations for the ideal 2x1 surface (clean and monohydride) have an electronic structure that exactly matches experiment. Since there is a clear indication of occupied gap states, we conclude that the actual surface is at least partially bare. Based on their tight-binding calculations, Davidson *et al*[11] have shown that a half-hydride structure, which has partially filled gap states, would best fit the photoemission data. Recently Lee and Pai using EELS measurements found that hydrogen easily desorbs from C(100) surface upon heating to 1473K[13]. We should not expect the calculations for the perfect surfaces to exactly correlate with the measurements on the actual samples which have defects and steps.

The electronic structure of the symmetric dihydride surfaces is shown in Figure 4. The highest occupied states are surface states induced by hydrogen adatoms. These states almost coincide energetically with the valence band maximum of diamond. A broad band of empty surface states exist about 0.8 eV above the E_v (or the highest occupied states). They are in strong resonance with the conduction band. Due to the Γ -point sampling, the detailed dispersion relation is not available. Although the interaction is strong, the surface remains insulating. This is in qualitative agreement with the tight-binding calculations of Davidson *et al*[11]. Gavrilenko[19], however found the dihydride surface to be metallic. Regardless these findings, the existence of a dihydride phase remains controversial.

Electron Affinity

In Figure 5, we plot the plane-averaged self-consistent potentials for the bare, monohydride, and the symmetric dihydride surfaces. In principle the vacuum level should be the same for all the surfaces, each of which may have different potential barriers. But for analytical convenience we align the potentials inside the bulk, thus the vacuum levels are different for each of the three surfaces. The potentials agree well

inside the bulk and flatten out in the vacuum region, indicating good convergence for the supercell size and the vacuum used. The bare C(100)(2x1) surface has the largest potential barrier (i.e. largest surface dipole D). Its vacuum level lies above the conduction band edge E_c , giving an electron affinity of +0.8 eV. Compared to the bare C(100)(2x1) surface, the hydrogenated surfaces have less electronic charge extending into the vacuum because hydrogen has saturated the dangling bonds. The net effect is that of an additional dipole layer in the opposite direction of the surface dipole D . Hence the total potential barrier is reduced. The vacuum levels of both the monohydride and the dihydride surfaces are below the conduction band. The calculated electron affinities are -2.2 eV and -3.4 eV respectively.

In the UV photoemission measurement, van der Weide and Nemanich[7] found that the NEA appears when the C(100) surface was annealed at 1050C°, a temperature which coincides with the 2x1 reconstruction. While hydrogen cannot be seen in the UV measurement, from comparison of experimental NEA with our calculated results, we conclude that hydrogen is present on the 2x1 surface. In a more recent experiment, Baumann et al[7] confirmed the presence of surface hydrogen since exposure of the 2x1 surface to atomic hydrogen did not affect the UV result. As for the 1x1 surface, on which UV measurement does not show a NEA peak and oxygen was found to be present, the structure is unclear.

Conclusions

Stable structures have been found for both 2x1 H-terminated and clean surfaces. The 1x1 dihydride structure is energetically unfavorable due to the steric repulsion of the hydrogen atoms, while a local minimum still exists. Negative electron affinities have been calculated for both C(100)2x1:H and C(100)1x1:2H surfaces. However the clean C(100)2x1 surface exhibits a positive electron affinity. The difference in the electron affinities is attributed to the hydrogen induced dipole layers on the surfaces.

Acknowledgment

This work was supported in part by the National Science Foundation through grants DMR-9204285 and the University Research Initiatives.

References

1. Wolter, S.D., *et al.*, Appl. Phys. Lett., 1993. **62**: p. 1215.
2. Tsuno, T., T. Imai, Japanese Journal of Applied Physics, 1991. **30**(5).
3. Rudder, R.A., *et al.* *Selected-Area Homoepitaxial Growth and Overgrowth On Si Patterned Diamond Substrates*. in *Second International Conference, New Diamond Science and Technology*. 1990. Washington, DC:
4. Badzian, A.R., *et al.* *Growth Sectors of CVD diamond*. in *New Diamond Science and Technology*. 1990. MRS.
5. Sutcu, F.L., *et al.*, J. Appl. Phys., 1992. **60**: p. 1685.
6. Hamza, A.V., G.D. Kubiak, and R.H. Stulen, Surf. Sci., 1990. **237**: p. 35.
7. Weide, J.v.d., *et al.*, to be submitted to PRL, 1993. .
8. Yang, Y.L. and M.P. D'Evelyn, J. Am. Chem. Chem. Soc., 1992. **114**(8): p. 2796.
9. Yang, S.H., D. A. Drabold and J. B. Adams, Phys. Rev. B, 1993. **48**(8): p. 5261.
10. Mehendru, S.P. and A.B. Anderson, Surf. Sci., 1991. **248**: p. 369.

11. Davidson, B.N. and W.E. Pickett, preprints, 1993. .
12. Frauenheim, T., *et al.*, Phys. Rev. B, 1993. 48(24): p. 8189.
13. Lee, S.-T. and G. Apai, Phys. Rev. B, 1993. 48: p. 9556.
14. Himpsel, F.J., *et al.*, Phys. Rev. B, 1979. 20(2): p. 624.
15. Pate, B.B., Sur. Sci., 1985. 165: p. 83.
16. Garrett, C.G.B. and W.H. Brattain, Physical Review, 1955. 99(2): p. 376.
17. Pate, B.B., *et al.*, J. Vac. Sci. Technol., 1980. 17(5): p. 1087.
18. Zheng, X.M. and P.V. Smith, Surf. Sci., 1991. 256: p. 1-8.
19. Gavrilenko, V.I., Phys. Rev. B, 1992. 47(15): p. 9556.
20. Car, R., Phys. Rev. Lett., 1985. 55: p. 2471.
21. Zhang, Q.-M., J.-Y. Yi, and J. Bernholc, Phys. Rev. Lett., 1991. 66: p. 2633.
22. Iarlori, S., *et al.*, Phys. Rev. Lett., 1992. 69(20): p. 2947.
23. Hamann, D.R., M. Schluter, and C. Chiang, Phys. Rev. Lett., 1979. 43: p. 1494.

24. Bachelet, G.B., D.R. Hamann, and M. Schluter, *Phys. Rev. B*, 1982. **26**: p. 4199.
25. Wang, C., Q.-M. Zhang, and J. Bernholc, *PRL*, 1992. **69**(26): p. 3789.
26. Zangwill, A., *Physics at Surface*. 1988, Cambridge University Press. 59.
27. Yang, Y.L. and M. D'Evelyn, *J. Vac. Sci. technol. A*, 1991. **10**(4): p. 978.
28. Yang, Y.L., *et al.*, *Thin Solid Films*, 1993. **225**: p. 203-211.
29. Hamers, R.J., P. Avouris, and F. Bozso, *Phys. Rev. Lett.*, 1987. **59**(18): p. 2071.
30. Ciraci, S., *et al.*, *Phys. Rev. B*, 1984. **30**(2): p. 711.

Table I. Diamond Surface Geometries

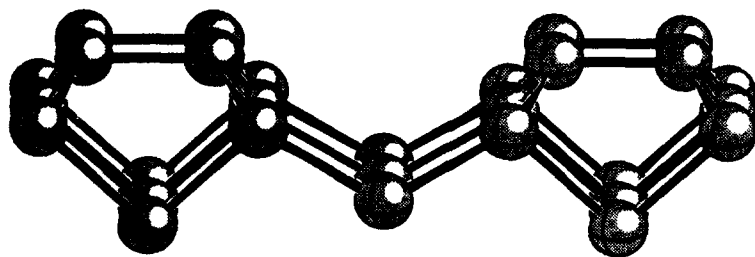
	2x1:clean	2x1:H	1x1:2H (sym)	1x1:2H (canted)
$r_{\text{dimer}}(\text{\AA})$	1.377	1.628	-	-
$r_{\text{CH}}(\text{\AA})$	-	1.112	1.056	1.04 - 1.13 *
$\alpha(\text{dimer-H})$	-	113.1°	-	-
$\theta(\text{H-C-H})$	-	-	84.72°	93° - 96° *
$\Delta x_1(\text{\AA})$.65	.80	.83	-
$\Delta x_2(\text{\AA})$.94	.90	.91	-
$\Delta x_3(\text{\AA})$.87	.89	.89	-

*Fluctuation range during finite temperature simulation

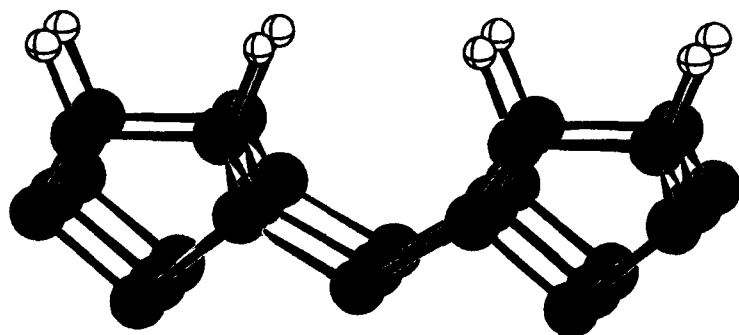
Table II. Energetics of Hydrogen Binding

Surface	Zheng, <i>et al</i>	Mehandru, <i>et al</i>	Yang, <i>et al</i>	Yang	This work
$\delta E_{\text{mono}}(\text{eV})$	6.32	6.63	3.27	6.18	5.49
$\delta E_{\text{di}}(\text{eV})$	4.11	-	1.19	-	1.13

Figure 1, the 2x1 structures



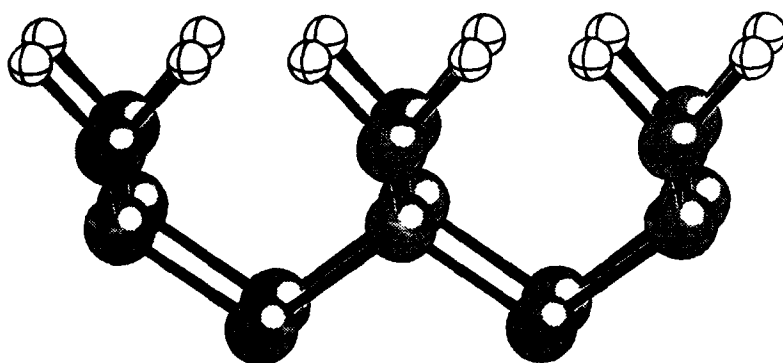
a) The clean C(100) diamond surface



b) Hydrogenated C(100) diamond surface

Figure 2, the 1x1 structure

symmetric



canted

(after simulated annealing to 300K)

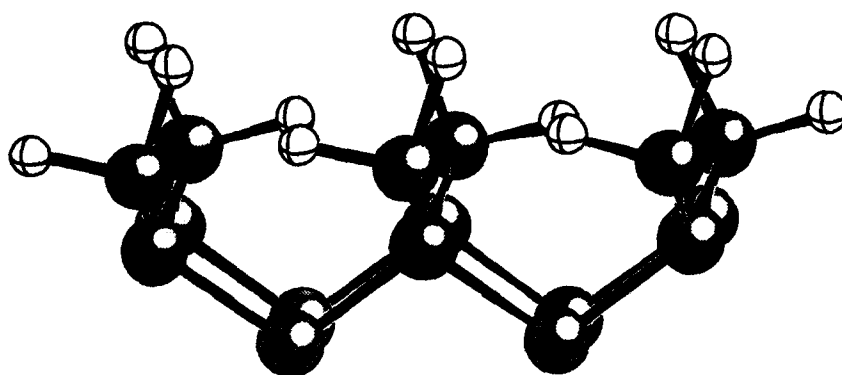
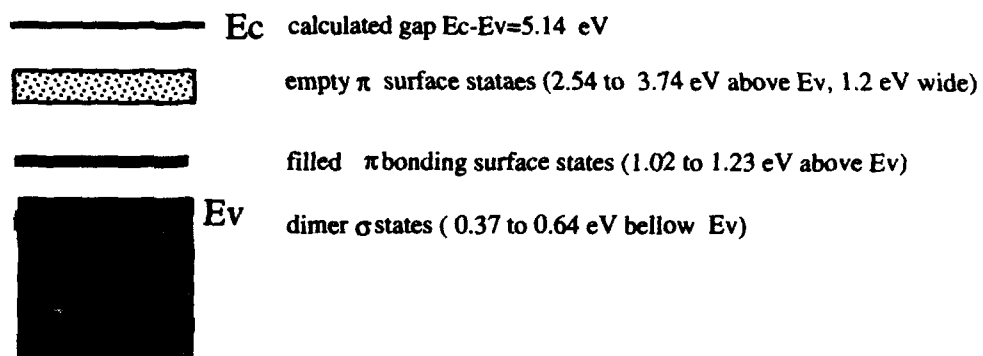


Figure 3. Electronic structure of bare C(100)(2x1) and C(100)(2x1):H surface

a) Bare C(100)(2x1)

The C(100) Bare Surface



b) C(100)(2x1):H surface

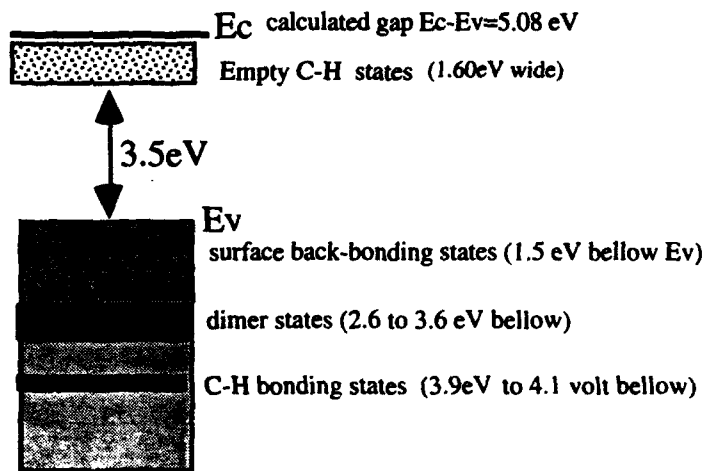


Figure 4. Electronic structure of dihydride C(100)(1x1):2H surface

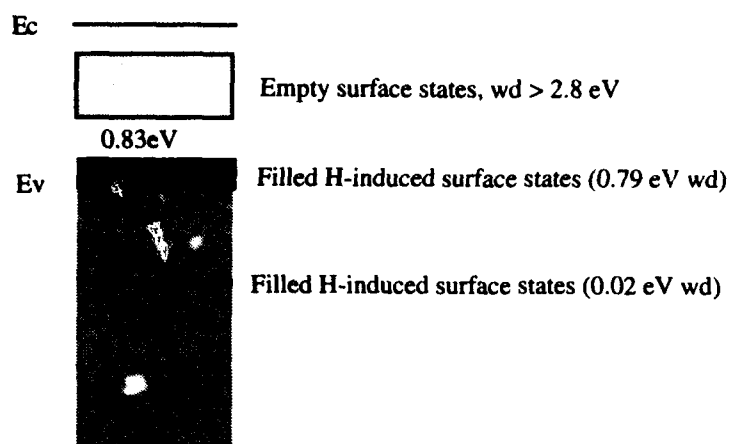
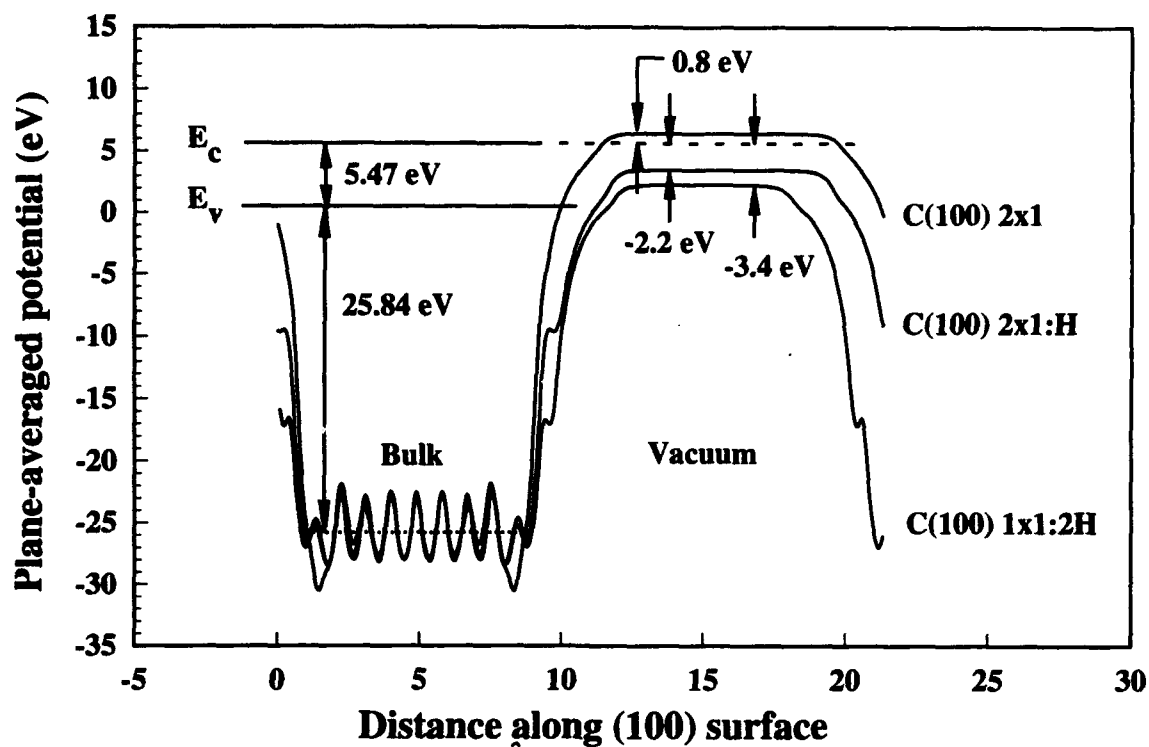


Figure 5. Plane-Averaged Self-Consistent Potential



III. Flourine-based Mechanisms for ALE Growth on Diamond (110)

M.G. Wensell, Z. Zhang and J. Bernholc

Department of Physics
North Carolina State University
Raleigh, North Carolina 27695-8202

ABSTRACT

Endpoint energetics for atomic layer epitaxial growth mechanisms have been studied using *ab initio* molecular dynamics. Hydrocarbons and flourcarbons are the principle gas species used in the growth reactions. The mechanisms employ the switching of H- and F-terminated terminated (110) surfaces to yield self-limiting growth. The reaction of atomic and diatomic hydrogen with flourinated surfaces and the reaction of atomic and diatomic flourine with hydrogenated surfaces has also been studied. The desorption of the HF molecule was found to be crucial for H- and F-based growth mechanisms.

1. Introduction

Atomic layer epitaxial (ALE) growth has the promise of yielding high quality diamond films. An ALE process has the characteristic of depositing uniform layers onto a substrate via self-limiting reactions. This technique has been well-demonstrated for the growth of II-VI and III-V semiconductor thin films^{1,2}. For binary semiconductors, the formation of a polar bond in the solid and self-limiting adsorption of the precursor gases directly benefits from the difference in the electronegativity of the elements. However, these advantages do not exist to assist ALE growth of homogenous group IV semiconductors such as diamond. Methods have been proposed for ALE growth of silicon that rely on the sequential exposure of precursor gases to the substrate that result in alternating the adatoms terminating the surface³⁻⁵. Our efforts have been directed at identifying promising mechanisms for growing diamond films employing the alternating surface termination scheme with fluorine.

Previously, halogen-based mechanisms for ALE growth on diamond have been based on chlorocarbons as the precursor growth gas species. Here we propose three new ALE diamond growth mechanisms based on fluorine. The growth precursor gases are either C_2H_4 or C_2F_4 and are exposed to the C(110):F or C(110):H surfaces, respectively. These reactions result in the growth of a monolayer of diamond and the switching of the terminating surface adatoms from H to F or vice versa. We can thus define a bilayer growth per cycle mechanism using both growth reactions in sequence. Reaction of diatomic and ionic hydrogen with an F-terminated surface and reaction of diatomic and ionic fluorine with an H-terminated surface has also been studied. These reactions have the effect of switching the type of the terminating adatoms without growing a layer. Thus we can also define monolayer growth per cycle mechanisms using a combination of a growth reaction

and a switching reaction. The desorption of HF from the surface plays a key role in the energetics of all the reactions.

In our investigation, we have performed large-scale *ab initio* calculations using the Car-Parrinello method⁶ which combines the density-functional theory (DFT) with molecular dynamics. From the total energies yielded by DFT we have calculated the endpoint energetics of the proposed growth mechanisms.

2. Method

In the Car-Parrinello methodology, the electrons are described in the local density approximation with their wavefunctions expanded in a plane wave basis. The ions were modeled with soft-core, norm-conserving pseudopotentials. Pseudopotentials for carbon were generated using a modified Hamann procedure⁷ and the hydrogen and fluorine were generated using the Li and Rabii procedure⁸. Due to the lack of *p* electrons in the core, the *p* pseudopotential for fluorine is very deep. This requires choosing a cutoff that includes plane wave with kinetic energies smaller than 50 Ry. Pseudopotentials generated with the Li and Rabii method are optimized for this cutoff.

The diamond surfaces were modeled in supercells as slabs of 9–11 atomic layers separated by more than 10 Å of vacuum. The large amount of vacuum was necessary to avoid interactions between slab surfaces. The bottom layer of each slab was held fixed to perfect crystal lattice positions and the dangling bonds were passivated with hydrogen. The top layer of the slab was terminated with either hydrogen or fluorine adatoms. An example of a ten-layer fluorine-terminated diamond (110) surface is shown in Fig. 1. The gas-species

used in the growth mechanisms were modeled in supercells of 10 cubic Å volume containing a single molecule or atom. Ground state total energies were calculated for each slab and gas species by simultaneous relaxation of the atomic and electronic structure. These total energies are then used to determine the endpoint energetics in the mechanisms.

The endpoint energetics of a reaction are thus defined to be the total energies of a slab and the precursor gas species minus the total energies of the slab with a fully deposited layer and the desorbed gas species. In each supercell the total number of atoms of each element are conserved throughout each reaction. Barriers to growth due to orientation of the precursor gas species relative to surface sites are not included in the scope of this paper.

3. Pseudopotentials

Modeling of fluorine previously required a prohibitively high cutoff of the the plane wave kinetic energy. Fluorine required as much as 100 Ry under the Hamman pseudopotential scheme. Using the Li and Rabii method, we have chosen the initial cutoff to be 50Ry. For hydrogen a Li pseudopotential was optimized for 50 Ry. Carbon was modeled using a Hamman pseudopotential that has been found to be well converged for cutoff energies less than 40 Ry and thus should be suitable for our chosen cutoff of 50 Ry.

Computational tests were performed by modeling and comparing the binding energies and vibrational frequencies of several gas species to be used in the reactions. The data from these tests are tabulated in tables 1-3. Good agreement with the molecular LDA calculations of Johnson *et al*⁹ was exhibited. The atomization energies agreed within 8%.

Vibrational frequencies were in close agreement with both molecular LDA and experimental data. Likewise, molecular geometries were also in good agreement.

4. Mechanisms

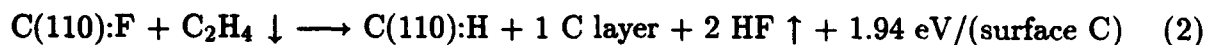
Recently, an ALE diamond growth process has been proposed¹⁰ involving the successive deposition of CH_4 and CCl_4 onto an initially chlorinated diamond (111) surface. From an elementary molecular bond strength analysis, the reaction energetics are found to be self-limiting. Below, we will discuss our results of *ab initio* molecular dynamics studies of this process. We found that while the reactions are energetically favorable, there are significant steric repulsions between Cl adatoms that could hinder the reactions from proceeding at practical rates. The steric repulsion are due to the fact that the Cl atom has a covalent radius of 0.99 Å which is much larger than the covalent radius of 0.77 Å for C atoms. Chlorine is more suitable for use in ALE growth mechanisms for Si because the covalent radius for Si is 1.17 Å. Fluorine has the advantage of having a covalent radius of 0.64 Å which reduces the steric repulsion between the adatoms on a diamond surface. Therefore, we would expect a lowering of the growth barriers relative to those found in Cl gas-species adsorption.

We have studied several reactions that when combined in appropriate sequences, are good candidates for ALE diamond growth mechanisms. Two reactions for growth of a monolayer of carbon are proposed. The first involves exposure of a C_2F_4 gas to a uniformly hydrogenated C(110) surface. The model assumes that addition of vinyl-like dimers occurs uniformly across the surface. The result is the adsorption of a monolayer of carbon, the

desorption of two HF molecules per C₂F₄ molecule, and an energy gain of 1.62 eV/(surface C). Similarly, we can model the symmetric counterpart of this reaction by switching the hydrogen and fluorine atoms in the reaction. Thus, in the second reaction, a C₂H₄ gas is exposed to a uniformly fluorinated surface resulting in the growth of a carbon monolayer, the desorption of two HF molecules per C₂H₄ molecule, and a similar energy gain of 1.94 eV/(surface C). The reactions can be detailed as



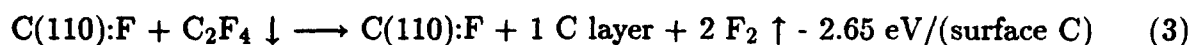
and



The differences in energy gain can be attributed to the differences in the covalent radii of the surface terminating adatoms. Since the energy gain is smaller for fluorine gas-species adsorption, the steric repulsion plays a role in the reaction but the favorable size of the fluorine adatoms prevents the repulsion from becoming a prohibitive barrier to adsorption. The desorption of HF is an important part of the reactions. Since the H-F bond is stronger than either the H-C or the C-F bond, the formation of this bond results in the large energy gain per surface carbon as the surface terminating adatoms are alternated. With these two reactions, one could combine them in to a two step cycle alternating the surface terminating adatoms and the incident gas-species. The reciprocal cycle would result in two layers of growth per cycle, but further reactions must be examined to show that the growth is self-limiting.

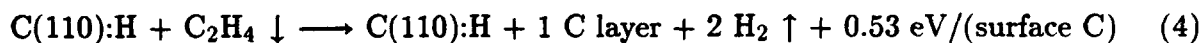
To study the self-limiting aspect of the reactions, we modeled reactions that would result in additional growth on uniformly covered surfaces where the surface terminating

adatoms are the same as those contained in the gas-species. For example, C_2F_4 continues to be exposed to the fluorinated surface that is the result of reaction (1). For continued growth on this surface, we would expect to see the desorption of two F_2 molecules per each C_2F_4 adsorbed. To achieve the growth of a layer of carbon using this reaction, we would have to add 2.65 eV per surface carbon atom to achieve growth. The reaction can be expressed as



As this is a very large barrier to the reaction, reaction (1) can be characterized as a self-limiting reaction in the sense that continued adsorption of C_2F_4 onto the completely fluorinated surface is very unfavorable energetically.

The self-limiting character of the second reaction was examined in a similar way. Continued exposure of C_2H_4 to the completely hydrogenated surface would require the desorption of two H_2 molecules per each C_2H_4 adsorbed. To achieve a monolayer of carbon using this reaction, an energy gain of 0.53 eV per surface carbon atom is realized. The reaction can be expressed as



At first glance, it would appear that reaction (4) is not a self-limiting reaction due to the slight energy gain. However, to gain energy by addition of C_2H_4 to $C(110):H$ a two-center reaction must take place. When the vinyl-like dimers are formed, we assume that the dimer's carbon-carbon double bond breaks and that H_2 formation occurs simultaneously. Experimentally, it has been shown that C_2H_4 does not react with hydrogen terminated diamond surfaces in the absence of plasma or glow discharge. Thus, both growth reactions

are most likely self-limiting and when used in an alternating cycle will form a bi-layer growth per cycle ALE mechanism.

In addition to the two main growth reactions, reactions of atomic and diatomic fluorine and hydrogen gas species with an oppositely terminated diamond (110) surface have been investigated. These reactions have the effect of alternating the termination adatom type with a desorption of HF molecules as the "waste" gas. The first reaction is that of F_2 with a uniformly hydrogenated (110) surface:



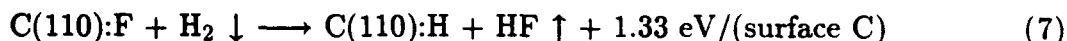
This illustrates the substantial energy gain realized when the hydrogen adatoms are stripped off of the surface when the HF bond is formed. With the breakage of the F_2 bond, the remaining fluorine atom replaces the hydrogen adatom as the terminating adatom. Note that using endpoint energetics, the reaction simulated is between the completely hydrogenated and completely fluorinated surface. Thus, any steric repulsions between adatoms is taken into account. One would expect the replacement of a small adatom with a larger adatom to be subject to barriers due to steric repulsion. With the substantial energy gain realized, we can assume that these barriers do not play a significant role in this reaction.

Similarly, the reaction of a flux of atomic F with a uniformly hydrogenated (110) surface



also realizes a large energy gain. The increased energy gain is due to the assumption that a second fluorine atom occupies the surface radical site of the hydrogen which was desorbed as HF after reacting with the first fluorine atom. Thus, there is no F_2 bond to break and the energy gain is increased relative to the last reaction.

Equivalent reactions of atomic and diatomic hydrogen with fluorinated surfaces have also been modeled. These reactions,



and



also exhibit large energy gains. The four non-growth mechanisms are obviously self-limiting and are only dependent on the availability of the precursor gas in enough quantity to switch the adatoms.

Reactions (5–8) can be appropriately combined with one of the two growth reactions to obtain monolayer per cycle ALE growth mechanisms. The most promising monolayer ALE mechanism would consist of reaction (1) alternated with reactions (7) or (8). This mechanism would be self-limiting and exhibits substantial energy gains at each step of the cycle.

5. Conclusions

In summary, we have used endpoint energetics to identify favorable reactions using hydro- and fluoro-based gas species on the fluorinated and hydrogenated diamond (110) surface. All of the reactions are most likely self-limiting and may be appropriately combined to form monolayer and bilayer growth per cycle ALE mechanisms. C_2H_4 and C_2F_4 were used as the growth precursor gases when exposed to an oppositely terminated surface. Atomic and diatomic hydrogen and fluorine gases were modeled as reacting with the oppositely terminated surface with the end result being the switching of the surface terminating

adatoms. All of the reactions relied on the desorption of HF to realize substantial energy gains.

References

1. M.L. Yu, Thin Solid Films **225**, 7 (1993).
2. J.R. Creighton and B.A. Bansenauer, Thin Solid Films **225**, 17 (1993).
3. S.M. Cohen, T.I. Hukka, Y.L. Yang and M.P. D'Evelyn, Thin Solid Films **225**, 155 (1993).
4. S. Imai, T. Iizuka, O. Sugiura and M. Matsumura, Thin Solid Films **225**, 168 (1993).
5. D.D. Koleske, S.M. Gates and D.B. Beach, Thin Solid Films **225**, 173 (1993).
6. R. Car and M. Parrinello, Phys. Rev. Lett. **55**, 2471 (1985).
7. G.B. Bachelet, D.R. Hamman and M. Schlüter, Phys. Rev. B. **26**, 4199 (1982).
8. G. Li and S. Rabii, preprint (1992).
9. B.G. Johnson, P.M.W. Gill and J.A. Pople, J. Chem. Phys. **7**, 5613 (1993).
10. V.B. Aleskovski and V.E. Drozd, *Proc. First Inter. Symp. on Atomic Layer Epitaxy*, edited by L. Niinisto, Acta Polytechnica Scandinavica, Chem. Techn. and Metallurgy Ser. **195**, 156 (1990).

Binding Energies (eV)			
Molecule	B.E.	LDA theory	Expt.
C_2H_4	28.62	26.06	23.07
HF	6.83	6.34	5.86
F_2	3.92	3.63	1.60
H_2	4.84	4.66	4.48

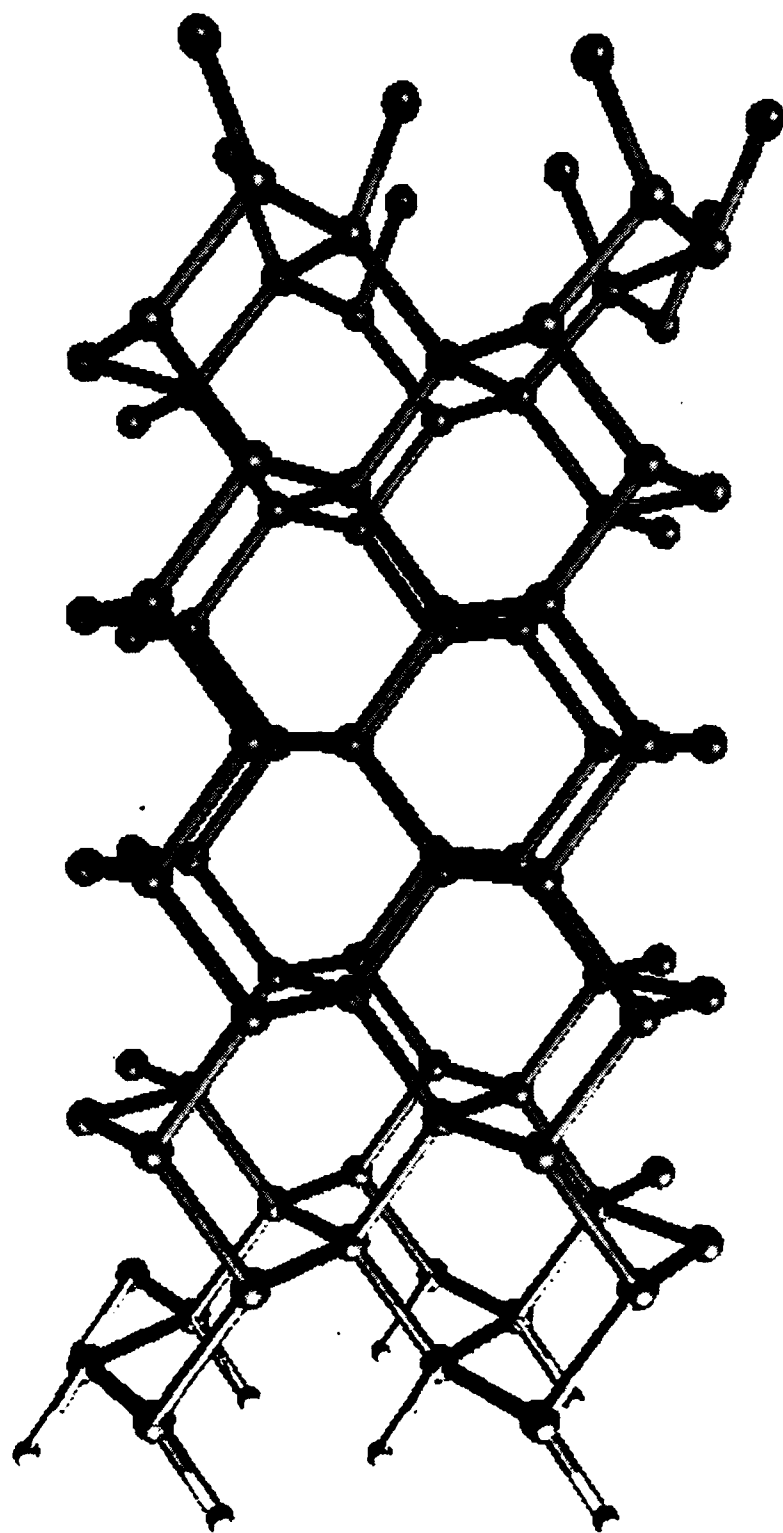
Table 1: Total binding energies of selected gas species.

Vibrational Energies (cm ⁻¹)			
Molecule	ω	LDA theory	Expt.
HF	4022	3912	4139
H ₂	4221	4207	4401
F ₂	1130	1087	923

Table 2: Vibrational Energies of diatomic molecules.

Molecular Geometry			
Molecule	Geom.	LDA theory	Expt.
C ₂ H ₄			
<i>r</i> (CC)	1.336	1.331	1.339
<i>r</i> (CH)	1.099	1.098	1.085
<i>a</i> (HCH)	116.9	116.4	117.8
HF			
<i>r</i> (HF)	0.944	0.940	0.917
F ₂			
<i>r</i> (FF)	1.448	1.389	1.417
H ₂			
<i>r</i> (HH)	0.774	0.765	0.741

Table 3: Molecular Geometries of selected gas species.



IV. Growth of Diamond Particles on a Ni₃Si Substrate

A. Introduction

The attainment of heteroepitaxial diamond is important if the microelectronics industry is ever to see the full utility of diamond's unique and excellent properties. Currently, oriented diamond particles have been deposited on c-BN, Si, SiC, Ni and Co. However, there are limitations to these substrate systems. For c-BN, this limitation is the difficulty in obtaining single crystal c-BN substrates of reasonable size. In growth on Si and SiC, there are problems with the large lattice mismatch (around 34% for Si and 18% for SiC) which results in misorientation in the resulting diamond particles. And for Ni and Co, while there is an excellent lattice match, there are adhesion problems and difficulty in obtaining complete films of diamond. A combination of two of the systems in which orientation has already been observed, Ni and Si, has been utilized as a substrate for heteroepitaxial diamond. By forming a nickel silicide, one combines the lattice match of the nickel with silicon's ability for covalent overlap and improved interface chemistry. Also, by introducing Ni into Si, the surface energy should increase from 870 ergs/cm² [1] to 1740 ergs/cm² [2] at room temperature, which may assist in the two-dimensional nucleation of diamond. Specifically, our primary candidate from the nickel silicide system is Ni₃Si which is cubic (Cu₃Au-type structure) and has a small lattice mismatch with diamond (approximately 2%).

B. Experimental

Currently, a bulk nickel silicide is being utilized. This silicide was produced by an arc melting and drop casting technique and involved mixing stoichiometric amounts of the nickel and silicon components to produce the compound Ni₃Si. The silicide sample was produced by Dr. C.T. Liu at Oak Ridge National Laboratory in the Metals and Ceramics Division. The resulting silicide was polycrystalline with small grains (average grain size was approximately 20 μ m in diameter) and has been characterized by metallography, XRD (both diffractometer and Debye-Scherrer), XPS, AES, and TEM as being largely cubic Ni₃Si. Diamond films were deposited on these substrates in a hot-filament chemical vapor deposition chamber connected *in-vacuo* with XPS and AES. Also, so that comparisons could be made with the chemistry of the nickel system, the same conditions were utilized in depositing on polycrystalline nickel. Typical conditions were a filament temperature of over 2200°C, substrate temperature of approximately 850 °C, pressure of 20 Torr, and methane concentration of 1% in hydrogen. The resulting films were characterized by SEM, Raman, XPS and AES.

C. Results and Discussion

An optical micrograph of the silicide sample is presented in Fig. 1 and gives evidence for the existence of two phases. In Fig. 2, the XRD diffractometer pattern of the silicide is plotted. The

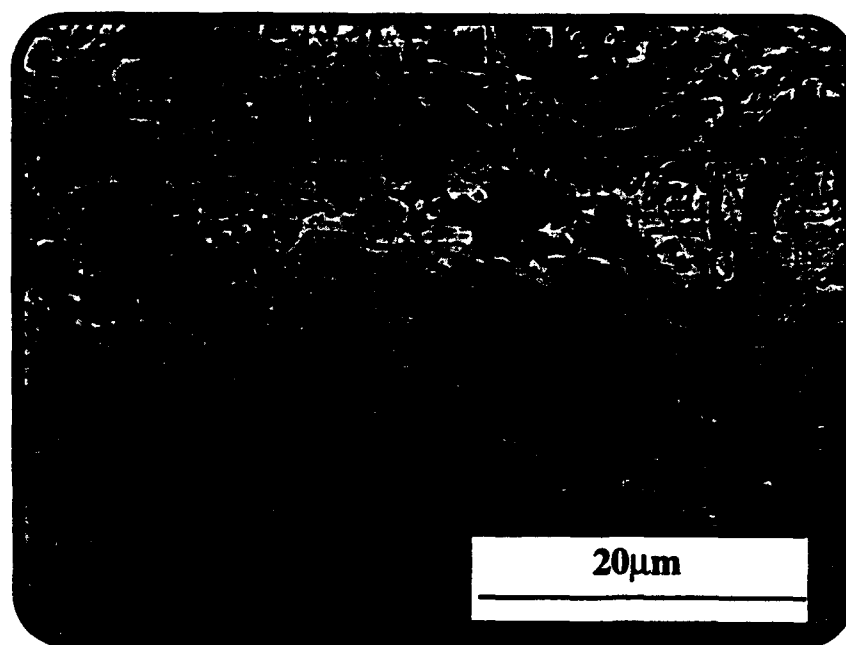


Figure 1. Optical micrograph of bulk nickel silicide sample at 500X.

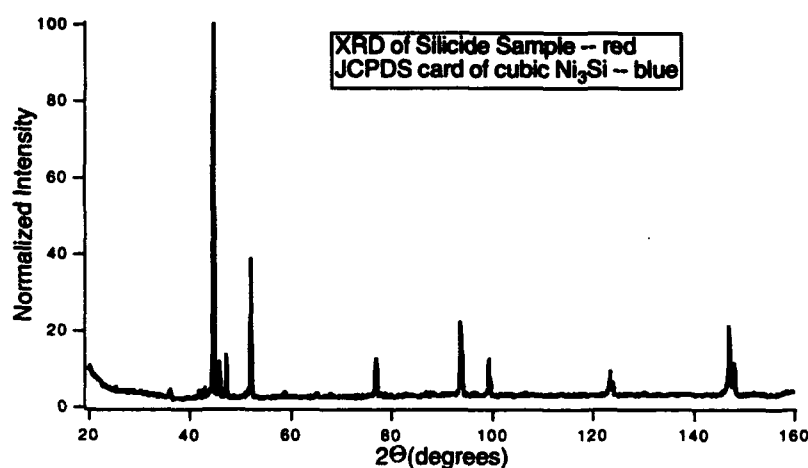


Figure 2. XRD pattern of nickel silicide sample.

peaks match up quite well with the powder pattern for cubic Ni_3Si . However, there are two peaks at a 2θ of 46.0° and 47.3° that are not accounted for by the cubic pattern. These peaks did correspond to that of the high temperature Ni_3Si phase which is a monoclinic material. In corroboration of the stoichiometry, XPS and AES quantitative analysis gave a $X_{\text{Ni}}/X_{\text{Si}}$ ratio of approximately 3. Also, TEM showed the presence of two phases: one the cubic Ni_3Si and the second a distorted cubic structure, which was possibly monoclinic.

In Fig. 3, two SEM micrographs resulting from diamond growth on the silicide are presented. There appears to be some evidence for oriented particles on the silicide. Figure 4 shows two SEM micrographs from growth on the nickel. As can be seen, the majority of the growth on the nickel substrate had DLC growth as in the top micrograph of Fig. 4. There also was poorly faceted diamond on the sample, as in the bottom micrograph of Fig. 4. Figures 5 and 6 are the Micro-Raman spectra for diamond growth on the nickel silicide and nickel, respectively. The Raman for growth on the nickel silicide, obviously, shows a very strong diamond peak centered at 1334 cm^{-1} with a FWHM of 3.6 cm^{-1} and very little sp^2 component. For growth on the nickel, however, the Raman shows a very weak and broad diamond peak and a large sp^2 peak.

D. Conclusions

Diamond particles were obtained on the nickel silicide where, under the same conditions, graphite and DLC was obtained on the pure nickel substrate. There seems to be some evidence that oriented particles were obtained on the nickel silicide. More interesting, however, may be the result that the addition of even a small amount of silicon to the nickel greatly changes the chemical properties from that of pure nickel.

E. Future Research

The nucleation density attained was quite small and was on the order of 10^5 . This is as would be expected for a material that has not been scratched or biased. We would, however, like to increase this nucleation density by biasing. Also, this proof of concept suggests that if single crystal nickel silicide can be obtained, it may be a heteroepitaxial substrate for diamond. Thus, we will also be working on methods to obtain single crystal nickel silicide, or, at least, a larger grained material.

F. Acknowledgments

Dr. C.T. Liu of the Metals and Ceramics Division is gratefully acknowledged for the fabrication of the silicide material used in this research. We appreciate the assistance of Ambika Somashekhar and Dr. Robert Nemanich for their Raman support. Also, we appreciate Dr. Nadia El-Masry's assistance in examining the TEM results.

G. References

1. K.-N. Tu, J. W. Mayer, L. C. Feldman, *Electronic Thin Film Science for Electrical Engineers and Materials Scientists* (Macmillan Publishing Company, New York, 1992), p. 38.
2. B. J. Keene, *Surface and Interface Analysis* **10**, 367 (1987).

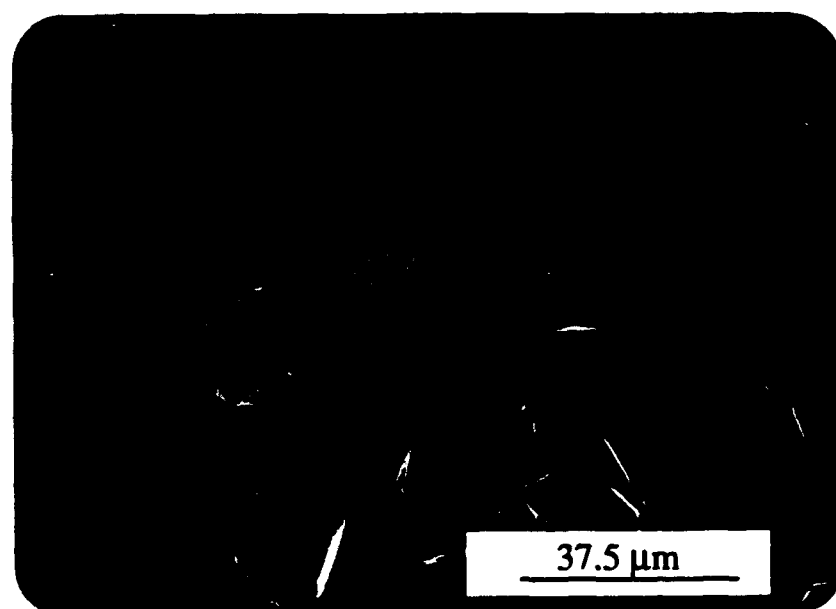
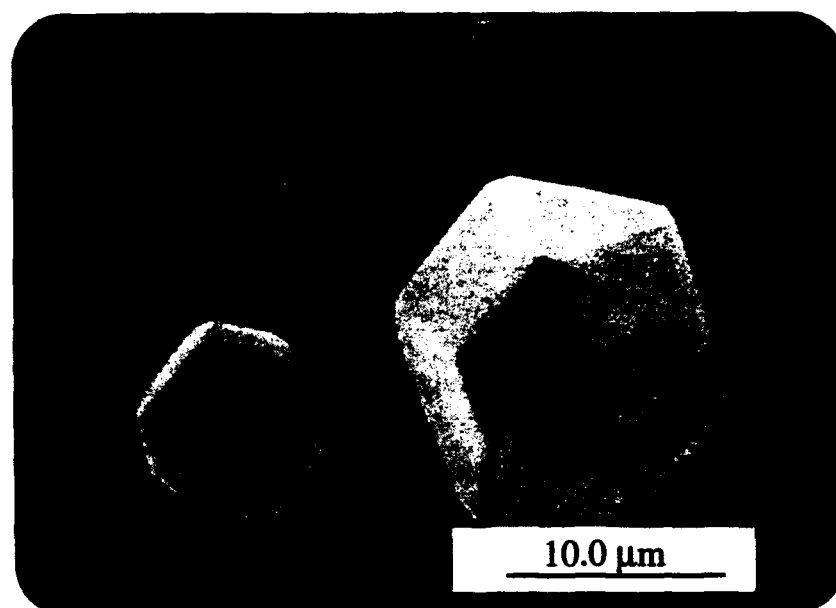


Figure 3. SEM micrographs of diamond particles on the nickel silicide.

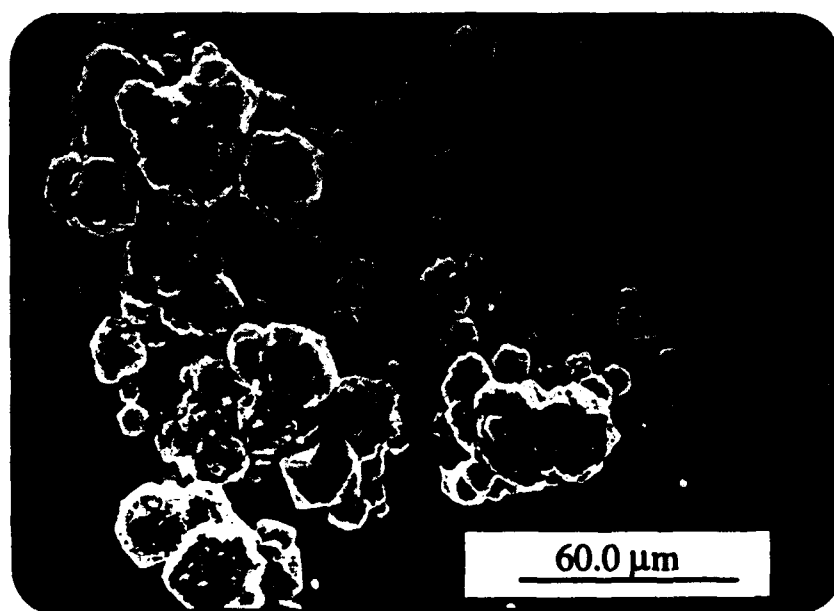
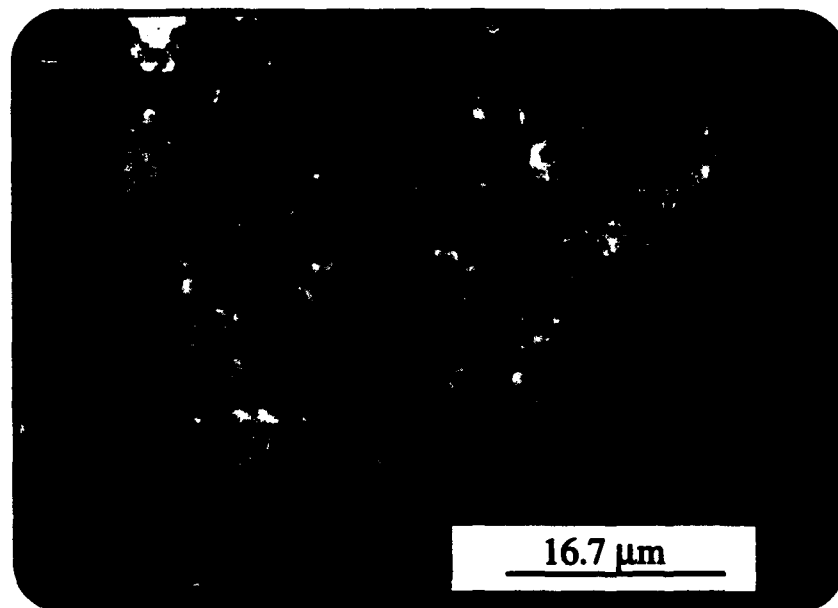


Figure 4. SEM micrographs of growth on the nickel.

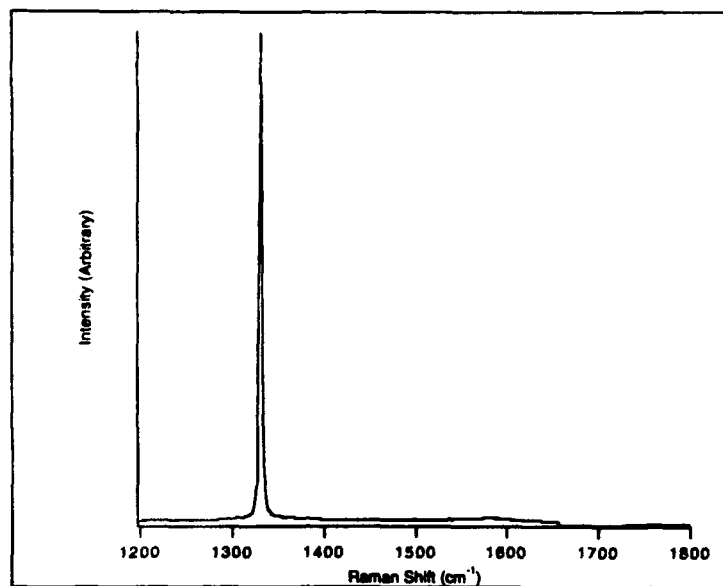


Figure 5. Micro-Raman of growth on the nickel silicide.

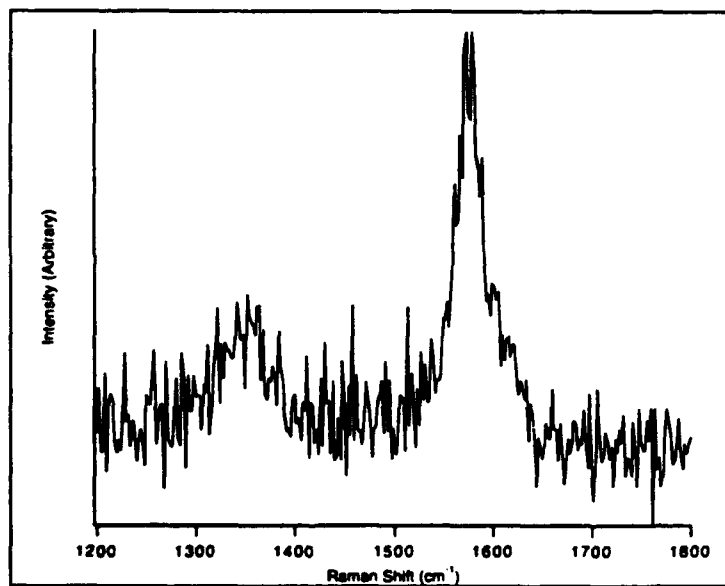


Figure 6. Micro-Raman of growth on the nickel.

V. Diamond Thin Film Coated Si Field Emitters

J. Liu, V. V. Zhirnov^a), A. F. Myers, W. B. Choi, G. J. Wojak, and J. J. Hren
*Department of Materials Science and Engineering, North Carolina State University,
Raleigh, NC 27695-7907*

S. D. Wolter, M. T. McClure, and J. T. Glass
Materials Research Center, North Carolina State University, Raleigh, NC 27695-7919

Diamond thin films have been deposited on the surface of single crystal silicon field emitters using bias-enhanced microwave plasma chemical vapor deposition. Polycrystalline diamond structures with high nucleation density ($10^{10}/\text{cm}^2$) and small grain size ($<10\text{ nm}$) were achieved. Field emission from these diamond coated emitters exhibited extremely high stabilities as well as high current densities.

I. INTRODUCTION

The study of heteroepitaxial growth of diamond films is currently of great interest not only as a subject of basic research but also for a variety of applications of diamond films. By taking full advantage of its unique physical and chemical properties such as high thermal conductivity and negative electron affinity, diamond will be an ideal material for the new generation of solid state electronic devices¹. Several new Schottky and ohmic contact structures, based on CVD diamond films, have been fabricated and evaluated during recent years. In the new emerging field of vacuum microelectronics, Si remains as a favored cathode material because of its well-established microprocessing technology. It is also strongly recommended, from the applicable device point of view, to have a thin film of diamond on the Si surface in order to enhance the operating current as well as the stability.

Our previous studies have demonstrated that thin films of SiC were producible on nanometer-scaled Si field emitters without altering the geometrical structures of the emitters significantly². Improved performance was achieved on these SiC coated emitters as compared to the pure Si ones. Growth of epitaxial diamond thin films on Si (100), (110), and (111) flat substrates has been studied by several investigators^{3, 4}. Considering the facts of known diamond nucleation size and density, appropriate processing conditions must accommodate the highly curved surface geometries of the Si emitters.

The current study was focused on formation of *nm* scale diamond thin films on Si field emitter surfaces. This research can essentially serve two purposes: first, to provide the performance study of diamond coated Si field emitters; secondly, to facilitate the information on the mechanism of diamond nucleation. A novel approach, termed bias-enhanced diamond nucleation, was used during the procedure

of microwave plasma chemical vapor deposition (MPCVD)³. The negative biasing pretreatment, preceded by an H_2 plasma cleaning step, allowed a conversion layer of SiC to form on Si and diamond to nucleate on the SiC. Such a pretreatment method is very suitable for the study of diamond nucleation on the surface of field emitters since it does not involve any scratching by diamond abrasives or other conventional forms of nucleation enhancement, therefore avoiding the possibilities of tip damage and over-sized diamond crystal growth.

II. EXPERIMENT

The low pressure diamond growth was performed on n-type (111) oriented single crystal Si whiskers which were fabricated by a vapor-liquid-solid (VLS) mechanism⁵. These whiskers were sharpened by subsequent procedures of chemical etching and oxidation to achieve the nanometer scale radii of curvatures. Fig. 1 illustrates a part of these Si tips in an array configuration. These Si tips usually have radii

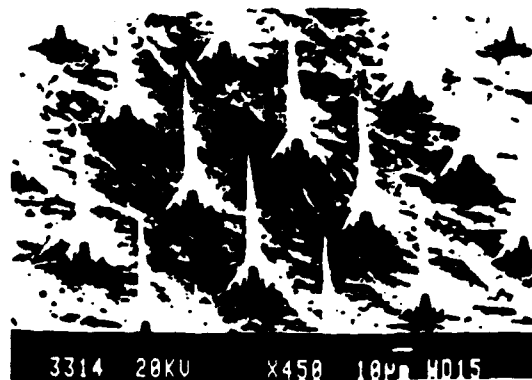


FIG. 1. SEM micrograph of the single crystal Si field emitter array fabricated by a VLS mechanism.

a) Permanent address: *Institute of Crystallography, Russian Academy of Sciences, Moscow 11733, Russia.*

of curvatures about 30 nm or less and are ideal samples for studies of field emission/field ion microscopies (FEM/FIM) and high resolution electron microscopies. Transmission electron microscopy (TEM), for example, can easily be performed on these tips without any further sample preparation. It eliminates any post-treatment altering or damaging to the specimen and has been an important advantage for the current study.

The three-step diamond growth process, involving H₂ plasma cleansing, bias-enhanced nucleation, and deposition, was carried out in a UHV MPCVD reactor chamber. The Si specimens were first cleaned by concentrated HF solution for removing the native oxide before loading into the growth chamber. The *in vacuo* cleaning step was undertaken by immersing the Si samples in microwave plasma with an H₂ pressure of 15 Torr. The temperature on the Si specimen was generated by the plasma as well as by a substrate heater and was maintained between 850 to 900 °C as monitored by an optical pyrometer. The biasing step, which is called bias-enhanced nucleation (BEN), was performed immediately following the carburization, where the CH₄/H₂ ratio was increased to 5% and a bias potential of -250 V DC was applied to the specimen substrate. A biasing length between 5 to 25 minutes was used in the experiments. SEM and TEM studies were performed before and after these processes. Following the biasing step, the substrate voltage was withdrawn and the pressure was raised to 25 Torr for the deposition process, which usually lasted 15 to 45 minutes for our particular specimens. The deposition process further enhanced the preceding diamond nucleation as well as the epitaxial growth.

High resolution electron microscopies, performed on a JEOL 6400F field emission SEM and two additional TOPCON 002B TEM's, were used to study the surface morphology and interfacial structures of the resultant emitters. Field emission characterizations were performed in a UHV FIM/FEM system.

III. RESULTS AND DISCUSSIONS

III.1. Electron Microscopy Studies

It was found in our experiments that under the negative biasing condition diamond can start to nucleate on the Si emitter surface within 5 minutes after the H₂ plasma cleaning step. The negative BEN treatment activated processes of carburization as well as diamond nucleation on the Si surface. The nucleation density, varying with biasing time as well as location, was measured to exceed $10^{10}/\text{cm}^2$ for a 20 minutes biasing treatment. This is considerably higher than the result on a flat substrate under the same conditions. Fig. 2 shows a typical single crystal Si tip after it was treated by negative biasing for 20 minutes. The formation of stable diamond nuclei was significantly enhanced by the negatively biased surface on which surface atoms or adatoms are more effectively activated by increased bombardment of positively charged energetic ions. The local

field distribution, and thus the flux of charged particles, is considered as the main contributor to the variation of local nucleation density.

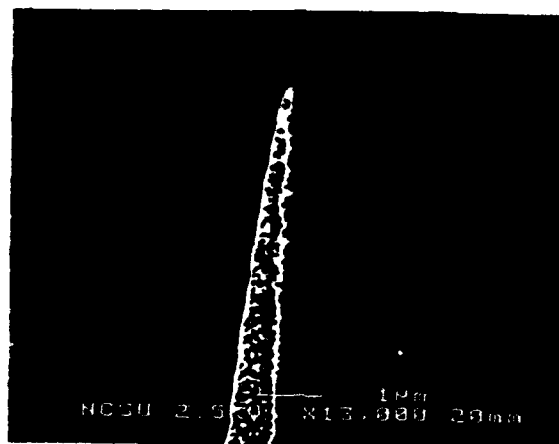


FIG. 2. A single crystal Si tip after treatment by negative BEN for 20 min.

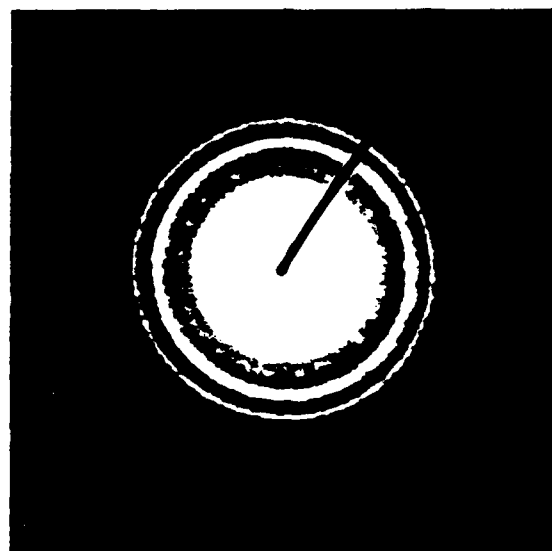


FIG. 3. A typical TEM diffraction pattern of the polycrystalline diamond coating and the SiC interlayer on Si tip surface.

After the BEN process, polycrystalline structures of diamond and a SiC interlayer were found on the Si emitter by high resolution TEM analyses. The structures were further confirmed by TEM diffraction studies. Fig. 3 shows a diffraction pattern of the nucleated diamond surface and the SiC interlayer. The rings match very well with the

corresponding crystallographic orientations of diamond. Single crystal diamond grains, ranging from a few nanometers to several tens of nanometers, were found in the diamond layer. The thickness of the SiC interlayer was measured to be between 20 to 100 Å. One or more faint rings corresponding to SiC can be observed in diffraction images like Fig. 3. The experimental results have further verified that the BEN process on Si first creates a SiC layer on which diamond starts to nucleate due to enhancement of the C-C bonding. It has been found that an intensified carburization process can produce a single crystal SiC conversion layer as well as epitaxial diamond growth³. However, these intensified condition and diamond nucleation may be beyond the scale which is required for a field emitter. It was also found that the deposition process after BEN enlarged the size of existing diamond grains in proportion to the process time. In order to maintain the geometry of the field emitter, we used minimal deposition times and sometimes even eliminated this step.

III. 2. Field Emission Characterizations

Field emission current-voltage (I-V) measurements were performed on diamond coated Si single emitters as well as on multi-emitter arrays. The tip-to-anode distance was kept at 10 mm and the vacuum was at the low 10^{-9} Torr range or better. Emission data from each sample was taken by several consecutive measurements. A total emission current of a few μA per tip both from pure Si and diamond coated emitters was easily obtained. To avoid tip destruction, however, our field emission experiments were carried out under mid-range current density at this stage for the purpose of analysis. Two sets of I-V measurements, one from a single pure Si tip and the other from a diamond coated single tip, are shown in Fig. 4. The data were analyzed using the Fowler-Nordheim equation as well as related curve fitting and calculations.

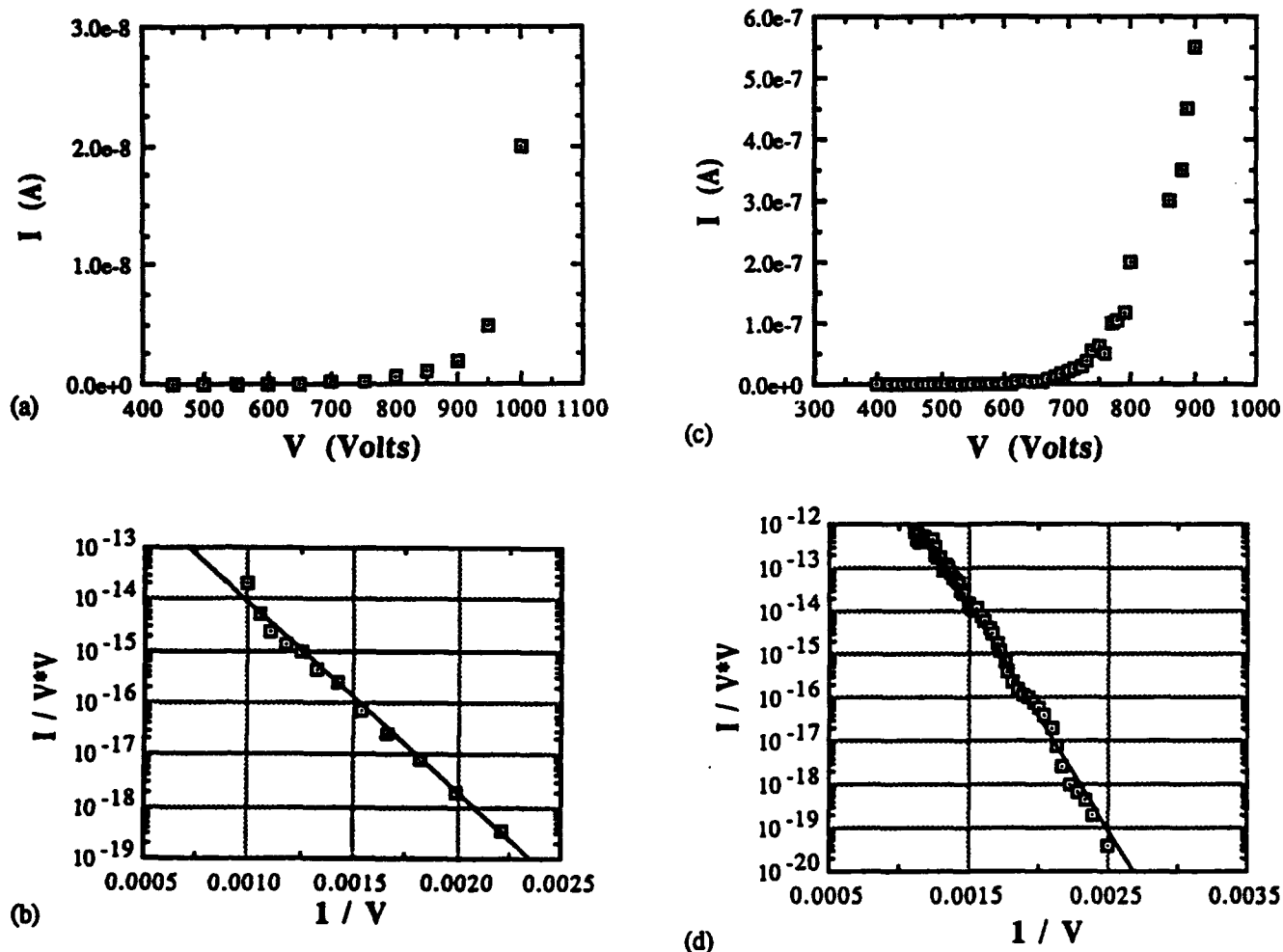


FIG. 4. Field emission characteristics and the corresponding Fowler-Nordheim plots: (a), (b) Pure single Si emitter; (c), (d) Diamond coated single emitter.

Very interesting results were obtained from diamond coated emitters. The emission exhibited exceptional stability as well as reproducibility. An unusually large emitting area was obtained compared to the pure Si samples which demonstrated consistency to previous results. Measured from both single and multi-emitter array, the emitting area was determined to be between 10^{-11} to 10^{-10} cm^2 . This happens to correspond to the entire surface area of the tip whose radius of curvature was estimated to be about 300 Å. Meanwhile, our measurements from pure Si and other metal emitters were very similar to those obtained by other investigators. Field emission in such cases showed a very small emitting area of $\sim 10^{-16} \text{ cm}^2$, which corresponds to only one or a few atomic sites. Surprisingly, the emitting behavior from a diamond coated emitter surface implied a full surface emission. Compared to a conventional field emitter whose surface is usually covered with unstable adsorbates or contaminants, diamond's chemically inert surface is obviously much more stable and therefore has the potential to emit electrons from a larger area. Although this mechanism is still under investigation, we believe it could be very significant for enhancing the total emission current and suppressing emitter disruption.

Fig. 5 shows measured emission stabilities for a pure Si emitter and diamond coated single and multi-emitters. It was found that the stability of diamond coated emitters was one to two orders of magnitude higher than that of a pure Si emitter. This may provide a strong verification for the above argument on the emitting area.

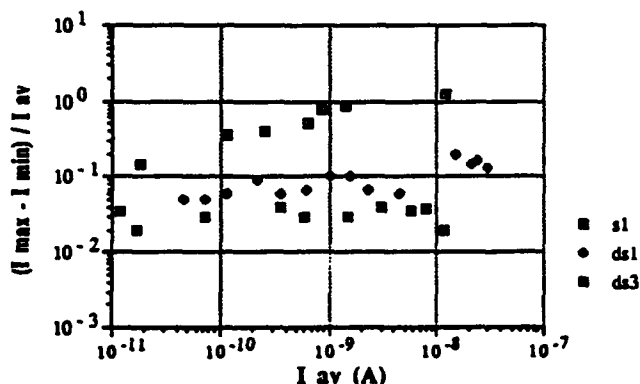


FIG. 5. Field emission stability of the emitters: (s1) pure single Si tip; (ds1) diamond coated single emitter; (ds3) diamond coated 4x4 emitter array.

Another interesting phenomenon was the determination of the work function of diamond coated emitter surfaces. A parabolic model for the emitter surface was used in our preliminary approach. The effective work function of the diamond coated surface was estimated to range from 3.5 to 4.5 eV for emitters with radii of curvatures between 300 and 500 Å. More accurate measurements and careful analysis are needed to obtain satisfactory results. In addition, a more specific theoretical model should be considered for semiconductor emitters.

IV. SUMMARY

This new experimental approach to improve the performance of Si field emitters has shown very encouraging results both on technical methodology and resultant phenomena. Bias-enhanced nucleation MPCVD has demonstrated its feasibility in forming polycrystalline diamond thin films on nano-scale Si field emitter surfaces. Superior performance was obtained from diamond coated emitters in our preliminary investigations. An exceptionally large emitting area like we observed on the diamond coated emitter surface has not been previously reported. Emission from such a large area suggests that diamond coated emitters may operate under a different mechanism than conventional emitters. We have shown that diamond coatings can significantly enhance the total emission current as well as the emission stability of Si field emitters.

REFERENCES

- (1) G. S. Gildenblat, S. A. Grot, C. R. Wronski, and A. R. Badzian, *Proc. IEEE*, 79, 647 (1991).
- (2) J. Liu, U. T. Son, A. N. Stepanova, and et al., *J. Vac. Sci. Technol.*, B12 (2), Mar/Apr (1994).
- (3) S. D. Wolter, B. R. Stoner, J. T. Glass, and et al., *Appl. Phys. Lett.*, 62 (11), 1215 (1993).
- (4) X. Jiang, K. Schiffmann, A. Westphal, and C. P. Klages, *Appl. Phys. Lett.*, 63 (9), 1203 (1993).
- (5) E. I. Givargizov, *J. Vac. Sci. Technol.*, B11 (2), 449 (1993).

VI. Effects of Gas Flow Ratio on the Growth Mode of Silicon Carbide by Gas-source Molecular Beam Epitaxy

A. Introduction

Since silicon carbide possesses a wide band gap (2.9 eV), high saturated electron drift velocity (2×10^7 cm/s), high breakdown field (5×10^6 V/cm), high thermal conductivity (3.5 W/cm $^\circ$ C at 300K), and chemical stability, it has been extensively studied for high temperature, high-power, and high-frequency electronic device applications [1]. Besides its superior electrical properties, SiC has an unique crystallographic characteristic, namely extensive *polytypism* [2]. The difference in stacking sequences of the close-packed planes, (111)_{cubic} or (0001)_{hexagonal}, can form more than 250 different polytypes. The 3C (β), 6H, and 4H are most popular polytypes due to their energetic and kinetic stability in nature. Although their formation mechanisms are not yet known, their film growth has been conducted by several methods, such as chemical vapor deposition [3, 4] and molecular beam epitaxy [5, 6]. In terms of homoepitaxial growth of SiC, which can result in a higher film quality due to the lack of lattice mismatch and other effects such as in SiC/Si system, the film polytype can be generally determined by the substrate polytype, if the growth mode is 'step flow' [3]. Step flow can be kinetically achieved when adatoms reach the step sites and retain the identical stacking sequence as the substrate. Therefore, 6H films can be formed on 6H SiC substrate with the presence of steps at relatively lower growth temperatures of $<1500^\circ\text{C}$ where 3C is normally the more stable polytype [7].

Step flow growth has been achieved by CVD in the range of growth temperatures of 1200°C - 1600°C to produce 6H and 4H homoepitaxial films [3, 4, 8]. The growth mechanisms of CVD deposited films investigated through kinetic [9] and microstructural [10] considerations. On the other hand, SiC film growth by MBE at lower growth temperatures ($<1200^\circ\text{C}$) on 6H-SiC substrates has not fully been successful. Yoshinobu *et al.* has grown 3C films on either 6H-SiC (000 $\bar{1}$) [5] and 3C-SiC(001) [11] substrates at $<1000^\circ\text{C}$ by an alternating supply of Si_2H_6 and C_2H_2 . However, a simultaneous supply of each gas caused either no film or polycrystalline island growth below 1100°C .

In this paper, we have successfully grown 6H-SiC films on vicinal 6H-SiC (0001) substrate at 1050°C by a simultaneous supply of source gases. The effects of gas flow ratios of $\text{C}_2\text{H}_4/\text{Si}_2\text{H}_6$ on growth mode was investigated. We found that the ethylene-rich conditions can cause islanding and that step flow growth can be achieved by a 1:1 ratio. Considering the surface chemistry, reconstruction, and related adatom diffusivities through the observation of the initial stage of growth by HRTEM and *in-situ* RHEED, a growth model is discussed.

B. Experimental Procedure

Silicon carbide films were typically grown on Si-faces of 6H-SiC (0001) substrates. The substrates used in this study were off-axis (3-4° off (0001) toward $\langle 11\bar{2}0 \rangle$) provided by Cree Research, Inc.[14] Films were all grown by a GSMBE method under varying conditions. The typical growth conditions are listed in Table I. Note that all depositions were performed at 1050°C. The detail description of the deposition technique can be found in Ref. 6. The as-received substrates were dipped in 10% HF solution for 5 min. to remove the protective surface oxide layer (typically $\sim 750\text{\AA}$), immediately followed by loading into the MBE system. Each substrate was annealed at 1050°C in the ultra high vacuum environmental ($\sim 1 \times 10^{-9}$ torr) for 30 min. prior to the deposition in order to remove residual hydrocarbons and surface oxides. During the depositions, RHEED patterns were monitored by the use of a charge coupled device camera and video recorder. After growing the film, the sample was cut and glued face to face to make a cross-sectional TEM sample, followed by the standard sample preparation techniques [13]. Finally, the sample was examined by a Topcon EM-002B operated at a 200kV acceleration voltage with the use of the $\langle \bar{2}110 \rangle$ zone axis.

Table I. Typical Growth Conditions for the SiC Films

Temperature	1050°C
Se ₂ H ₆ flow rate	0.1 sccm
C ₂ H ₄ flow rate	0.1-1.0 sccm
C ₂ H ₄ /Si ₂ H ₆ flow ratio	1.0, 2.0, 10.0
Growth rate	50-100Å/hr

C. Results and Discussion

Figure 1 shows the cross-sectional image of the SiC film on an off-axis (vicinal) 6H-SiC (0001) substrate. The resulting film was generally cubic (3C) in structure and had a rough surface morphology due to island growth under the condition of a ratio of $C_2H_4/Si_2H_6 = 2$. The islands (3C) which nucleated on the different terrace sites and are separated by steps (indicated by the arrows) can be clearly seen. The more ethylene-rich condition of $C_2H_4/Si_2H_6 = 10$ showed the similar features of $C_2H_4/Si_2H_6 = 2$ condition except the density of the islands decreased. Moreover, it can be observed that there are steps which are $1/2$ to 2 unit cell height ($c = 15\text{\AA}$). According to the preliminary investigation of vicinal 6H-SiC surface structure by HRTEM, monolayer (consisting of Si and C layers) steps predominantly exist on the surface [14]. Thus, this implies the occurrence of step bunching at the early stage

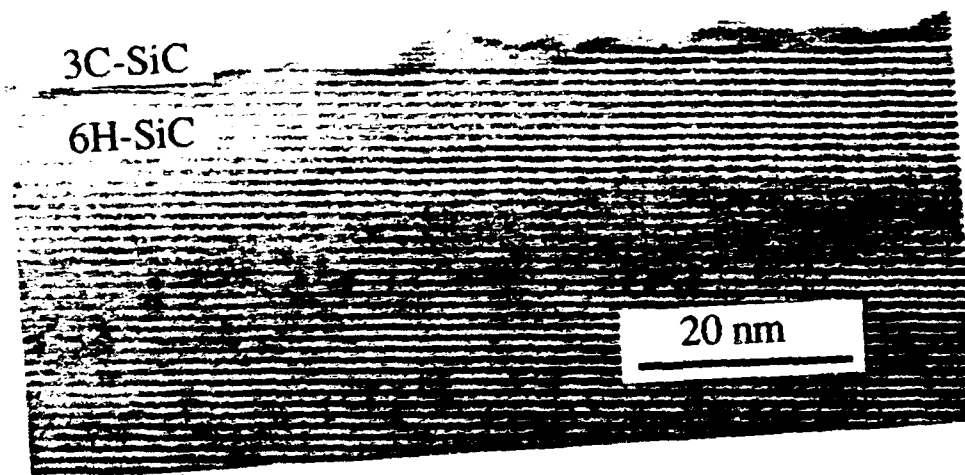


Figure 1. TEM image of 3C island growth at $C_2H_4/Si_2H_6 = 2$.

of growth. At the early stage of growth where monolayer steps are available (accordingly terrace width is $\sim 60\text{\AA}$), the adatoms can migrate to the step site to cause step flow because of the comparable diffusion length of the adatoms to terrace width. It should be emphasized here that step bunching can substantially be observed if the difference in diffusivities of the (000n) planes of 6H-SiC where $n=1$ to 6 is present. Interestingly, energetic calculations by Heine *et. al* [7] can provide the difference in surface energies, showing the lowest energy plane is A in the ABC notation. Thus, the presence of step bunching at the early stage of growth can be reasonable. As the terrace width increases, adatoms can not reach the step sites to retain step flow due to the limited diffusion length at the growth temperature, and ultimately islands form on the terrace site. During the growth of both films, RHEED initially showed a streaky (1×1) pattern and changed to a spotty (1×1) pattern which was indicative of 3C island formation and included double positioning boundaries (DPBs) [15]. The details of the RHEED study will be reported in the future.

Under the different condition in which $C_2H_4/Si_2H_6 = 1$, a dramatic change in the film growth mode was observed. Figure 3 (a) shows 6H-SiC film growth with a stepped surface. At present the film growth rate is not verified, however, it is very positive that 6H-SiC film growth could be performed under these conditions. Because the stepped surface feature is

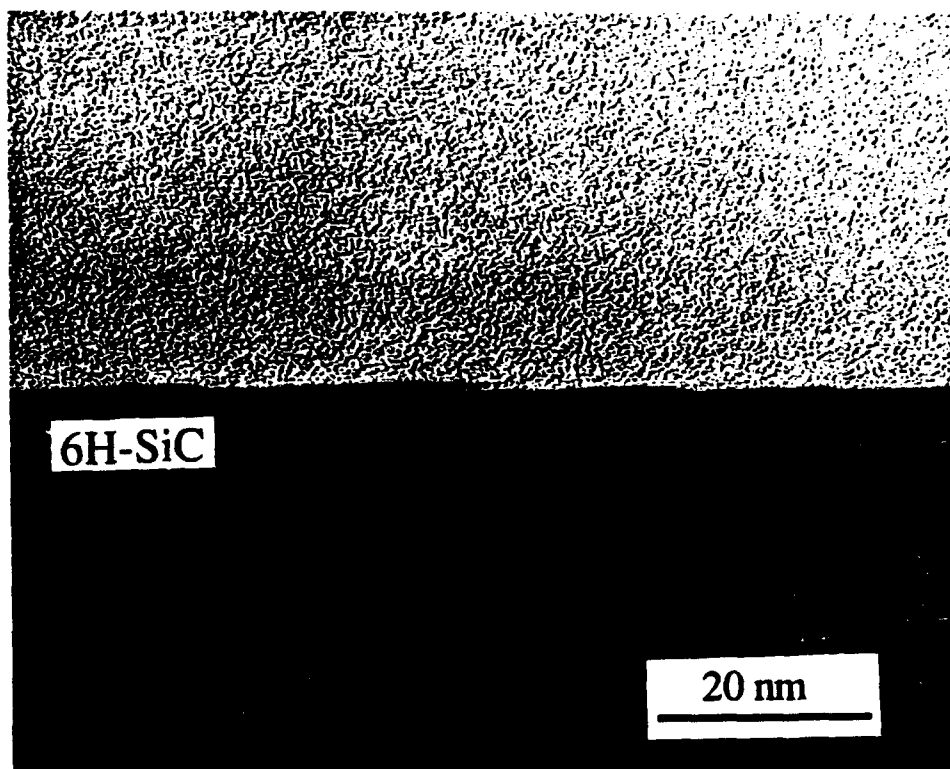


Figure 2. TEM image of step flow growth at $C_2H_4/Si_2H_6 = 1$.

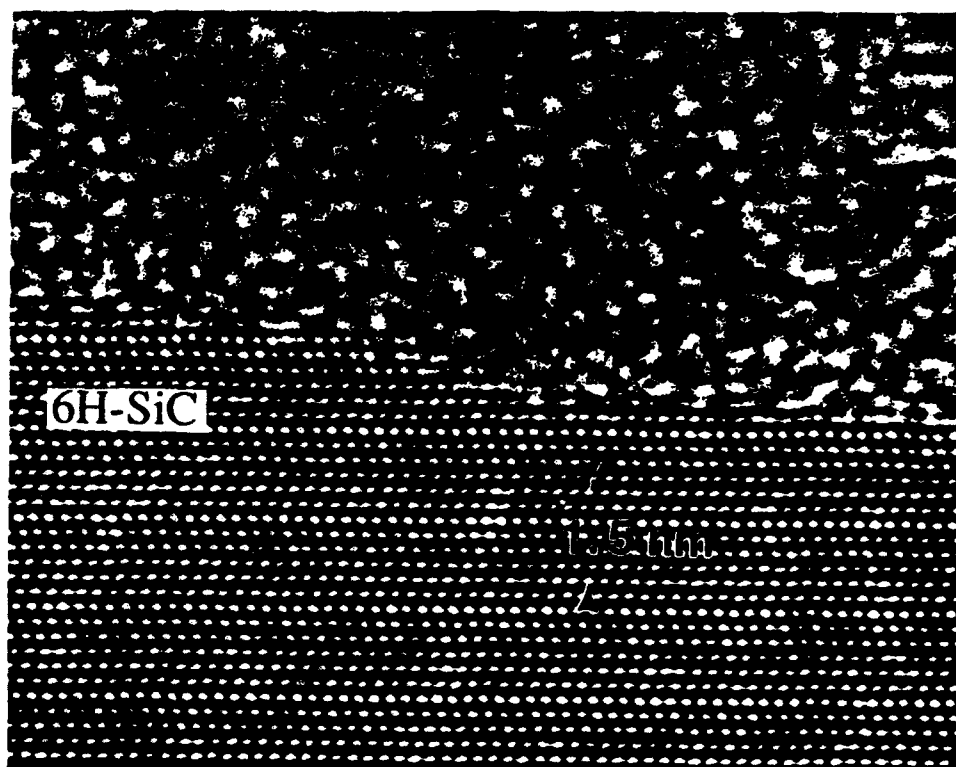


Figure 3. HRTEM image of the stepped surface occurred by step flow growth at $C_2H_4/Si_2H_6 = 1$.

apparently different from that of the substrate surface as mentioned in the previous paragraph. In Fig. 3 (b), a magnified image of the stepped surface is shown. A step having a half unit cell height (3~4 monolayers) clearly indicates step flow growth. During the film growth, (3×3) reconstruction was observed by RHEED as shown in Fig. 4. Kaplan proposed the model for this reconstruction [16], consisting of an adsorbed Si bilayer.



Figure 4. (3×3) RHEED pattern observed during the growth of the SiC film at $C_2H_4/Si_2H_6 = 1$.

We have recognized that the gas flow ratio of C_2H_4/Si_2H_6 influenced the growth mode significantly with step bunching plus island formation and step flow under ethylene rich (= 2 and 10) and 1:1 conditions, respectively. As indicated by the RHEED patterns, the (3×3) surface reconstruction occurred under the condition of $C_2H_4/Si_2H_6 = 1$, suggesting the lower surface energy of the growing surface. Thus, the surface mobilities of adatoms can be enhanced to some degree on such a reconstructed surface, leading a step flow growth.

D. Conclusion

In summary, we have successfully grown 6H-SiC films on 6H-SiC substrates by GSMBE utilizing a simultaneous supply of source gases at a relatively low temperature of 1050°C. Step flow growth was enhanced under the condition of $C_2H_4/Si_2H_6 = 1$ possibly due to the surface reconstruction during growth which introduced the higher mobility of adatoms. Under the different gas flow ratios such as $C_2H_4/Si_2H_6 = 2$ and 10, step bunching plus islanding was observed.

E. Future Plans

HRTEM and *in-situ* RHEED will continue to be used in studying the growth mechanisms. The growth mechanisms which has been established in this report will be investigated in more details through *in-situ* RHEED oscillation and a scanning tunneling

microscope at Oak Ridge National Laboratory. Preliminary observation of the very early stage of SiC growth showed the plausibility of the model established in this study. More quantitative discussion will be desired in terms of surface mobilities of adatoms on the reconstructed surfaces and growing surface chemistry. The control of polytype formation (2H and 4H) will be also challenged on the basis of the theory obtained in this study.

F. References

1. R. F. Davis, *Physica B* **185**, 1 (1993).
2. N. W. Jepps and T. F. Page, *Progress in Crystal Growth and Characterization* **7**, edited by P. Krishna (Pergamon Press, New York, 1983), 259.
3. H. S., Kong, J. T. Glass, and R. F. Davis, *J. Appl. Phys.* **64**, 2672 (1988).
4. H. Matsunami, T. Ueda, and H. Nishino, *Mater. Res. Soc. Symp. Proc.* **162**, 397 (1990).
5. T. Yoshinobu, M. Nakayama, H. Shimoi, T. Fuyuki, and H. Matsunami, *J. Cryst. Growth* **99**, 520 (1990).
6. L. B. Rowland, R. S. Kern, S. Tanaka, and R. F. Davis, *J. Mater. Res.* **8**, 2753 (1993).
7. V. Heine, C. Chen, and R. J. Needs, *J. Am. Ceram. Soc.* **74**, 2630 (1991).
8. T. Kimoto, A. Yamashita, A. Itoh, and H. Matsunami, *Jpn. J. Appl. Phys.* **32**, 1045 (1993).
9. T. Kimoto, H. Nishino, W. S. Yoo, and H. Matsunami, *J. Appl. Phys.* **73**, 726 (1993).
10. F. R. Chien, S. R. Nutt, W. S. Yoo, T. Kimoto, and H. Matsunami, *J. Mater. Res.* **9**, 940 (1994).
11. T. Yoshinobu, H. Mitsui, I. Izumikawa, T. Fuyuki, and H. Matsunami, *Appl. Phys. Lett.* **60**, 824 (1992).
12. Cree Research Inc., Durham, NC.
13. C. H. Carter, Jr., R. F. Davis, and S. R. Nutt, *J. Mater. Res.* **1**, 811 (1986).
14. unpublished
15. L. B. Rowland, R. S. Kern, S. Tanaka, and R. F. Davis, *Appl. Phys. Lett.* **62**, 3333 (1993).
16. R. Kaplan, *Surf. Sci.* **215**, 111 (1989).

VII. Growth and Characterization of Thin, Epitaxial Silicon Carbide Films by Gas-source Molecular Beam Epitaxy

A. Introduction

Interest in wide band gap semiconductor materials for use in high-temperature, -power, -frequency and -speed microelectronic devices resistant to radiation has escalated on a global scale within the last decade. Silicon carbide (SiC) is one of the leading candidate materials fueling this interest. This material occurs in a number of different structural variants called polytypes that arise as a result of the different stacking sequences of the Si/C bilayers along the directions of closest packing. There is one cubic polytype (β - or 3C-SiC) and approximately 250 hexagonal and rhombohedral polytypes that are collectively denoted as α -SiC. The most common of these is 6H-SiC. Many electronic properties, including band gap, are dependent on the polytype.

Thin film growth of 3C- and 6H-SiC has been achieved primarily via chemical vapor deposition (CVD) (see Davis *et al.* [1] for a review of this and related research). Monocrystalline Si wafers have been the principal substrate of choice for 3C deposition. This is achieved by a carbonization step in which a C-containing gas converts the Si(100) surface to 3C-SiC to reduce the effects of the large mismatches in lattice parameters ($\approx 20\%$) and coefficients of thermal expansion ($\approx 10\%$). The epitaxial growth of SiC films on $\alpha(6H)$ -SiC(0001) substrates via CVD has been reported for three decades [1]. When the [0001] direction of the 6H wafer is oriented off-axis $\leq 0.5^\circ$, the result is single phase β -SiC films [2,3]. Double positioning boundaries (DPB) are the primary defects in these films [4]. Deposition at $T \geq 1400^\circ\text{C}$ on substrates cut $3\text{--}4^\circ$ towards $[11\bar{2}0]$ have resulted in high-quality monocrystalline 6H-SiC layers with low defect densities [5,6].

Solid- and gas-source (GS) molecular beam epitaxy (MBE) techniques have also been employed for deposition of SiC films on a variety of substrates. All previous researchers achieved the growth of only β -SiC. The best results for lower defect densities have been obtained on 6H-SiC substrates. Kaneda *et al.* [7] studied the relationships between the ratio of fluxes of electron-beam evaporated Si and C and the temperature of the on-axis $\alpha(6H)$ -SiC(0001) substrates in the range of $1150\text{--}1400^\circ\text{C}$. Stoichiometric, epitaxial 3C-SiC(111) films were obtained at particular source flux ratios ($J_{\text{Si}}/J_{\text{C}} \geq 1$) between $1150\text{--}1400^\circ\text{C}$. No information was given by these authors regarding the substrate face, the microstructure of the resultant films or the type of defects present in these films; however, they were able to fabricate p-n junctions by adding B to the solid Si source. Rowland *et al.* [8] deposited β -SiC(111) on vicinal $\alpha(6H)$ -SiC(0001) at 1050°C using 0.5 standard cubic centimeters per minute (sccm) Si_2H_6 and 2.0 sccm C_2H_4 . The resulting films grew primarily as islands on the terraces between steps resulting in films with a high DPB density. By

contrast, Yoshinobu *et al.* [9] employed the periodic introduction of Si_2H_6 and C_2H_2 to achieve 3C-SiC growth on vicinal 6H-SiC(000 $\bar{1}$) and 6H-SiC(0 $\bar{1}$ 14) substrates at 850–1160°C. Films grown on vicinal 6H-SiC(000 $\bar{1}$) contained DPBs while those grown on 6H-SiC(0 $\bar{1}$ 14) were free of these defects. Smooth films were obtained at the lowest growth rates used in the study ($< 0.01 \mu\text{m/hr}$).

B. Experimental Procedure

In the present research, SiC films were grown using a specially designed and previously described [10] GSMBE system. The base and operating pressures were 10^{-9} Torr and 10^{-3} – 10^{-6} Torr, respectively. All films were grown between 1050–1250°C using 1:1 ratios of disilane (Si_2H_6 , 99.99% purity) and ethylene (C_2H_4 , 99.99% purity) with total source inputs ranging from 0.6–4.0 sccm on off-axis α (6H)-SiC(0001) and thin 2H-AlN(0001) buffer layers on on-axis α (6H)-SiC(0001). The thin AlN layers were grown for 1 minute in the same system at 1050°C using a standard Al (99.9999% purity) effusion cell source, operating at 1260°C, and a compact electron cyclotron resonance (ECR) source to activate 3.5 sccm of N_2 (99.9995% purity). (This procedure has been described previously [11, 12]). Solid aluminum, evaporated from a standard MBE effusion cell, was used for p-type doping. Substrates were chemically cleaned prior to growth in a 10% HF solution for 5 minutes, loaded immediately into the growth chamber and then evacuated to ultrahigh vacuum. A surface pretreatment step, in which the substrates were heated to 1050°C and held for 10 minutes, exposed to a 1 sccm flux of Si_2H_6 for minute and heated to 1200°C to evaporate the Si from the surface, was performed prior to growth. The surface of the substrates was monitored using reflection high-energy diffraction (RHEED) operating at 10 kV.

RHEED was also used to determine the crystalline quality and structure of the surface of the resulting films. High-resolution transmission electron microscopy (HRTEM), operating at 200 kV, was employed to observe the microstructure of the film as well as film/substrate interfaces. Secondary ion mass spectrometry (SIMS), using 10 keV O^+ ions, was employed to determine the atomic concentration of Al. Carrier concentrations for undoped SiC films, grown on insulating AlN layers, and p-type doped films were measured at room temperature by standard Hall techniques at 3.5 kG. Nickel contacts, RF sputtered at room temperature then annealed at 1000°C for 30 s in Ar, were used on the undoped films and aluminum contacts, evaporated at room temperature and annealed at 500°C for 30 seconds in Ar, were used on p-type films.

C. Results

Film Growth. Figure 1 shows a representative HRTEM image of a homoepitaxial, undoped 6H-SiC film on a 6H-SiC(0001) substrate cut 3–4° towards $[1\bar{2}0]$. This layer was

grown for 2 hours at 1250°C using 1.0 sccm Si₂H₆ and 1.0 sccm C₂H₄. The lattice fringes seen in the image are indicative of the 6H stacking sequence. Although it is very difficult to determine the thickness of such a thin, undoped film, the thickness is expected to be about 1200 Å based on previously determined growth rates.

Figure 2 shows a HRTEM micrograph of a 3C-SiC/2H-AlN/6H-SiC heterostructure. The SiC layer was grown on approximately 1.5 nm of AlN on an on-axis 6H-SiC(0001) substrate at 1050°C for 1 hour using 0.3 sccm Si₂H₆ and 0.3 sccm C₂H₄. Similar to previous reports of growth on AlN [12, 13], the resulting SiC film is of the 3C polytype. Hall electrical characterization on thicker SiC films ($\approx 0.5 \mu\text{m}$) grown under the same conditions for longer times revealed the films to have carrier concentrations on the order of $2 \times 10^{16} \text{ cm}^{-3}$ to $1 \times 10^{17} \text{ cm}^{-3}$.

Figures 3a and 3b show RHEED photographs taken along major poles on the two SiC films described above. The photograph in Fig. 3a, taken along the $[11\bar{2}0]$ azimuth of the film shown in Fig. 1, is indicative of a smooth 6H-SiC film. Figure 3b, showing the $[110]$ azimuth of the SiC surface of the multilayer film shown in Fig. 2, shows a typical pattern for a smooth surface of 3C-SiC.

Film Doping. Carrier concentrations were measured on a number of Al-doped 6H-SiC films by the Hall technique. These films were grown under the same conditions as in Fig. 1. Four different doping levels were achieved with Al effusion cell temperatures held at 700°C, 800°C, 900°C and 1000°C. The results are shown in Table I. As expected, the carrier concentration increased as the effusion cell temperature was increased.

Table I. Measured Carrier Concentrations in Various P-type SiC Films

Aluminum Cell Temperature (°C)	Carrier Concentration from Hall Measurements (cm^{-3})
700	3.8×10^{16} *
800	5.3×10^{16}
900	8.2×10^{17}
1000	1.2×10^{18}

* Despite apparent Al incorporation, this film is still n-type according to Hall and Hot Probe analysis.



Figure 1. HRTEM micrograph of a homoepitaxial, undoped 6H-SiC(0001) film grown on a vicinal 6H-SiC(0001) substrate. Note the very large step and the wide, smooth terrace that results.

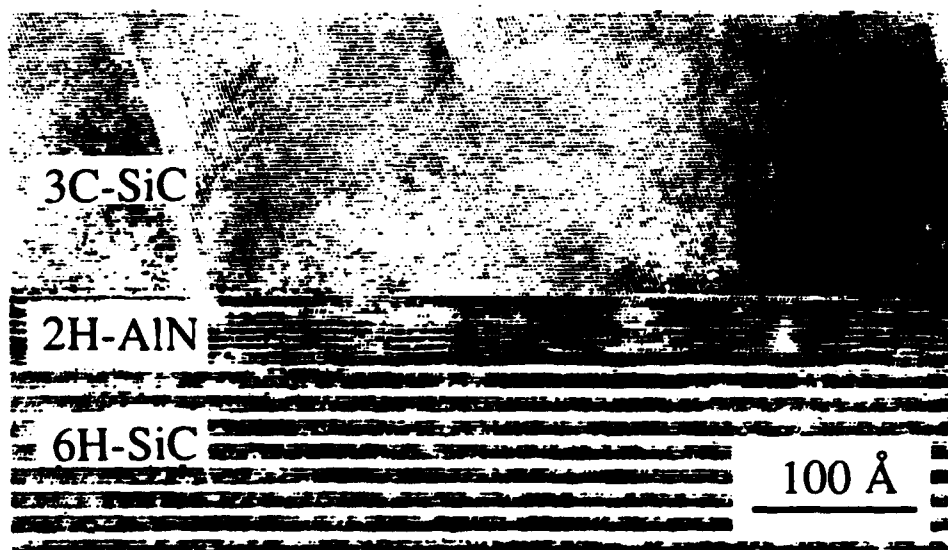
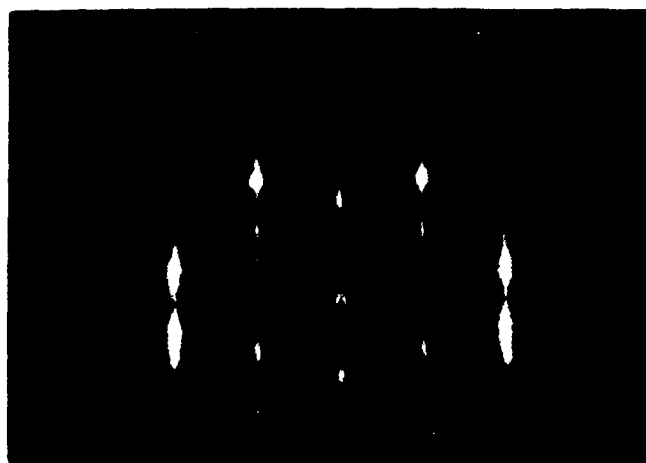


Figure 2. HRTEM micrograph of a 3C-SiC(111) film on a thin (≈ 1.5 nm) 2H-AlN(0001) layer grown on on-axis 6H-SiC(0001). Note the smooth 3C-SiC layer that results.



(a)



(b)

Figure 3. RHEED photographs of (a) the 6H-SiC film shown in Fig. 1 and (b) the 3C-SiC film shown in Fig. 2.

Figure 4 shows SIMS profiles for the same p-type films as displayed in Table I. The film having the lowest Al doping, and labeled as 700°C, is at the Al detection limit of $5 \times 10^{15} \text{ cm}^{-3}$ for the instrument. The highest doped of these films shows a very non-uniform profile due to occasional Al inclusions, observed as bright spots in the sputtering crater, within the film.

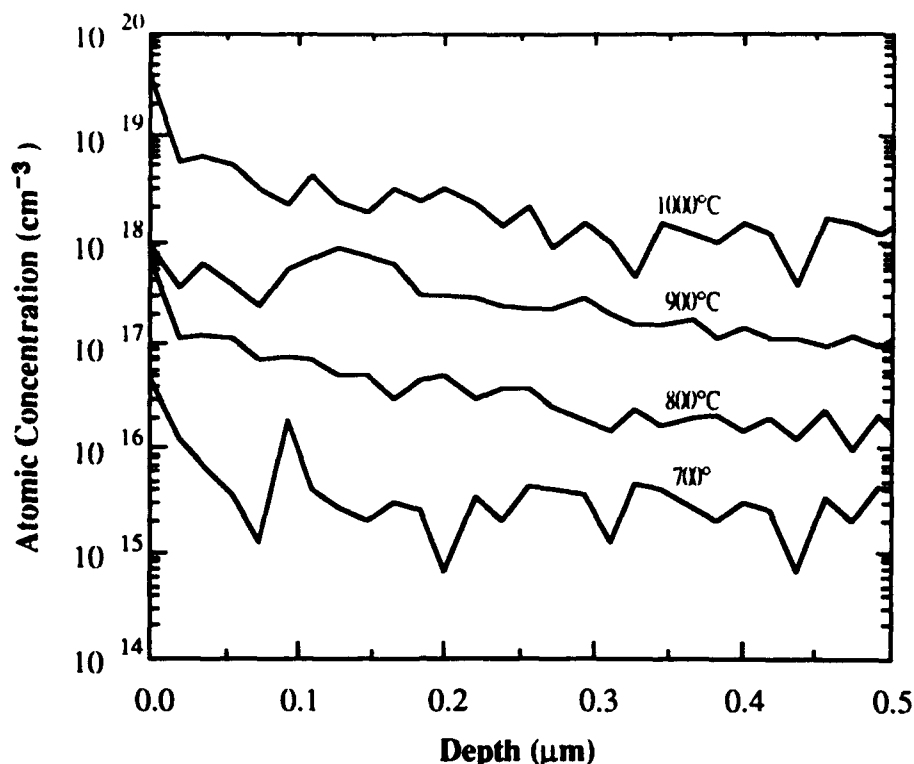


Figure 4. SIMS profiles for 6H-SiC films doped with Al from an MBE effusion cell at different source temperatures.

D. Discussion

The large surface step (≈ 15 nm or 10 unit cells) seen in Fig. 1 is most likely the result of a combination of step flow and step bunching during growth whereby different steps, which have different surface energies associated with them, grow laterally at different velocities until they impinge on one another [14]. By contrast, the majority of the film is extremely smooth with widely spaced steps. Although not yet suitable for device applications, this film represents a significant step toward that goal.

The film shown in Fig. 2 and the resulting electrical data from similarly produced films represent the best β -SiC(111) produced by this system. The role of the AlN buffer layer is not fully understood, but this film appears much smoother and less defective than 3C layers grown directly on 6H substrates [8,9].

The Hall measurements listed in Table I and the SIMS data displayed in Fig. 4 represent one of the first attempts at SiC doping by MBE. As expected, the concentration of both impurity atoms and carriers increased as the source flux increased. The high levels of Al seen at the surface in the SIMS plot are probably a result of ineffective shuttering of the solid Al source at the conclusion of growth. Gas sources can be immediately diverted to another pump but the solid source can only be shuttered while the flux decreases during cooling. This was a particular problem and a possible source of the Al inclusions observed on the

surface of the highest doped films. These profiles and the data from Table I are the same order of magnitude indicating a much higher activation efficiency than previously reported by CVD [15].

E. Conclusions

Films of 3C- and 6H-SiC have been grown between 1050-1250°C by GSMBE using Si₂H₆ and C₂H₄ on different orientations of α (6H)-SiC(0001) and on thin buffer layers of AlN. Growth of SiC on AlN represents a possible means of growing higher quality β -SiC(111) than previously reported. Hall electrical measurements on these films revealed carrier concentration of $2 \times 10^{16} \text{ cm}^{-3}$ – $1 \times 10^{17} \text{ cm}^{-3}$.

Doped films of 6H-SiC have been grown on vicinal α (6H)-SiC(0001) at 1250°C. The films (doped p-type with Al) showed atomic Al concentrations varied with increasing Al effusion cell temperature. These films showed carrier concentrations between 5.3×10^{16} and 1.2×10^{18} with the lowest Al incorporation only partially compensating the as-grown n-type character. SIMS profiles for Al incorporation are of the same order of magnitude indicating a much higher activation efficiency than previously reported by CVD.

F. Future Research Plans and Goals

Further study of SiC growth will center on the basic requirements necessary to produce device structures. These include increasing growth rate, a full understanding of polytype control, and both p- and n-type doping. In addition, studies are underway to examine the role of the thin AlN buffer layer and the relatively high dopant activation efficiency. The lone system modification necessary may be a redesign of the shuttering mechanism.

G. References

1. R. F. Davis, J. W. Palmour and J. A. Edmond, *Diamond and Related Materials* 1, 109 (1992).
2. H. S. Kong, J. T. Glass and R. F. Davis, *Appl. Phys. Lett.* 49, 1074 (1986).
3. K. Shibahara, N. Kuroda, S. Nishino and H. Matsunami, *Jpn. J. Appl. Phys.* 26, L1815 (1987).
4. H. S. Kong, B. L. Jiang, J. T. Glass, G. A. Rozgonyi and K. L. More, *J. Appl. Phys.* 63, 2645 (1988).
5. H. S. Kong, J. T. Glass and R. F. Davis, *J. Appl. Phys.* 64, 2672 (1988).
6. N. Kuroda, K. Shibahara, W. Yoo, S. Nishino and H. Matsunami, in *Extended Abstracts of the 19th Conference on Solid State Devices and Materials* (Business Center for Academic Societies, Tokyo, 1987), p. 227.
7. S. Kaneda, Y. Sakamoto, T. Mihara and T. Tanaka, *J. Cryst. Growth* 81, 536 (1987).
8. L. B. Rowland, R. S. Kern, S. Tanaka and R. F. Davis, *J. Mater. Res.*, 8, 2753 (1993).
9. T. Yoshinobu, H. Mitsui, I. Izumikawa, T. Fuyuki and H. Matsunami, *Appl. Phys. Lett.* 60, 824 (1992).

10. L. B. Rowland, S. Tanaka, R. S. Kern and R. F. Davis, in *Proceedings of the Fourth International Conference on Amorphous and Crystalline Silicon Carbide and Related Materials*, edited by C. Y. Yang, M. M. Rahman and G. L. Harris (Springer-Verlag, Berlin, 1992) p. 84.
11. L. B. Rowland, R. S. Kern, S. Tanaka and R. F. Davis, *J. Mater. Res.* **8**, 2310 (1993).
12. L. B. Rowland, R. S. Kern, S. Tanaka and R. F. Davis, *Appl. Phys. Lett.* **62**, 3333 (1993).
13. R. S. Kern, S. Tanaka, and R. F. Davis, to be published in *Proceedings of the International Conference on Silicon Carbide and Related Materials*.
14. F. R. Chien, S. R. Nutt, W. S. Yoo, T. Kimoto and H. Matsunami, *J. Mat. Res.* **9**, 940 (1994).
15. H. J. Kim and R. F. Davis, *J. Electrochem. Soc.* **133**, 2350 (1986).

VIII. Chemistry, Microstructure, and Electrical Properties at Interfaces between Thin Films of Cobalt and Alpha (6H) Silicon Carbide (0001)

I. Introduction

The extreme thermal, mechanical, and electronic properties of SiC make it an attractive material for use in both structural applications and high-power, -temperature, -speed, and -frequency electronic and optoelectronic devices. The Co/SiC system has been studied by several investigators for the applications of both structural composites and contacts for devices[1-5]. Cobalt was reported to be a good rectifying contact on n-type 6H-SiC (0001) both in the as-deposited condition and after annealing at temperatures to 800°C, while ohmic-like behavior was displayed after annealing at 900°C[4,5]. Because Ni is commonly employed as an ohmic contact to n-type SiC[6], one also might expect ohmic behavior from annealed Co contacts when considering their chemical similarities and similar work functions.

High resolution transmission electron microscopy (TEM) has been employed to investigate the interfacial chemistry and microstructure between Co and n-type 6H-SiC (0001) before and after annealing at 1000°C. The results have been compared with other chemical studies and correlated with the electrical properties measured in the present research.

B. Experimental Procedure

Vicinal, single crystal, nitrogen-doped, n-type ($\approx 10^{18} \text{ cm}^{-3}$) wafers of 1" diameter 6H-SiC (0001) containing 0.5-1.5 μm thick, n-type ($\approx 10^{16}$ - 10^{17} cm^{-3}) homoepitaxial films thermally oxidized to a thickness of 500-1000 Å in dry oxygen at 1300°C were provided by Cree Research, Inc. The epitaxial layers were unintentionally-doped except where higher doping concentrations were needed; these latter films were intentionally doped with nitrogen during growth. The Si-terminated (0001) surface, tilted 3°-4° towards $[11\bar{2}0]$ was used for all depositions and analyses.

The substrates were simultaneously cleaned and the oxide layer etched from the surface using a 10 min. dip in a 10% hydrofluoric acid solution. This was followed by a quick rinse in deionized water. The substrates were loaded immediately into a vacuum system transfer tube (base pressure $\approx 10^{-9}$ Torr), thermally desorbed at 700°C for 15 min. to remove any residual hydrocarbon contamination, and transferred to the metal deposition chamber.

A UHV, dual source 270°, 10 cc electron beam evaporator was used to deposit the Co films in a thickness range of 4-1000 Å. A 330 l/s turbomolecular pump was used for roughing the system and during processing. A 500 l/s diode ion pump and a titanium sublimation pump were employed to achieve and maintain UHV base pressures of $<2 \times 10^{-10}$ Torr. Prior to the depositions, approximately 25-50 Å was typically evaporated from the source to liberate any foreign material which may have collected on its surface. Each substrate was covered by a shutter during this operation. To commence the deposition,

the emission current was increased very slowly until a deposition rate of 10–12 Å/min was stabilized according to the thickness monitor, and the shutter subsequently removed from in front of the sample. The pressure during the depositions was between 5×10^{-9} and 5×10^{-8} Torr. Throughout each deposition the substrates were rotated to ensure uniform thickness across the sample. The substrates were not intentionally heated during the depositions.

Patterned contact structures consisting of 500 μm (0.02") and 750 μm (0.03") diameter circular contacts of 100 nm thickness were created for electrical characterization by depositing the metal through a Mo mask in contact with the substrate. Silver paste served as the large area back contact. Subsequent annealing was conducted either in UHV or in an inert gas (N_2 or Ar) ambient. Current-voltage (I-V) measurements were taken with a Rucker & Kolls Model 260 probe station in tandem with an HP 4145A Semiconductor Parameter Analyzer. Capacitance-voltage (C-V) measurements were taken with a Keithley 590 CV Analyzer using a measurement frequency of 1 MHz.

Co/SiC samples were prepared in cross-section for analysis by transmission electron microscopy (TEM). High resolution (HR) images were obtained with an ISI EM 002B operating at 200 kV with an interpretable resolution limit of 0.18 nm. These images were typically recorded at an electron-optical magnification of 590,000. Lattice spacings (d-spacings) and interplanar angles were measured from optical digital diffraction patterns and used to identify the reaction product phases. The values of the lattice spacings of unknown phases were calculated using the (0006) d-spacing in 6H-SiC near the phase to be identified to avoid d-spacing errors introduced by changes in objective lens current. The experimentally-determined d-spacings were compared to a data base of d-spacings for each possible reaction product phase. The interplanar angles of the phases having d-spacings in the data base which were within 2% of the measured values were also compared for additional assistance in the identification. Most of the measured values were within 1% of the theoretical values. Unknown phases were identified uniquely by these procedures.

Analytical electron microscopy was performed using a Philips 400 ST FEG attached to a Gatan 666 parallel electron energy loss spectrometer (PEELS) operating at 100 kV and with a spatial resolution of approximately 3 nm. For fixed position PEELS the probe position was adjusted in the diffraction mode by monitoring the shadow image in the Bragg disk of the transmitted beam. The image was created by defocusing the second condenser lens. A liquid nitrogen cooled double-tilted holder was used for all analytical experiments to minimize specimen contamination.

Surface chemistry was studied using a Riber x-ray photoelectron spectroscopy (XPS) system. This system consists of a Mac2 semi-dispersive electron energy analyzer and is accessible by UHV transfer from the deposition chamber. The Mg $\text{K}\alpha$ (1253.6 eV) x-ray

source was operated at 14 kV with an emission-controlled current of 15 mA. Scans of individual photoelectron peaks were obtained at 0.8 eV resolution and contained 500-750 data points and a 20-30 eV binding energy range.

C. Results and Discussion

Electrical Properties. As-deposited Co contacts displayed excellent rectifying characteristics with consistently low ideality factors ($n < 1.06$) and typical leakage currents of 2.0×10^{-8} A/cm² at -10 V (Fig. 1). Figure 2 shows a representative semilogarithmic I-V plot. The linear region extends over > 4 decades of current. At higher voltages the current became limited by the resistance of the substrate, and the slope was reduced. Following the procedure outlined in Ref. [7], the average Schottky barrier height (SBH) calculated from the semilogarithmic I-V plots was 1.12 eV.

Capacitance-voltage measurements plotted as $1/C^2$ vs. V yielded straight lines over a 2 to 5 V range, as shown in Fig. 3. These plots allowed the SBH to be calculated from the equation

$$\Phi_B = V_i + \xi + \frac{kT}{q} - \Delta\Phi, \quad (1)$$

where V_i is the voltage intercept; ξ is the energy difference between the conduction band minimum and the Fermi level in the bulk of the material; and $\Delta\Phi$ is the image force lowering. The extrapolated voltage intercept was -1.00 V, yielding a calculated SBH of 1.15 eV.

The SBH of thin, as-deposited Co films on SiC were also calculated from XPS analyses by comparing shifts in the C 1s and Si 2p binding energies before and after deposition of very thin metal films. The binding energies of the C 1s and Si 2p peaks were defined as the full widths at half maximum of the C-bound-to-Si and Si-bound-to-C portions of the peaks, respectively. Table I lists the corrected C 1s and Si 2p binding energies as a function of Co film thickness. According to Ref. [7], the initial band bending at the SiC surface was 284.30 eV minus 283.80 eV (C 1s), which is equal to 0.50 eV. After depositing 12 Å Co the C 1s and Si 2p binding energies were both reduced by 0.56 eV, which corresponds to an increase in band bending by the same amount. This data indicates that the SBH was approximately equal to 1.06 ± 0.1 eV.

Calculation of the C 1s and Si 2p reduced intensities as a function of Co thickness indicated that island growth occurred rather than layer-by-layer growth. The same procedure outlined in Ref. [7] for Ti contacts was used to determine the growth mechanism. For the hcp Co film ($a = 2.507$ Å, $c = 4.07$ Å), the thickness of one monolayer was taken to be 2.04 Å for the calculations. Figure 4 shows that the C 1s and Si 2p intensities were significantly higher than the theoretical intensities for layer-by-layer growth and closer to those for island growth (assuming 50% coverage). Higher substrate intensities are expected for island growth

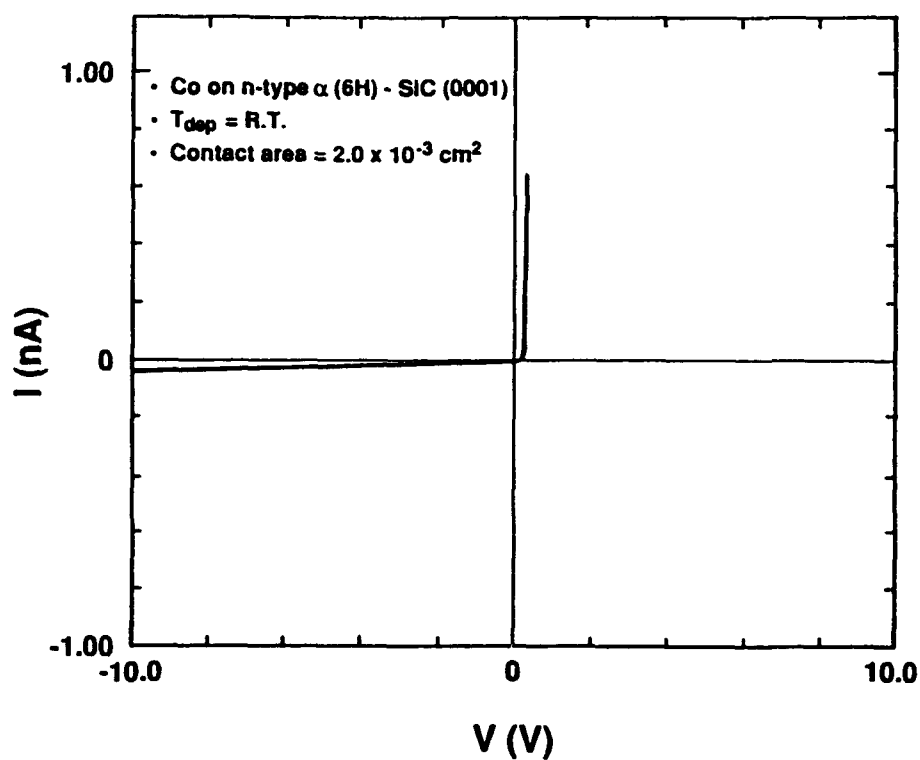


Figure 1. Representative plot of current-voltage data of as-deposited Co on 6H-SiC (0001).

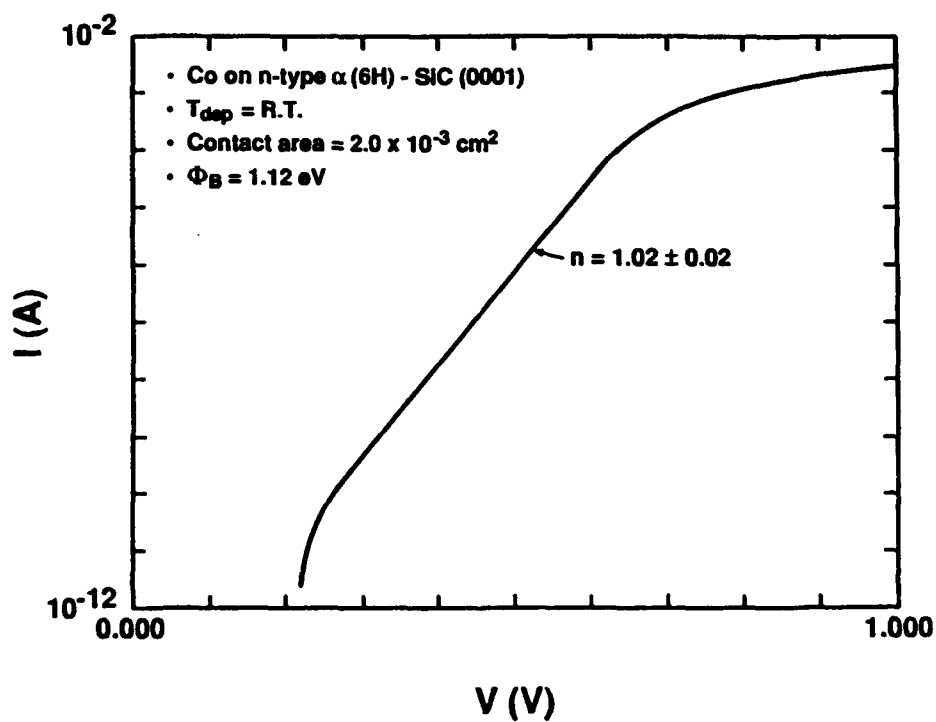


Figure 2. Semilogarithmic I-V plot of as-deposited Co on 6H-SiC (0001).

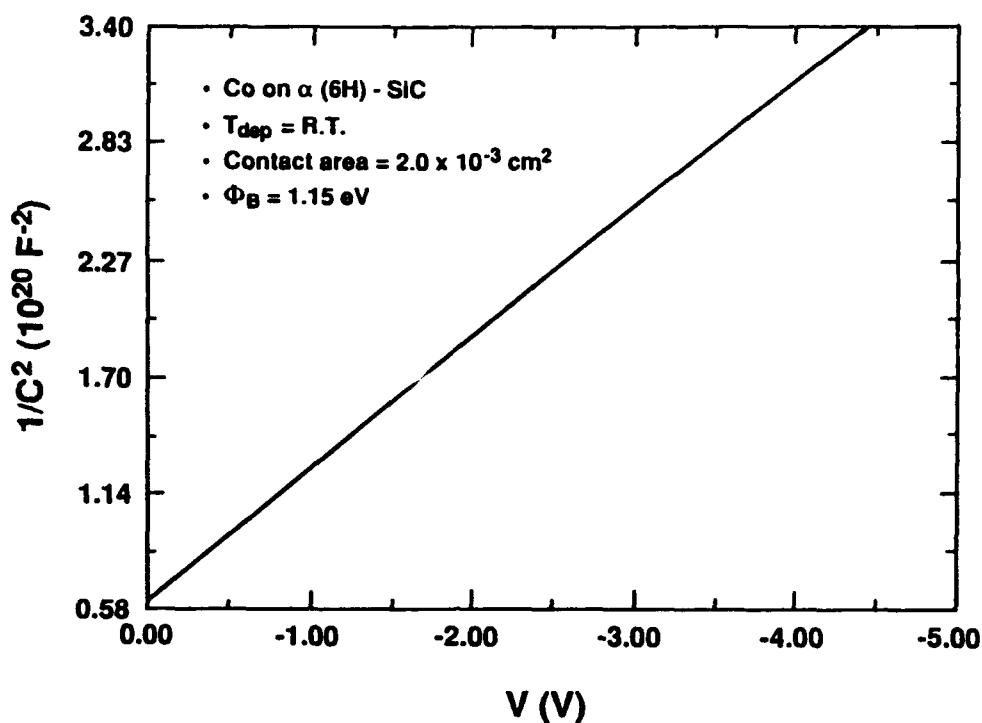


Figure 3. $1/C^2$ vs. V of as-deposited Co on 6H-SiC (0001).

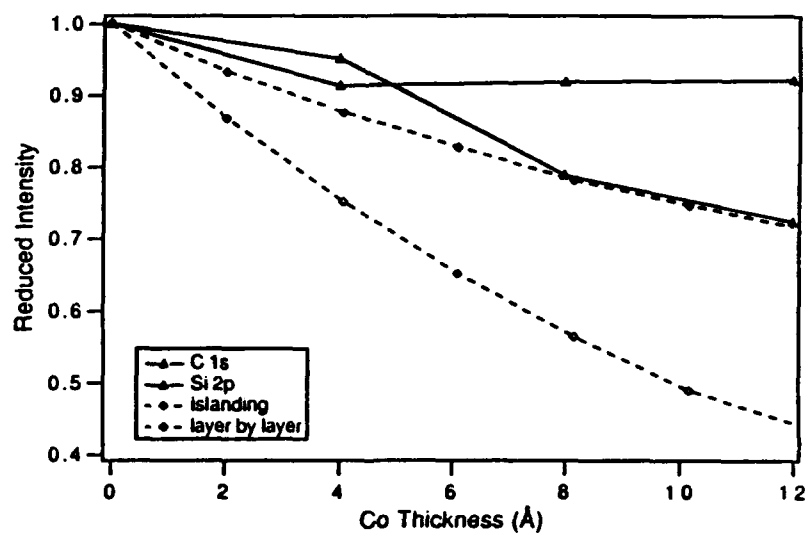


Figure 4. Plot of C 1s and Si 2p reduced intensities vs. Co overlayer thickness as measured by the growth thickness monitor. The theoretical curves represent island (Volmer Weber) growth, assuming 50% coverage, and layer-by-layer (Frank-van-der Merwe) growth.

Table I. Binding energies of C 1s and Si 2p peaks from SiC with various thicknesses of Co.*

Peak	0 Å Co	4 Å Co	8 Å Co	12 Å Co
C 1s	283.80	283.52	283.60	283.24
Si 2p	101.56	101.28	101.32	101.00

*These binding energies have been corrected according to the Au 4f_{7/2} binding energy. Units are in electron-volts.

because regions of the substrate are not covered by the deposited film. Therefore, less attenuation of the substrate peaks occurs. It is possible that complete coverage with thicker films would have resulted in more band bending in the SiC and, correspondingly, a larger calculated SBH. However, the close agreement between the values calculated from XPS and I-V and C-V measurements suggests that any change in that respect would be small. The islanding may be due to O in the film, which is discussed in a later section. The reason for the higher C 1s intensities compared to the Si 2p intensities is unknown at this time.

Annealing of thicker films (1000Å) for 20 min. at 800°C resulted in an increase in the leakage currents by an order of 10^3 to 10^6 . A few contacts displayed low ideality factors, while others displayed no linear region from which an ideality factor could be calculated. For the former the average SBH was 1.05 eV. However, the average SBH for all of the contacts was likely substantially lower than that.

Cobalt contacts were subsequently deposited onto another SiC substrate (epilayer carrier concentration of $9 \times 10^{16} \text{ cm}^{-3}$) and rapidly annealed at 1000°C for total times of 1, 2, and 3 min. This higher temperature was chosen to determine whether ohmic behavior would result, as occurs in the Ni/SiC system[6]. The resulting electrical characteristics are displayed in Fig. 5. After 1 min. the contacts displayed very high leakage currents. No ideality factors could be obtained from the log I vs. V plots. After annealing for a total time of 2 min., the contacts became either ohmic or ohmic-like. However, in most cases, annealing for 3 min. resulted in an increase in the resistivity.

Because ohmic behavior was displayed after annealing for brief periods, Co was again deposited on SiC but through a Mo mask designed for TLM measurements. The SiC substrate was n-type with a carrier concentration of $3.4 \times 10^{18} \text{ cm}^{-3}$. It contained a 3.0 μm thick, n-type homoepitaxial layer with carrier concentration $3.2 \times 10^{18} \text{ cm}^{-3}$. This sample was also annealed for 2 min. at 1000°C. The average contact resistivity was $\rho_c = 2.5 (\pm 0.4) \times 10^{-2} \Omega \text{ cm}^2$.

Microstructure. As-deposited Co films were mainly of the α-phase and polycrystalline, having a small angular range of orientations in the direction perpendicular to the substrate. In particular, (0002)_{Co} is within $\pm 5^\circ$ along (0006)_{SiC}. This orientation relationship is revealed

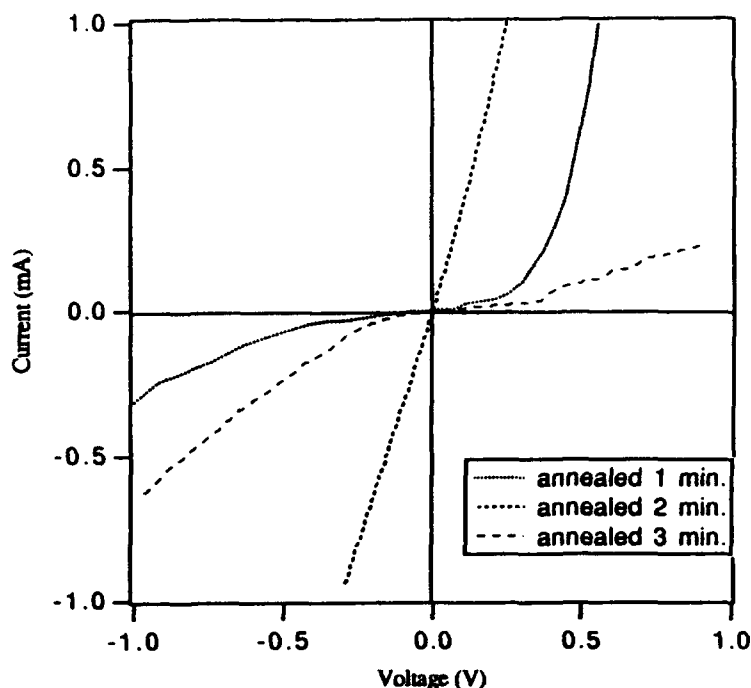


Figure 5. Current-voltage measurements of Co/SiC after annealing at 1000°C for 1, 2, and 3 min.

in the selected area diffraction (SAD) pattern in Fig. 6. A high resolution TEM image (Fig. 7) shows the high concentration of stacking faults in a representative film. An approximately 0.34 nm thick, white interfacial layer is apparent at the interface. This layer cannot be due to a new phase since the thickness is much less than the critical nucleation radius. The layer also is not attributed to ion milling damage during sample preparation, because its thickness remained constant across the sample, and no amorphous region in the Co or the SiC surrounded the layer. Considering the strain between the Co film and the SiC having the crystallographic relationship of $(0001)_{\text{Co}} \parallel (0001)_{\text{SiC}}$ to be as high as 18%, the white contrast is considered to be due to a local atomic density which is lower than the surrounding crystalline phases. Similar contrast for heterophase interfaces with large misfit strain has been reported in the literature[8,9].

Film Morphology & Phase Identification. Annealing the Co/SiC interface for 2 min. at 1000°C resulted in extensive reaction. Samples annealed under these conditions showed ohmic or ohmic-like behavior. Samples were also annealed at 800°C for 20 min., but did not produce ohmic contacts and were not analyzed by TEM. All of the Co (100 nm) and a thin layer of the SiC were consumed by the reaction at 1000°C. The low magnification TEM image in Fig. 8 shows the interface to be nonplanar, and, correspondingly, the width of the

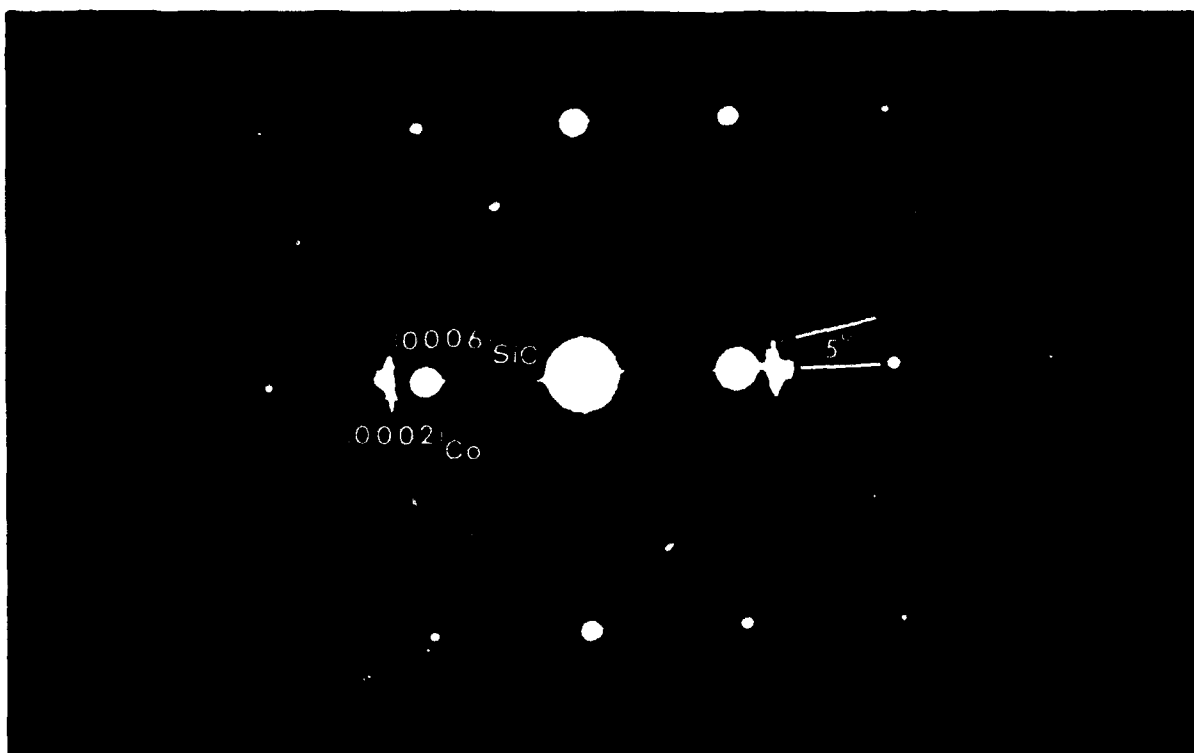


Figure 6. Selected area diffraction pattern of as-deposited Co on 6H-SiC (0001). Zone axis = $[1\bar{1}00]_{\text{SiC}}$.

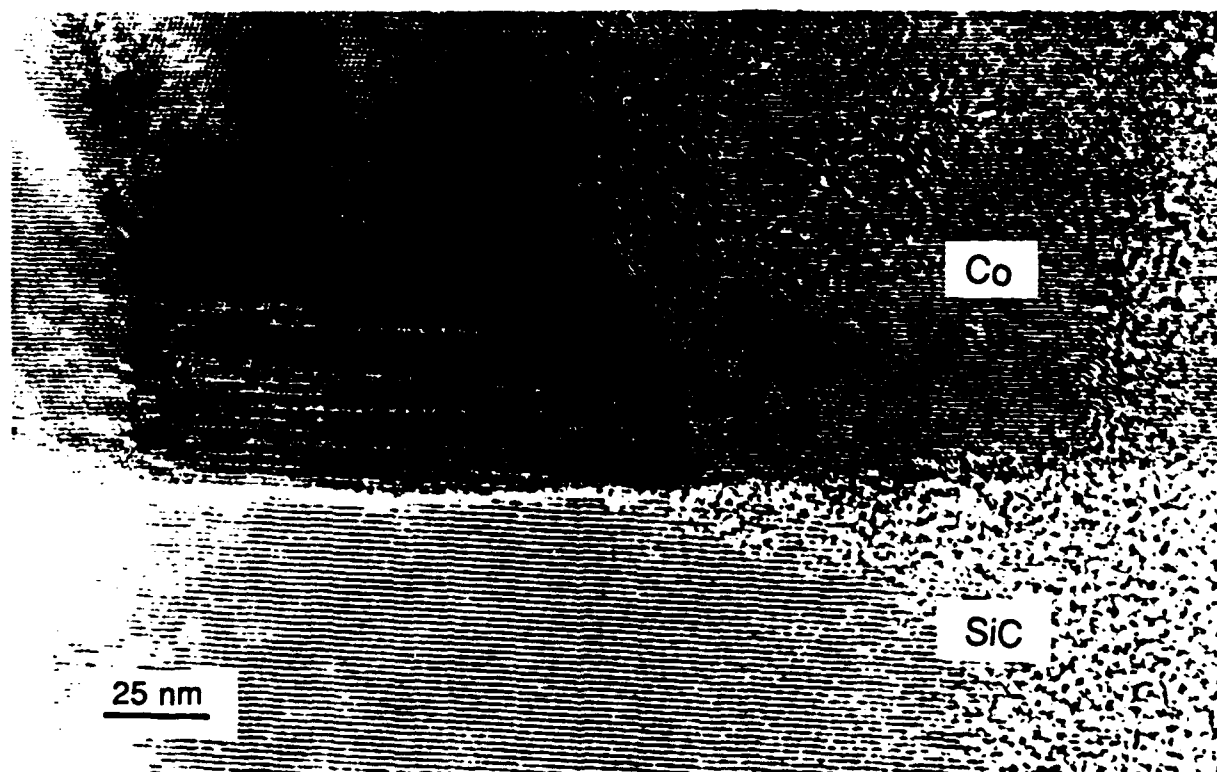


Figure 7. High resolution TEM image of as-deposited Co on 6H-SiC (0001) showing stacking faults in the film.

reaction zone varied. In fact, the narrow region of the reaction zone shown in Fig. 8 is approximately 200 nm, while the widest region is approximately 320 nm. The smooth, undulating interface morphology indicates that melting and solidification occurred during heating and cooling[1].

The reacted film may be divided into three layers according to Fig. 8. The layer adjacent to the SiC substrate is approximately 75 nm thick and is composed mainly of grains of crystalline phase(s) separated by low angle boundaries. Carbon aggregates displaying graphite fringes and which appear white in Fig. 8 are the dominant phase in the second layer. This layer is close to the original Co/SiC interface. Centered dark field (CDF) images, along with bright field (BF) images and PEELS data indicated that these aggregates were accompanied by voids.

The outermost layer contains a very long grain which is the same phase and has the same orientation to the grains in the first layer. A SAD pattern (Fig. 9) taken from this layer was indexed and the phase identified to be cubic CoSi viewed from the $[1\bar{1}2]$ zone axis. This phase also comprised the first layer, with the exclusion of one unidentified grain. The satellite spots along each main diffraction spot were attributed to double diffraction which resulted from grains with low angle grain boundaries along the electron beam path. Two orthogonal d-spacings measured from the SAD pattern and the microdiffraction pattern are 0.251 and 0.318 nm. They correspond to CoSi(111) ($d = 0.2558$ nm) and CoSi(110) ($d = 0.3132$ nm).

The higher magnification TEM image of the reacted interface in Fig. 10 shows a region of SiC protruding into the reaction zone. At the end of the protruded region, a small, faintly-observable region of SiC appears to be almost isolated from the SiC substrate. Selected area diffraction (SAD) patterns with rings corresponding to a d-spacing of 0.337 nm indicated the presence of graphite ($d(0002) = 0.3362$ nm). This and several other HRTEM micrographs revealed that graphite particles tend to contact these SiC protusions (see arrows in Fig. 10), probably to reduce the surface energy.

Nathan and Ahearn[3] studied the interface reactions between amorphous SiC (100 Å thick) and thermally evaporated thin films (50, 100, and 200 Å) of Ni and Co. A series of rapid anneals, corresponding to one temperature for each sample, was performed for 10 s at 25°C intervals between 300 and 450°C, 50°C intervals between 450 and 600°C, and 100°C intervals between 600 and 1000°C. At 1000°C samples were annealed for 60 s. After annealing the Co/SiC samples at temperatures between 400 and 600°C, Co₂Si was the only phase identified. After annealing at 1000°C, an uncertain phase, thought to be a crystalline C phase, and Co₂Si were present in the thicker samples. In the 50 Å films CoSi began to appear after 600°C annealing and higher.

In another study[1] diffusion couples were made between polycrystalline SiC, primarily β-SiC, and Pt, Co, and Ni. Before pressing the materials together the SiC and metals were

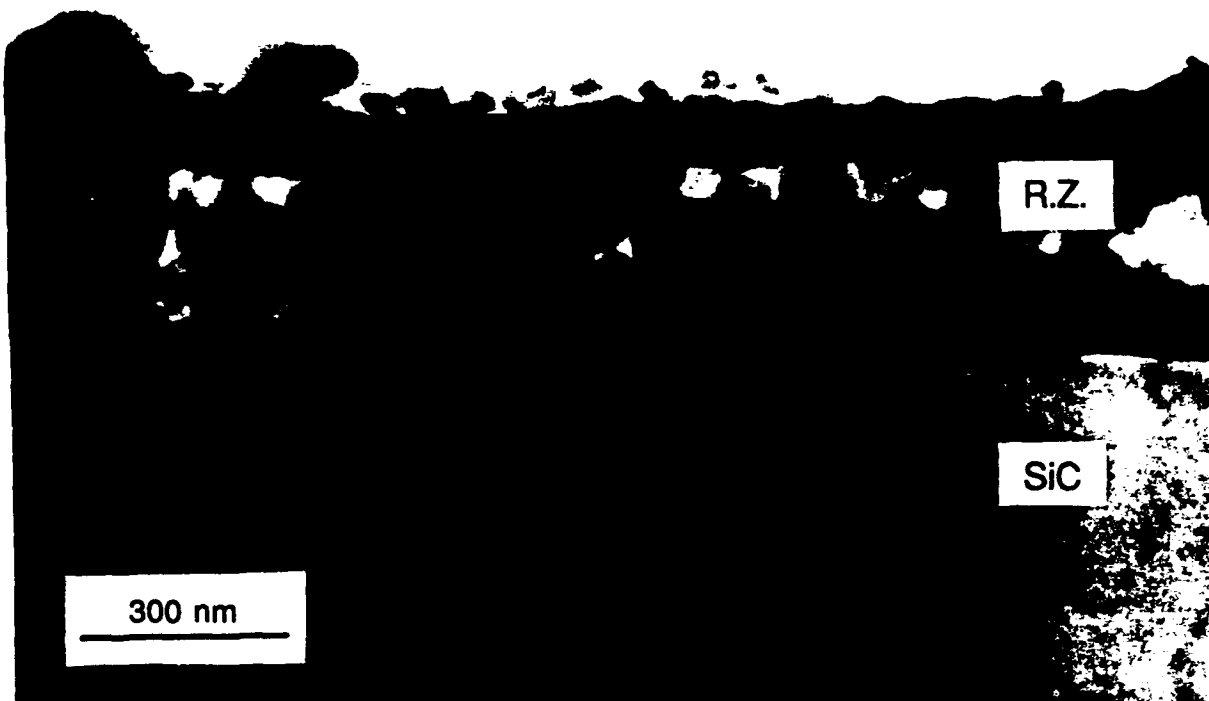


Figure 8. Low magnification cross-section TEM image of the Co/SiC interface after annealing at 1000°C for 2 min.

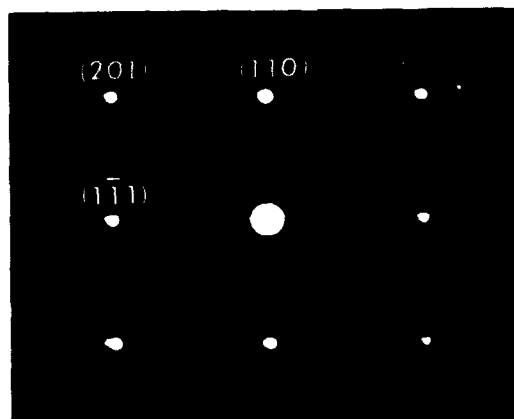


Figure 9. Selected area diffraction pattern from the outermost region of the Co/SiC reaction zone after annealing at 1000°C for 2 min. The pattern was indexed to be CoSi viewed from the $[1\bar{1}1]$ zone axis.

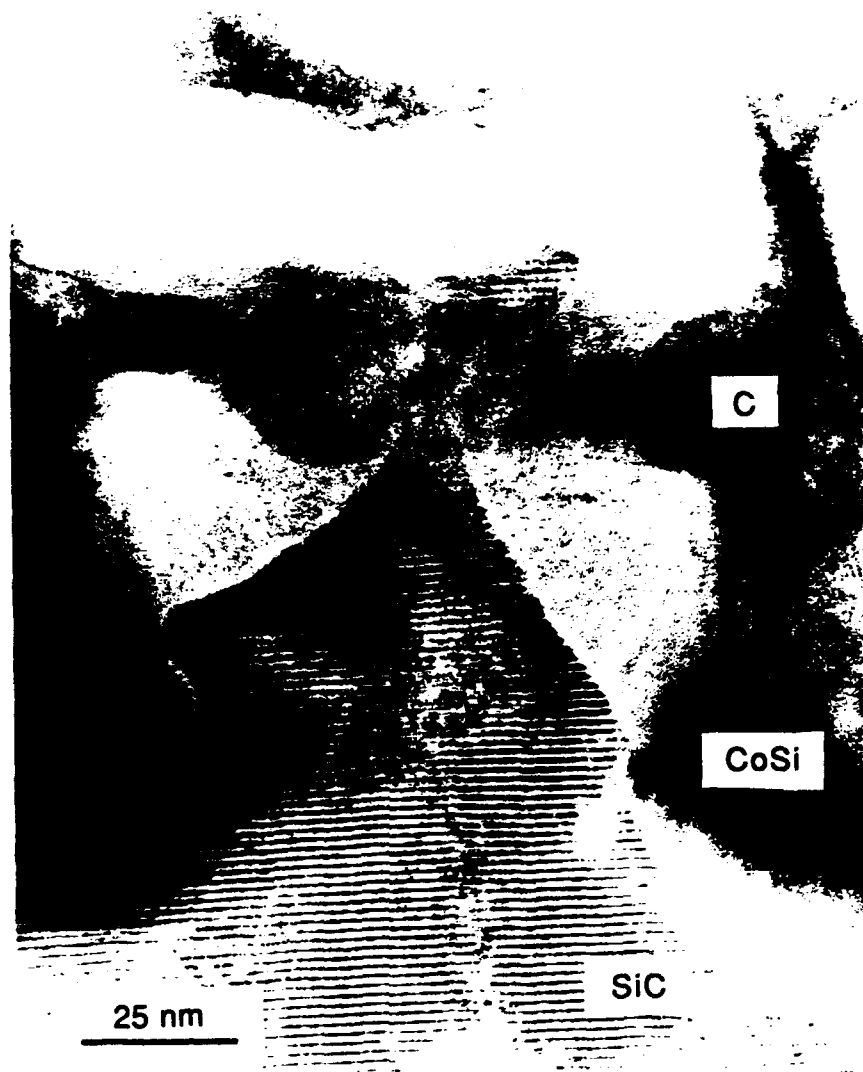


Figure 10. High resolution TEM image of Co/SiC reaction zone after annealing at 1000°C for 2 min.

polished, ultrasonically cleaned in acetone, rinsed in water, and dried with compressed air. After annealing at 1100°C for 6h, the Co/SiC reaction zone consisted of an $\approx 50 \mu\text{m}$ thick layer which contained both C precipitates and Co_2Si .

Comparing the present study with the other two studies discussed in the preceding paragraphs, it appears that Co_2Si forms in the Co/SiC system for thick and thin films of Co at temperatures between 400 and 1200°C when the Co film is not sufficiently thin as to limit the reaction. Because SiC has a very high bond strength, the initial stage of the reaction is

probably limited by the breaking of these bonds. However, once all of the Co has reacted to form Co_2Si , the evidence indicates that the reaction proceeds via the formation of CoSi .

Although CoSi was the phase in contact with the SiC after annealing for 2 min. at 1000°C , it is not believed to have inherent properties such as a low work function to cause the observed ohmic-like behavior. While the work function of CoSi (4.87 eV)[10] is less than that of Co (5.2 eV)[11], the difference should not be sufficient to account for the change. A potential future experiment would be to deposit CoSi on SiC without annealing and measure its electrical properties. Elemental doping from the contact layer, which could account for ohmic behavior, also is not likely to occur in this case. Because of the extensive reaction which resulted in highly nonuniform interfaces, it is likely that the post annealing electrical characteristics are associated with a high density of defects at the interfaces.

Interface Chemistry. Chemical bonding at the interfaces of thin, as-deposited Co films on SiC was studied with XPS. Both the $\text{C } 1s$ and $\text{Si } 2p$ peaks before and after depositing 4, 8, and 12 \AA of Co are shown in Fig. 11. The $\text{C } 1s$ peak of the uncoated SiC displayed only a Si-bound state, located at 283.80 eV. After depositing 4 \AA of Co , a small shoulder on the high binding energy side of this peak appeared. This shoulder grew substantially after depositing 8 and 12 \AA of Co . The higher binding energy indicates that the element with which the C is bound has a higher electronegativity than Si . There is no thermodynamically stable cobalt carbide. Moreover, the electronegativities of Co and Si are virtually identical; thus, Co-C bonding was ruled out as a possibility. In contrast, oxygen, has a very high electronegativity and forms oxides with Co which have large negative free energies of formation at room temperature (e.g. CoO (-214 kJ/mol) and Co_3O_4 (-795 kJ/mol)[12]). The O peak could not be monitored after depositing Co because the Co Auger peak interfered with the $\text{O } 1s$ peak. Hydrocarbons, which are reported in the literature to have a $\text{C } 1s$ binding energy of 285.0 eV[13], are another possible cause of the peak at higher binding energy. This peak would be expected to grow with increasing Co coverage as the photoelectron signal became more sensitive to interfacial C , and less sensitive to C within the bulk SiC material. This agrees with PEELS analysis which indicated O was present at a low level ($\sim 3 \text{ at. \%}$) throughout the Co film.

The fact that no bonding states other than the Si-bound state were present in the $\text{C } 1s$ peak from the clean SiC surface indicates that the O or hydrocarbons were introduced during the deposition process. It is not believed that these contaminants were introduced by a leak in the vacuum system (base pressure $1\text{--}2 \times 10^{-10}$ Torr) since they were not detected in other metal films, such as Ti , deposited in the same system. Also an Auger depth profile of the Co source revealed that O was not present at concentrations above the detection limit of the technique (1 at. %). Therefore, it is believed that the impurities were introduced either during the initial stages of the deposition or while transferring the sample through the vacuum system.

No Co silicide bonding was detected in the Si 2p peak, although three are known to exist in the Co-Si binary system[14]. Binding energies for Co-silicides were not found in the literature; however, Co-Si bonding would be expected to result in a peak at binding energies lower than the C-bound Si 2p peak. There was some evidence of enhancement of the minor O-bound Si 2p peak which was present before the deposition of Co.

D. Conclusions

A chemical, electrical, and microstructural study of as-deposited and annealed interfaces between Co and n-type 6H-SiC (0001) has been performed. The as-deposited contacts resulted in excellent rectifying behavior with low ideality factors ($n < 1.1$) and typical leakage currents of 2.0×10^{-8} A/cm² at -10 V. The SBH's calculated from XPS, I-V, and C-V measurements were between 1.06 and 1.15 eV.

After annealing at 800°C for 20 min., the contacts remained rectifying, but the leakage currents increased substantially. The contacts became ohmic-like after rapidly annealing at 1000°C for 2 min. HRTEM analyses revealed that the latter contacts were comprised of a mixture of CoSi and graphite. The reaction which formed these phases was extensive, consuming up to approximately 200 nm of the SiC. The ohmic-like behavior is likely due to defects created at the interface from the reaction.

E. Future Research Plans and Goals

The current technology of SiC devices is driving the need for ohmic contacts to p-type SiC which have low contact resistivities at both room and elevated temperatures. Aluminum alloys are currently used because the Al degeneratively dopes the surface of the SiC, which reduces the contact resistance. However, these contacts cause problems at elevated temperatures due to melting and extensive diffusion.

We are currently investigating three metal systems, one of which should be much more stable at elevated temperatures. The materials, which are comprised of 2-3 components, were chosen based on chemistry and doping considerations in addition to thermal stability. All three contact materials have been deposited onto p-type (and in one case n-type) 6H-SiC and have been characterized electrically after annealing at low-moderate temperatures.

Higher temperature anneals are planned for the contact material which has high thermal stability. For this system these temperatures are probably necessary to cause chemical reaction, which we believe will result in ohmic behavior. Once the preliminary studies involving annealing conditions and electrical properties have been performed, the chemistry and physics of these interfaces will be thoroughly investigated to understand the mechanisms related to the electrical behavior.

F. References

1. T.C. Chou, A. Joshi, and J. Wadsworth, *J. Mater. Res.*, **6**, 796 (1991).
2. T.C. Chou, A. Joshi, and J. Wadsworth, *J. Vac. Sci. Technol. A*, **9**, 1525 (1991).
3. M. Nathan and J.S. Ahearn, *J. Appl. Phys.*, **70**, 811 (1991).
4. N. Lundberg, C.-M. Zetterling, and M. Ostling, *Appl. Surf. Sci.*, **73**, 316 (1993).
5. N. Lundberg and M. Ostling, *Appl. Phys. Lett.*, **63**, 3069 (1993).
6. G. Kelner, S. Binari, M. Shur, and J.W. Palmour, *Electronics Letters*, **27**, 1038 (1991).
7. L.M. Porter, J.S. Bow, R.C. Glass, M.J. Kim, R.W. Carpenter, and R.F. Davis, Submitted to *J. Mater. Res.*
8. K.L. Merkle, M.I. Buckett, and Y. Gao, *Acta Metall. Mater.*, **40**, S249 (1992).
9. S.Q. Xiao, A.H. Heuer, and P. Pirouz, in *Proc. 50th MSA Annual Meeting*, 1992.
10. B.D. Wissman, D.W. Gidley, and W.E. Frieze, *Phys. Rev. B*, **46**, 16058 (1992).
11. C. Pirri, J.C. Peruchetti, G. Gewinner, and J. Derrien, *Surf. Sci.*, **152-153**, pt. 2, 1106 (1985).
12. *JANAF Thermochemical Tables* Journal of Physical and Chemical Reference Data, (The American Chemical Society and The National Institute of Physics for the National Bureau of Standards, Midland, MI, 1985) Vol. 14, edited by M.W. Chase Jr., C.A. Davies, J.R. Downey Jr., D.J. Frurip, R.A. McDonald, and N.A. Syverud.
13. *Auger and X-ray Photoelectron Spectroscopy* 2nd ed. Practical Surface Analysis, (John Wiley & Sons, New York, 1990), Vol. 1, edited by D. Briggs and M.P. Seah
14. *Binary Alloy Phase Diagrams* 2nd ed. (ASM International, Materials Park, Ohio, 1990), Vol. 2 edited by T.B. Massalski, H. Okamoto, P.R. Subramanian, and L. Kacprzak.

Nitrogen-based Materials

IX. Native Defects in Wurtzite GaN and AlN

P. Boguslawski,* E. Briggs, T. A. White, M. G. Wensell, and J. Bernholc
Accepted for Publication in the *Proceedings of the Materials Research Society*

Abstract

The results of an extensive theoretical study of native defects in GaN and of vacancies in AlN are presented. We have considered cation and anion vacancies, antisites, and interstitials. The computations were carried out using quantum molecular dynamics, in supercells containing 72 atoms. Due to the wide gap of nitrides, the formation energies of defects depend strongly on the position of the Fermi level. The N vacancy in GaN introduces a shallow donor level that may be responsible for the *n*-type character of as-grown GaN. Other defects introduce deep states in the gap, with strongly localized wave functions.

1. Introduction

Wide gap nitrides hold substantial promise for electronic applications. Since the electronic quality of a semiconductor is largely determined by the nature and number of its native defects and impurities, it is important to understand their properties. In wide gap semiconductors, impurity-induced shifts in the Fermi level position will have a major effect on the abundance of native defects, and thus on self-compensation and diffusion. Therefore, they will also affect growth and processing.

In GaN, *n*- and recently also *p*-type doping has been achieved [1, 2]. The quality of the material could still be improved, and the role of native defects needs to be understood, in particular for light-emitting applications, where a presence of recombination centers could lead to severe degradation. AlN has so far resisted any doping attempts, either *n*- or *p*-type. This may be due to its very wide band gap (6.3 eV), or be caused by a presence of a large number native defects.

We have embarked on a comprehensive study of native defects and impurities in GaN and AlN, focusing on identifying the dominant native defects, stoichiometry effects, and a search for effective dopants. In the following, we describe our first results regarding the electronic structure and formation energetics of point defects. We have also considered substitutional impurities and contaminants. These results will be presented elsewhere.

2. Calculations and Theoretical Aspects

The calculations were carried out using *ab initio* molecular dynamics (MD) [3] and the local density approximation (LDA). A soft non-local pseudopotential for N was generated according to the procedure of Lee and Rabii [4], while for Ga a standard non-local potential was used [5]. The kinetic energy cutoff for the plane wave basis set was 30 Ry. The accuracy of the pseudopotentials was tested by computing the lattice constants, the cohesive energies, and the bulk moduli of zinc-blende GaN and AlN. The results were in good agreement with previous calculations and experimental data [6]. Calculations for defects were carried out in a large supercell that would contain 72 atoms in the case of the perfect crystal. Due to the size of the cell, only the Γ point was used for Brillouin zone summations. To speed up the search for minimum energy configurations, the atoms were relaxed according to an efficient scheme that uses Newtonian dynamics with a special friction force for the atoms [7], while the electrons follow the motion of the atoms according to the Car-Parrinello equations [3].

Considering the limitations of the above approach, the use of supercells allows for the application of the powerful *ab initio* MD formalism, but results in broadening of the defect-

*Permanent address: Institute of Physics, Polish Academy of Sciences, 02-668 Warsaw, Poland.

and impurity-induced energy levels. This leads to an uncertainty in level positions of up to 0.5 eV in the supercell we are using. (The total energy and thus the calculated formation energies converge much more rapidly with supercell size.) The remaining source of error is due to the use of local density theory, which seriously underestimates band gaps and overestimates the cohesive energy. Even when the positions of the levels are measured from the nearest band edge, the band gap problem introduces an *additional* uncertainty of the order of 0.5 eV for deep levels. The overbinding problem is less severe, affecting the formation energies by less than 10%.

For the purposes of the present paper, we define the formation energy E_{form} of a neutral defect, *e.g.*, a nitrogen vacancy, as

$$E_{form} = E[GaN : V_N] + E_{at}(N) + \mu(N) - E[GaN], \quad (1)$$

where E is the total energy of the supercell, $E_{at}(N)$ is the total energy of the isolated N atom, and μ is taken as the experimental cohesive energy of the solid [8] except for N, where we use the binding energy of N_2 .

For charged defects, the formation energy depends on the position of the Fermi level E_F as

$$E_{form}(\Delta n) = E_{form}^0 - E_F \Delta n, \quad (2)$$

where E_{form}^0 is the formation energy for the neutral defect, and Δn is its charge.

One should stress that the definition of the formation energy (1) is not unique, since it depends on the chemical potential(s) of the atom(s). These, in turn, depend on the conditions at which the defects form during growth, processing, or annealing. If the growing solid can be assumed to be in local equilibrium with other solid phases, one can constrain the variation of the chemical potential in (1) to a range determined by the difference in the cohesive energy of the compound and that of its elements [9, 10, 7]. In some cases, the assumption of a good quality material (*i.e.*, with a low concentration of defects), restricts the values of the chemical potential to a narrow range [7, 11].

Provided that the growth proceeds under quasi-equilibrium conditions, the concentration of a defect is given by

$$Conc = N_{sites} \exp(S_{form}/k_B - E_{form}/k_B T) \quad (3)$$

where N_{sites} is the number of available sites and S_{form} is the formation entropy. Usually, the formation entropy is in the range of 4-10 k_B and the formation energy dominates.

It should be pointed out that the local equilibrium with competing solid phases may not be maintained. This is especially true if the growth process involves local excitations with ion sources and/or energetic beams, or specific kinetic conditions, *e.g.*, those corresponding to atomic layer epitaxy. In CVD, the use of complex precursors may also preclude the attainment of local equilibrium with the solid phases. In annealing experiments, the chemical potentials are determined by the nature and pressure of the gases in the annealing ampoule, rather than by equilibrium with the solid phases [11]. We postpone the investigation of these effects to a future publication and use equation (1) as a benchmark for an approximate comparison of the energetics of formation of various types of defects.

Turning to crystal symmetry issues, it is convenient to analyze the results obtained for the wurtzite structure in terms of zinc-blende symmetry with a superimposed hexagonal perturbation. In the zinc-blende structure, a substitutional defect, *e.g.*, a vacancy, has four equivalent nearest neighbors, which may be subject to both fully symmetric (breathing mode) and asymmetric relaxations. In the wurtzite structure, the atom along the c axis relative to the defect (called here type-1 neighbor) becomes inequivalent to the three remaining neighbors (called here type-2 neighbors). The lowering of the point symmetry is also reflected in the electronic structure: the defect states that are three-fold degenerate in the zinc-blende structure split into singlets and doublets in the wurtzite structure. In the following, we refer to such singlet and doublet pairs as quasi-triplets.

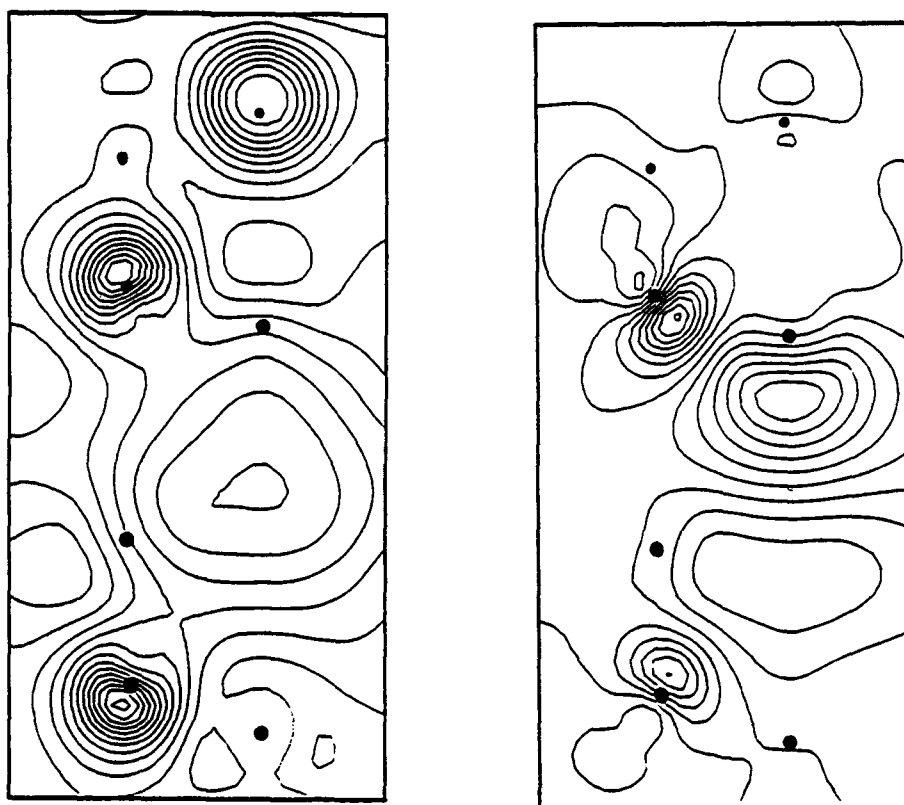


Figure 1: Contour plots of the wave functions of V_N a) the shallow donor state; and b) the conduction band resonance.

3. Native Defects in GaN

3.1. Nitrogen vacancy

The nitrogen vacancy has long been thought to be the dominant native defect in GaN, responsible for the n -type character of as-grown crystals. Our results show that the neutral N vacancy is indeed a shallow donor, with a level just below the conduction band edge. The effective-mass character of this state follows not only from the position of its energy level, but also from its wave function, which is mainly built up from wave functions at bottom of the conduction band of the perfect GaN, see Fig. 1a. This is what one expects for a shallow donor state from the effective mass theory.

The dangling-bond-like quasi-triplet state expected for the vacancy is a resonance in the conduction bands. The hexagonal symmetry results in a 0.5 eV splitting, with the singlet being lower than the doublet. The singlet is located 0.8 eV above the bottom of the conduction band. In the dangling bond model of the vacancy, the quasi-triplet level, which would have held six electrons in the perfect GaN, should contain one electron once the vacancy was created by removing the five-valent N atom. However, since the quasi-triplet is a resonance, the electron autoionizes to the bottom of the conduction bands, where it forms an effective mass state bound by the Coulomb tail of the vacancy potential.

The lattice relaxation around V_N is not very pronounced. The Ga nearest neighbor shell relaxes outwards, by 0.407 and 0.125 a.u. for type-1 and type-2 neighbors, respectively. For the neutral vacancy, the energy gain is 0.38 eV and the computed formation energy becomes 4.8 eV. It will be strongly reduced in p -type material by electron transfer from its donor level to the Fermi level. In n -type GaN, the high formation energy of V_N would indicate that it cannot be formed in sufficient concentration to account for the n -type character of the as-grown material. However, the assumption of phase equilibrium during growth may not be valid for GaN, since MBE growth involves supplying highly excited N_2 to the surface

(N_2 in its ground state is unreactive) which could result in N-deficient material. In CVD, thermal equilibrium should be easier to achieve, but thermal decomposition of TGM and ammonia may involve complicated intermediates, making simple formation energy estimates less reliable. Attainment of local equilibrium between the various solid phases also requires that the diffusion rate in the surface layers be faster than the deposition rate. At this time little is known about the mechanisms of growth of GaN, and thus the reliability of formation energy arguments cannot be assessed.

Recent high-pressure measurements in as-grown *n*-type GaN show that when high pressure is applied, the electrons that were initially in the conduction bands become localized [12]. This result indicates the presence of a resonant state in the conduction bands that emerges into the forbidden gap as the bottom of the conduction bands moves up with pressure. The electrons in the conduction bands would then become trapped in the just emerged deep level, rendering the sample insulating. We have performed calculations for V_N under pressure, and found that the quasi-triplet indeed emerges into the gap in agreement with the experimental data. The wave function of the lower (singlet) level is shown in Fig. 1b. Additional results regarding the pressure calculations will be published elsewhere.

Obviously, further data are needed for a final identification, but the good agreement between the theoretical and experimental results suggests that N vacancies are present in the samples of Ref. [12].

3.2. Gallium Vacancy

Since the formation of the Ga vacancy creates N dangling bonds, its levels should be close to the top of the valence bands. Indeed, the quasi-triplet is located about 0.4 eV above the valence bands edge, and the hexagonal splitting is only 0.1 eV. Since the quasi-triplet is populated by 3 electrons in the neutral charge state, V_{Ga} can trap both electrons and holes. In spite of the proximity to the valence band, the quasi-triplet wave functions are very localized. The wave function of the singlet is composed mainly of the $p_z(N)$ orbital of the type-1 neighbor. The contributions of the type-2 neighbors are smaller by an order of magnitude. The wave functions of the doublet are built up from the $p(N)$ orbitals of the type-2 neighbors. In this case, the contribution of the type-1 neighbor is negligible.

The formation energy of the neutral V_{Ga} is very high, 8 eV. However, since V_{Ga} can release or accept three electrons, its formation energy depends very strongly on the position of the Fermi level. In particular, in *n*-type samples the formation energy of V_{Ga}^{-3} may become very low. The thermodynamic levels for 0/-, -/2-, and 2-/3- transitions are at 0.5, 0.8, and 1.3 eV above the top of the valence band, respectively.

3.3. Nitrogen antisite, N_{Ga}

In the neutral charge state, N_{Ga} introduces a doubly occupied singlet at $E_v+0.4$ eV, and an empty doublet at $E_c-0.2$ eV. For both levels, the contribution of the type-1 neighbor is about 5 times smaller than those of type-2 neighbors. However, the singlet and the doublet do not originate from one quasi-triplet. In the initial unrelaxed configuration, there is a resonant quasi-triplet located at 0.3 eV above the bottom of the conduction band, with a vanishing hexagonal splitting. After relaxation, the splitting becomes 2.3 eV and the doublet moves to $E_c-0.2$ eV.

The dominant contribution of the type-1 neighbor is due to a strong distortion of N_{Ga} along the *c* axis. Specifically, the bond distance to the type-1 neighbor is reduced by 29% (from 3.70 to 2.62 a.u.) and becomes comparable with the bond length in the N_2 molecule, 2.07 a.u. Due to the distortion, the remaining bond lengths increase by 11%. The relaxation energy is 0.6 eV.

The formation energy of the neutral N_{Ga} is 7.3 eV. This value can be slightly reduced in strongly *p*-type samples, due to electron transfer to the Fermi level. The empty doublet at $E_c-0.2$ eV cannot be occupied even by one electron, due to the large value of the electron-electron repulsion parameter for this level (0.95 eV).

3.4. Gallium antisite, Ga_N

The gallium antisite introduces a quasi-triplet close to the middle of the band gap. In the neutral charge state, the singlet at $E_v+1.4$ eV and the doublet at $E_v+2.1$ eV contain two electrons each. The wave function of the singlet is mainly a bonding combination of the p_z orbitals of Ga_N with the orbitals of the type-1 neighbor. Similarly, the doublet is mainly a bonding combination of $p_{x,y}$ of Ga_N with p orbitals of the type-2 neighbors. However, the p orbitals from the second neighbor N atoms contribute considerably to both the singlet and the triplet.

As expected, we find an outward relaxation around Ga_N , with a large relaxation energy of 3.9 eV. The bond lengths with type-1 and type-2 neighbors are 4.12 and 4.27 a.u., respectively. The formation energy of Ga_N in the neutral state is 6.0 eV, but it is reduced strongly in highly doped samples due to electron transfer to/from the Fermi level.

3.5. Interstitials

For substitutional defects, the local topologies of zinc-blende and wurtzite lattices are similar, since in both cases each atom has four first neighbors with tetrahedral symmetry. The difference between the two structures begins at the second shell of neighbors. This is why the electronic structures of vacancies and interstitials in both structures are similar. In contrast, the local topologies of interstitials are quite different in the two lattices. In zinc-blende crystals there are two interstitial sites with tetrahedral symmetry, surrounded by four cations and four anions, respectively. In the wurtzite structure, there are two high-symmetry interstitial positions, referred to as 'tetrahedral' (T) and 'octahedral' (O) in the literature [13]. These terms are misleading, since they do not correspond to the actual point group symmetry, which is C_{3v} in both cases. In the ideal wurtzite lattice, an atom at the O site has six first neighbors, three cations and three anions. An atom at the T site has two first neighbors, one cation and one anion, and six second neighbors (three anions and three cations). Due to the point symmetry, neither T nor O can be the equilibrium position of an interstitial defect, except by accident. In particular, a relaxation along the c axis is expected.

Indeed, we find that both T and O positions are highly unstable for native interstitials. The interstitials move towards the first neighbor of the same kind. For the N interstitial, starting from both T and O positions leads to the same final configuration. At present, we are investigating whether an analogous effect also holds for the Ga interstitial.

After relaxation, N_I assumes a bridge-bond configuration similar to the bridge-bond geometry of As interstitial in GaAs, as discussed by Chadi [14]. The N-N bond length is 2.64 a.u., which is very close to the N-N distance in the case of N_{Ga} . Both N atoms move off the c -axis, and the resulting configuration is asymmetric. The relaxation energy is 7.6 eV, due to interstitial motion of over 2 a.u. Considering the electronic structure, N_I introduces two closely spaced deep levels at about $E_v+1.0$ eV, separated by 0.06 eV. Both are built up from the orbitals of the N-N pair and are occupied by three electrons. The formation energy of N_I^0 is 2.9 eV, but it will be strongly reduced in highly doped samples.

The Ga_I , initially at the T position, undergoes a displacement of 1.2 a.u., which leads to an energy gain of 8.9 eV. As mentioned above, the equilibrium configuration is similar to the bridge-bond geometry of interstitial Ga found by Chadi, but in GaN both Ga atoms are exactly along the c axis. The Ga-Ga distance is 4.17 a.u., which is close to the average Ga-Ga distance for Ga_N .

Turning to the electronic structure, Ga_I^0 introduces a deep level at $E_v+0.5$ eV, occupied by two electrons, and a resonance at $E_c+0.8$ eV. The remaining Ga electron autoionizes from the resonance and is trapped in a shallow, effective mass state. The deep Ga_I state is composed of displaced host Ga orbitals and the three N neighbors. The formation energy of a neutral $\text{Ga}(T)$ is 5.1 eV, but it will be strongly reduced in p-type samples.

4. Vacancies in AlN

We have extended the computations to the second important nitride, AlN, and considered both vacancies. Their electronic structures and formation energies are very close to the corresponding values in GaN. Specifically, V_{Al}^0 introduces a quasi-triplet at $E_v+0.4$ eV, split by 0.05 eV. It is occupied by 3 electrons. Its formation energy is 8.05 eV, which is smaller by 0.05 eV from that of V_{Ga}^0 . V_N introduces a quasi-triplet at $E_c+0.2$ eV. The hexagonal splitting is 0.6 eV and the singlet is below the bottom of the conduction band. The formation energy of V_N^0 is 5.4 eV, compared to 5.0 eV in GaN.

5. Summary

We have calculated the electronic structure and formation energies of native defects in wurtzite GaN by *ab initio* molecular dynamics. In most cases, the relaxation around the defect is substantial, strongly influencing the energy levels and formation energies. This is particularly true for interstitials. We have investigated two possible high-symmetry interstitial sites, the so-called *T* and *O*. In these high-symmetry positions both Ga and N interstitials are highly unstable. After a displacement of 1-2 a.u., both atoms form split interstitial configurations that are lower in energy by 5-9 eV. Due to the large value of the forbidden gap, formation energies depend strongly on the position of the Fermi level. The low-formation energy defects are V_{Ga} , Ga_N , and N_I in n-type samples, and V_N , Ga_N , Ga_I , and N_I in p-type samples. Our results confirm the widely held hypothesis that V_N is a shallow donor, which may be responsible for the n-type character of as-grown GaN. We have also considered common dopants and contaminants in GaN and AlN. The results of these investigations will be presented elsewhere.

This work is supported by ONR and NSF.

6. References

1. R. F. Davis, *Physica B* **185**, 1 (1993).
2. S. Strite and H. Morkoc, *J. Vac. Sci. Technol. B* **10**, 1237 (1992).
3. R. Car and M. Parrinello, *Phys. Rev. Lett.* **55**, 2471 (1985).
4. G. Li and S. Rabii, preprint.
5. G. B. Bachelet, D. R. Hamann, and M. Schluter, *Phys. Rev. B* **26**, 4199 (1982); X. Gonze, R. Stumpf, and M. Scheffler, *Phys. Rev. B* **44**, 8503 (1991).
6. R. W. L. Lambrecht and B. Segall, *Mat. Res. Soc. Symp. Proc.* **242**, 367 (1992); V. Fiorentini, M. Methfessel, and M. Scheffler, *Phys. Rev.* **47**, 13353 (1993); K. Miwa and A. Fukumoto, *Phys. Rev. B* **48**, 7897 (1993).
7. C. Wang, Q.-M. Zhang, and J. Bernholc, *Phys. Rev. Lett.* **69**, 3789 (1992).
8. C. Kittel, *Introduction to Solid State Physics*, Wiley and Sons, New York (1986).
9. S. B. Zhang and J. E. Northrup, *Phys. Rev. Lett.* **67**, 2339 (1991).
10. D. B. Laks, C. G. Van De Walle, G. F. Neumark, and S. T. Pantelides, *Phys. Rev. Lett.* **66**, 648 (1991).
11. B. Chen, Q.-M. Zhang, and J. Bernholc, *Phys. Rev. B* **49**, 2985 (1994).
12. P. Perlin, H. Teyssie, and T. Suski, to be published.
13. R. Boyn, *Phys. Stat. Solidi (b)* **148**, 11 (1988). M. A. Robertson and S. K. Estreicher, *Mat. Res. Soc. Symp. Proc.* **242**, 355 (1992), denote these sites by *T* and *R*, respectively.
14. J. D. Chadi, *Phys. Rev. B* **46**, 9400 (1992).

X. Growth of Aluminum Nitride Single Crystals Via Sublimation Method

A. Introduction

Many high-frequency and high-temperature electronic and optoelectronic device applications are in strong demand of a suitable material that could perform without deterioration under the conditions imposed by the application. Aluminum nitride, among other III-V compounds, is an excellent choice as a material for active and passive components in electronic circuits for such applications. Also, because of its high electrical resistivity ($>10^{13}$ W-cm) and good thermal conductivity (2W/cm-K) [7], it can be used as a substrate material to carry the silicon chips containing these circuits. Due to its large band gap (6.2 eV @ 300K), aluminum nitride is frequently considered for use for optical devices which can operate throughout the entire visible spectrum and into the medium, ultraviolet wavelengths. Having the highest ever reported surface acoustic velocity [1] value, AlN is a candidate for many piezoelectric applications. Excellent review articles are available for further information on aluminum nitride [2-5]. However, all proposed applications are still waiting for good-quality aluminum nitride single crystals. It is the purpose of this research to investigate a suitable method and establish growth conditions for producing bulk aluminum nitride single crystals.

Due to its high melting point and its instability near the melting temperature, most AlN single crystal material has been grown from the vapor phase. When the literature is reviewed, it can be seen that the majority of research on growth of aluminum nitride has been concentrated on chemical vapor transport due its easy integration to the present semiconductor technology. However, no one has yet reported producing single bulk crystals of AlN.

Aluminum nitride evaporates at appreciable rates above 1800°C and under 1 atm pressure. Sublimation takes place according to the following reaction:



Although thermodynamically a very small amount of AlN(g) should exist upon sublimation, it has not been detected. See Fig. 1. The exact mechanism of sublimation is not known i.e., whether or not Al and N becomes adsorbed on the surface prior to evaporation; but once nitrogen leaves the surface, the existence of N₂ inevitable for experimental conditions employed in this research. It has been calculated that at 2000 °C half time of a nitrogen atom leaving the evaporation surface is 10^{-4} – 10^{-3} seconds [11]. From the simple diffusion equation, $X=(Dt)^{1/2}$, it can be calculated that at any distance greater than 2.5μm from the surface, nitrogen will be in its diatomic form.

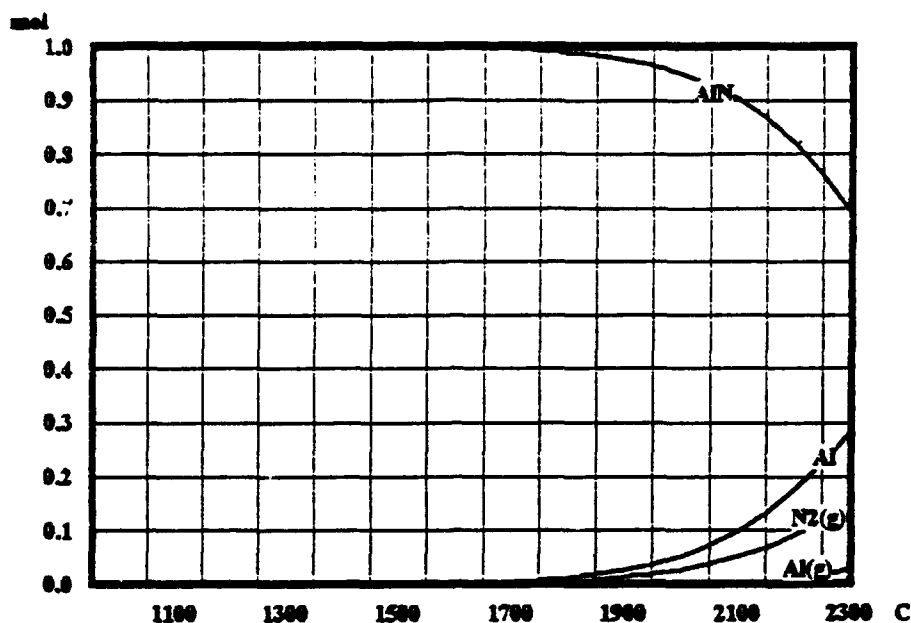


Figure 1. Sublimation behavior of AlN[12], amount of AlN(g) is negligible.

B. Experimental Procedure

As stated in the previous section, the chosen method to grow aluminum nitride crystals in the present study involves the sublimation of a polycrystalline AlN source. The basic idea is to create a temperature difference (20-100°C) between the source and the substrate and by this way to recondensate the sublimed AlN on the substrate. For this purpose, a vertical graphite furnace was utilized. The furnace used has a natural (built-in) temperature gradient due to its shape. See Fig. 2 for details of the experimental set-up.

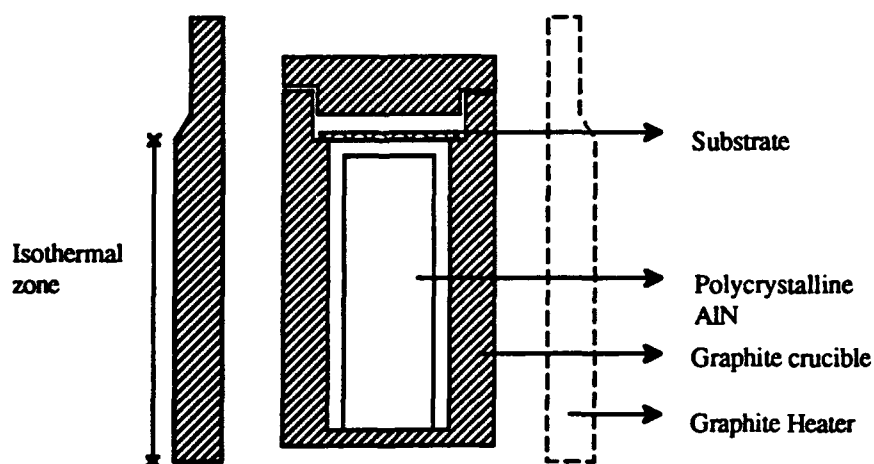


Figure 2. Configuration used for sublimation growth of AlN.

To begin the study, while the pressure was kept at 1 atm, temperatures in the range of 1850°C to 2300°C were experimented for a suitable evaporation rate for the polycrystalline AlN. It was our finding that for an efficient growth process temperature of the polycrystalline source must be between 2000°C and 2200°C at 1 atm. The evaporation rates at this temperature range changes roughly between 30mg and 1000mg/hr. Although temperature gradient was primarily controlled by furnace characteristics, by varying the substrate height with respect to the source a temperature difference of 80 to 100°C was obtained. It is essential to have a smaller difference as the evaporation temperature is lowered. The reason being molecules that are reaching the surface need enough thermal energy or surface mobility to arrange them in a orderly manner to form a solid coating. When this requirement was not met, material morphology ranging from loosely-bonded powder to individual crystal chunks were obtained.

The substrate to source distance is another crucial parameter in this method. Distances from a few mm to 3-4 cm were tested for suitability for the process. One very distinct effect of separation distance on growth is that, as the separation increases the deposition yield drops drastically. As an example, the deposition yield at 3 mm is roughly 30 times more than the yield at 15 mm separation. Most promising results were obtained at separation distances in the range of 1 to 5mm.

Due to its small lattice mismatch and stability at the temperatures employed, single crystal SiC wafers were used as substrate. Also, SiC substrates coated with thin layers of AlN by molecular beam epitaxy were used in some experiments but no conclusive results have been obtained yet.

Pressure was kept at 1 atm in the majority of the experiments since already there exists a number of parameters that can be varied. The only net effect that was observed by lowering the system pressure was the increased evaporation rate of the source material. All the experiments were carried out under nitrogen atmosphere.

Table I. Typical Growth Parameters

Substrate temperature	2100°C - 2150°C
Source temperature	2000°C - 2250°C
Pressure range	200 torr - 760 torr
Source - substrate separation	1 mm - 40 mm

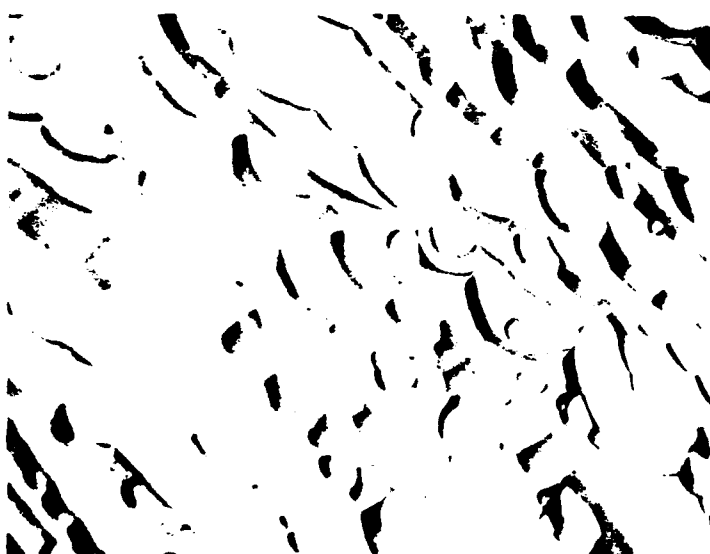


Figure 3. AlN on SiC: a) center of the sample, b) towards the edge of the crystal layer.

C. Results and Discussion

AlN single crystals were grown on SiC substrates. The layers were approximately 0.4 to 1 mm in thickness. Transparent layers were blue to dark green in color. This is most probably due the incorporation of C and O as impurities. The grown layers in general had smooth

surfaces but there were areas that the steps can be seen which indicate a step-flow growth mechanism (see Fig. 4). A range of growth parameters were obtained for sublimation growth aluminum nitride. Best results were obtained at 3-4 mm separation at 2200°C source temperature and 2150°C substrate temperature. Resulting deposit was proven to be AlN by X-rays. Laue diffraction patterns indicate that the material is indeed single crystal.

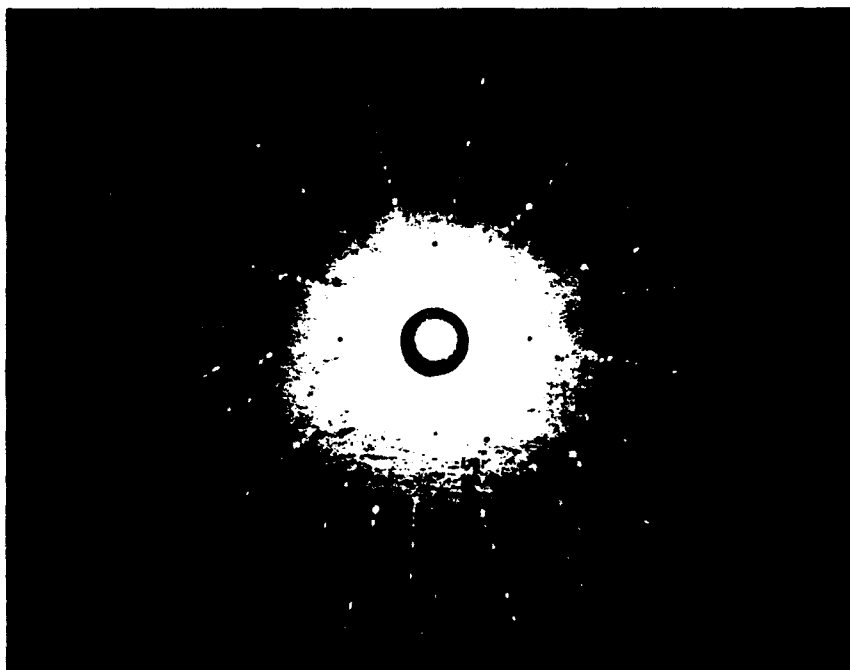


Figure 4. Laue diffraction pattern of AlN grown by sublimation.

A major difficulty faced was to maintain a constant temperature gradient as crystals grows. It is essential to keep the growth conditions constant at the growing surface of the crystal for monocrystalline growth. Crystals were also grown when the substrate was in the isothermal zone of the furnace. The fact that there is a net transfer of material under this condition and SiC preserving its structural integrity indicates another mechanism that is in effect during the creation of the temperature gradient. The only explanation to this is the fact that single crystal SiC is transparent to radiation and absorbs less heat than its surroundings. This phenomena, although by other scientists, was never explained. Another very important conclusion of this study is the necessity of having a continuous source feed. During the evaporation process there are two fluxes that one needs to be concerned with. The first one is the flux from the polycrystalline source to the substrate and the second one is the evaporation from the substrate. Naturally for a crystal to grow, the former must be higher. When the process is started, this condition is satisfied but since not every Al and N atom that leaves the

source surface transforms back in to AlN on the substrate as time passes the distance between the source and substrate becomes greater. At this point, as previously mentioned, yield starts dropping drastically. Finally there comes a point when the flux from the growing surface exceeds the incoming material flux. Extended experiments done with the intention of growing long crystals on the contrary resulted in loss of previously deposited material. Efficiency in depositing AlN has always been observed to be low, even in thin film research and this point needs to be accounted for bulk single crystal growth.

D. Conclusions

Results obtained from the experiments conducted to date indicates that deposition of single crystal AlN has a high feasibility with an improved design. Also, at the temperatures employed, deterioration of the crucible created difficulties to a certain extent. Formation of aluminum carbide can also account for some loss of aluminum that evaporated from the source. It has been proven that the idea of creating a temperature gradient and solidifying the sublimed material on a cool substrate is indeed an efficient way to grow bulk single crystals of aluminum nitride. Growing longer crystals will require a better equipment design.

E. Future Plans and Goals

The above described method will be further investigated for bulk crystal growth of aluminum nitride. To grow thicker crystals, it is necessary to design a new system where the growth conditions could be kept constant throughout the growth process. In an improved design, localized heating of the source should be considered. It was observed that a considerable amount of AlN evaporated from the bottom part of the source since it was in direct contact with the graphite crucible.

F. References

1. G. R. Kline and K. M. Lakin, Proc. IEEE Symp. Ultrasonics 14, 340 (1983).
2. M. T. Duffy, in Heteroepitaxial Semiconductors for Electronic Devices, G.W. Cullen and C. C. Wang, Eds., Springer Verlag, Berlin, pp.150-181 (1978).
3. R. F. Davis, Proc. IEEE 79, 702 (1991).
4. S. Strite and H. Morkoc, J. Vac. Sci. Technol. B 10, (1992)
5. J. H. Edgar, J. Mater. Res. 7, 235 (1992).
6. C. O. Dugger, Mat. Res. Bull. 9, 331, (1974).
7. G. A. Slack and T. F. McNelly, J. Crys. Gro. 34, 263, (1976).
8. G. A. Slack and T. F. McNelly, Final technical report, AFOSR Contract F44620-76-C-0039K, March (1978).
9. P. Bhattacharya and D. Bose, Jap. J. Appl. Phys. 10, L1750, (1991).
10. A. T. Collins, E. C. Lightowers, P. J. Dean, Phys. Rev. 158, 883 (1960).
11. P. M. Dryburgh, The Ninth International Conference on Crystal Growth, ICCG-9 (1989).
12. HSC Chemistry, Chemical Reaction and Equilibrium Software. Outokumpu Research, Finland.

XI. Initial Stage of Aluminum Nitride Film Growth on 6H-Silicon Carbide by Plasma-assisted, Gas-source Molecular Beam Epitaxy

A. Introduction

AlN has attractive characteristics such as a direct wide band gap of 6.28eV at 300K [1], high melting point of over 2275K [2], and a thermal conductivity of 3.2W/cmK [3]. Thus it is a candidate material for high power and high temperature microelectronic and optoelectronic applications. The multilayer heterostructures of GaN/AlN [4] and SiC/AlN [5] have also been considered interesting materials for the above mentioned applications. Recently, in addition to its device applications, AlN has been recognized the usefulness of this material as a buffer layer for the growth of GaN and InN on SiC and Sapphire substrates because of its intermediate lattice constant [6, 7, 8], e.g. the lattice constants of the *a*-axis of these materials are 3.189Å (2H-GaN), 3.112Å (2H-AlN) and 3.08Å (6H-SiC), and thermal expansion coefficient [6, 7]. It is of great importance to obtain very smooth and defect free AlN films in order to grow high-quality films subsequently. For the growth of multilayered structures such as GaN/AlN/SiC [8] and SiC/AlN/SiC [5], the smoothness of each layer would be especially desired. Smoothness in general is determined by growth modes, i.e. two-dimensional versus three dimensional growth. To obtain an atomically smooth surface, it should be necessary to grow films with a two-dimensional growth mode or step flow growth. In this study, the initial stages of AlN film growth on 6H-SiC substrates were investigated by cross-sectional HRTEM observation in terms of growth mode and defects at the interfaces. The effect of the vicinal surface of the substrate on AlN film growth is especially studied.

B. Experimental Procedure

AlN films were grown on Si faces of 6H-SiC (0001) substrates. The substrates used in this study were either on-axis or vicinal (3-4° off from (0001) toward $\langle 11\bar{2}0 \rangle$) provided by Cree Research Inc. [9] All films were grown by plasma-assisted gas source molecular beam epitaxy under the same conditions. Solid Al (99.999% pure) was evaporated from a standard effusion cell. Nitrogen gas (99.9995% pure) was decomposed by an electron cyclotron resonance (ECR) plasma in the vicinity of the substrate. The detailed description of the deposition technique can be found in Ref.[10]. The as-received substrate was dipped in 10% HF solution for 5 min. to remove the surface protective silicon oxide layer (typically ~750Å in thickness), immediately followed by loading into MBE system. The substrate was annealed at 1050°C in an ultra high vacuum environmental ($\sim 1 \times 10^{-9}$ torr) for 5 min. prior to the deposition in order to remove residual hydrocarbons and silicon oxide. The typical growth conditions are shown in Table I. In order to observe the initial stages of growth, the thickness of the films was controlled by varying the growth time. After growing the film, the sample was cut and glued

face to face to make a cross-sectional TEM sample, followed by the standard sample preparation techniques [11]. Finally, the sample was examined by a Topcon EM-002B operated at a 200kV acceleration voltage with the use of the $\langle\bar{2}110\rangle$ zone axis.

Table I. Growth Conditions for the AlN films

Temperature	1050 °C
Al evaporation temperature	1260 °C
Nitrogen flow rate	3.5 sccm
Microwave power	100 W
Growth rate	~17 Å/min

C. Results and Discussion

Figure 1 (a) and (b) shows the initial stage of a deposited AlN film on both on-axis and vicinal 6H-SiC (0001) substrates, respectively. The films show epitaxial 2H (wurtzite) structure which has an ABAB stacking sequence in the $\langle 1000 \rangle$ direction, referring to 'ABC' notation. The thickness of the AlN film is ~15Å. Very smooth surface morphological feature and uniformity in thickness can be seen in the AlN film grown on the on-axis substrate (Fig. 1 (a)), indicating a two-dimensional growth mode in this thickness range. In contrast, slightly rougher surface feature can be observed in the AlN film grown on the vicinal surface. Surface roughness is strongly related to the presence of steps in the vicinal surface as indicated by the arrows. Steps may play a role to confine adatoms to create an island within the terrace sites due to step site barriers caused from the strained field of AlN films. This will be discussed later with the use of the structural model at the interface. Higher magnification images of each film, shown in Fig. 2 (a) and (b) can clearly describe the detail of the structures. In Fig. (a), an atomically smooth AlN film surface and an abrupt AlN/SiC interface are seen in the film of the on-axis substrate. The AlN film consists of 5-6 'bi-atomic' monolayers (one 'bi-atomic' layer includes Al (Si) and N (C) layers). On the other hand, island-like surface feature can be observed in the film of the vicinal substrate (Fig. (b)). An island forms on a terrace site which is separated by the steps at each end (see arrows for steps). The film thickness varies from 3-4 to 7-8 monolayers. Coalescent regions of each island have a disordered atomic configuration and form 'valleys' due to misalignment of each island.

In Fig. 3, a model of the AlN/SiC interface including one bi-monolayer step, indicates an anti-phase domain boundary (APB) at the step site. AlN nuclei having ABAB stacking sequence on both of the terrace sites fail to align at the step site because of the difference in the level of 6H-SiC stacking. An 'A' layer of 2H-AlN crystal is rotated 60° from a 'B' layer in the $[1000]$ direction. This model was established on the basis of an assumption: the first AlN layer

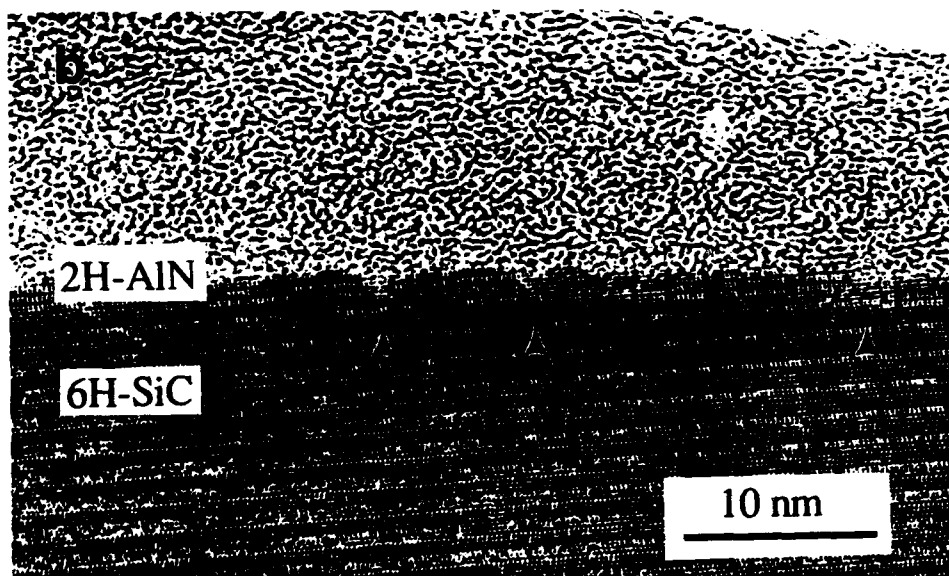
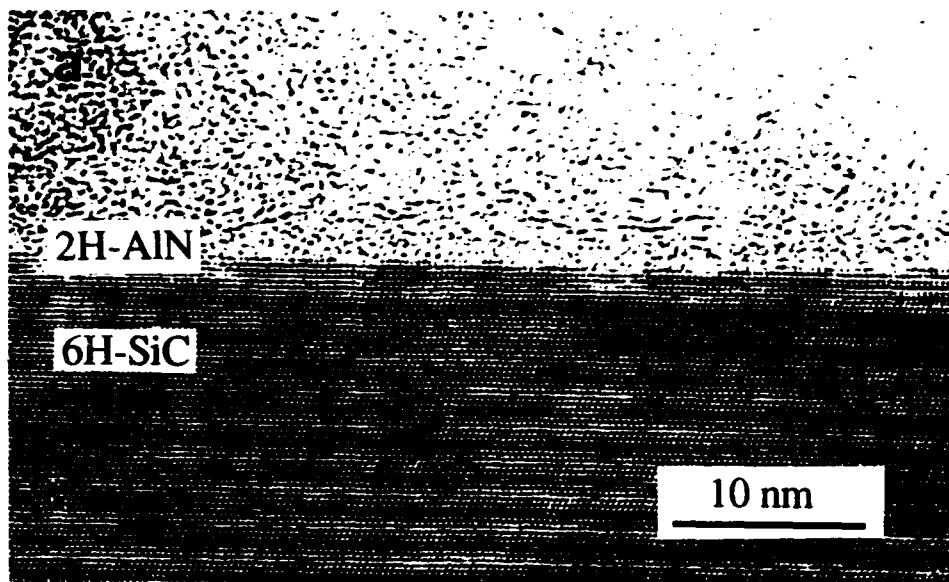


Figure 1. Cross-sectional TEM images of AlN films grown on (a) on-axis substrate and (b) vicinal substrate. The arrows shown in (b) indicate the step positions.

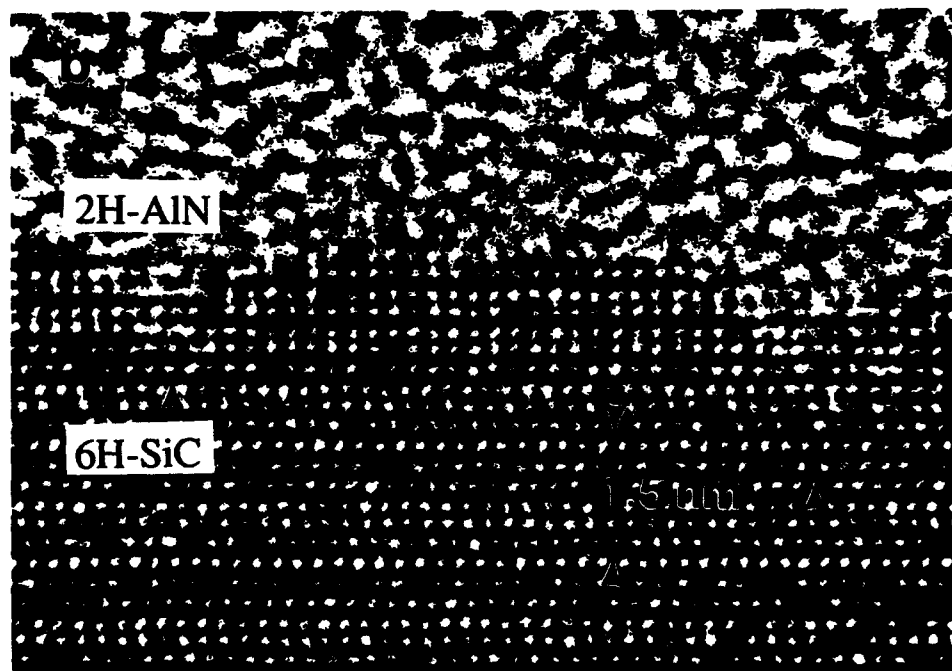
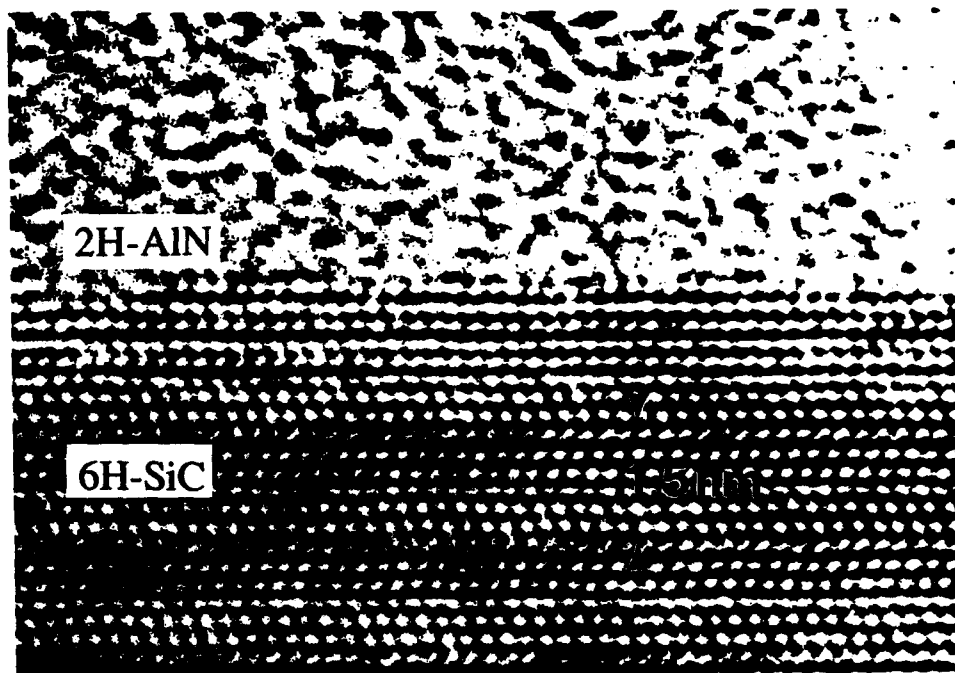


Figure 2. High resolution TEM images of AlN films and AlN/SiC interfaces of (a) on-axis substrate and (b) vicinal substrate. The arrows shown in (b) indicate the step positions.

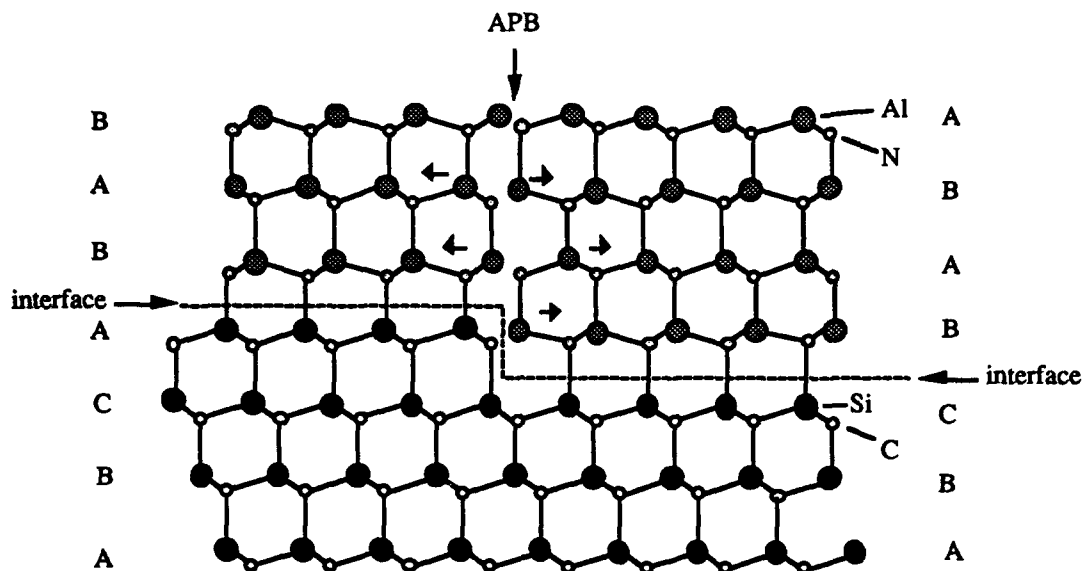


Figure 3. Model of the APB of the AlN/SiC interface. The short arrows indicate the direction of lattice distortion.

energetically prefers to occupy the wurtzite position on the SiC surface, i.e. Al atoms sit on the positions above the C atoms to bond with N atoms. Careful observation of the AlN/SiC interface also suggested the plausibility of this assumption. However, a detailed structural study by quantum mechanical calculations such as shown in the system of Si-NiSi₂ and Si-CoSi₂ [12] should be made to ascertain this assumption. As indicated by the arrows in Fig. 3, the lattice can be elastically relaxed. Adatoms may feel the strained potential at a step site so that they are hindered to migrate across the surface. Therefore, there is thickness variation which introduces an island formation on the terrace site. Nuclei on the different terrace sites fail to align with the neighboring nuclei (island) due to their anti-phase characteristics. Further study of the step configuration, however, indicates that nuclei formed on different levels of terraces can sometimes align with each other without any strain because of the step geometry of the 6H-SiC substrate [13]. It is clear that an idealistic on-axis SiC surface which includes no steps can provide nearly perfect AlN film growth at the initial stage of growth. A critical thickness for the Stranski-Krastanov growth mode, which might be applied in this AlN/SiC system, will be studied in the series of this research.

D. Conclusion

In summary, the initial stage of 2H-AlN film growth on both on-axis and vicinal 6H-SiC (0001) substrates was investigated by cross-sectional HRTEM. Comparison of very thin films (~15Å) grown on two different surfaces (on-axis and vicinal) shows different surface morphologies and interface micro-structures. A very smooth and defect free AlN film was formed on the on-axis substrate, indicative of a two-dimensional growth mode at this

thickness range. On the other hand, rough and defective features were observed in the AlN film on the vicinal substrate. The high resolution images and the structural model at the interface indicates the presence of APBs due to the nature of steps residing in the 6H-SiC substrate. Finally, it has been suggested that AlN film quality should be improved with the use of an on-axis substrate.

E. Future Plans

The investigation on AlN film growth on 6H-SiC substrates will be continued in terms of suppression of defects and growth mechanisms. The further growth of AlN films will be discussed. The results obtained in this study will be applied for the growth of other systems such as GaN/AlN/SiC and SiC/AlN/SiC. Thus, a similar investigation should be made for SiC growth on AlN surfaces to complete pseudomorphic heterostructural studies.

F. References

1. W. M. Yim, E. J. Stofko, P. I. Pankove, M. Ettenberg, and S. L. Gilbert, *J. Appl. Phys.* **44**, 292 (1973).
2. M. G. Norton, B. C. H. Steele, and C. A. Leach, *Science Ceram.* **14**, 545 (1988).
3. G. A. Slack, *J. Phys. Chem. Solids* **34**, 321 (1973).
4. Z. Sitar, M. J. Paisley, B. Yan, J. Ruan, W. J. Choyke, and R. F. Davis, *J. Vac. Sci. Technol.* **B8**, 316 (1990).
5. L. B. Rowland, R. S. Kern, S. Tanaka, and R. F. Davis, *Appl. Phys. Lett.* **62**, 3333 (1993).
6. J. H. Edgar, *J. Mater. Res.* **7**, 235 (1992).
7. S. Strite and H. Morkoc, *J. Vac. Sci. Technol.* **B10**, 1237 (1992).
8. H. Amano, M. Kito, K. Hiramatsu, and I. Akasaki, *Jpn. J. Appl. Phys.* **28**, L2112 (1989).
9. Cree Research Inc., Durham, NC.
10. L. B. Rowland, R. S. Kern, S. Tanaka, and R. F. Davis, *J. Mater. Res.* **8**, 2310 (1993).
11. C. H. Carter, Jr., R. F. Davis, and S. R. Nutt, *J. Mater. Res.* **1**, 811 (1986).
12. D. R. Hamann, *Phys. Rev. Lett.* **60**, 313 (1988).
13. S. Tanaka, R. S. Kern, and R. F. Davis, paper in progress.

XII. Properties of the Heteroepitaxial AlN/SiC Interface

A. Introduction

The semiconductor industry is presently limited in device application by the materials used in device fabrication. Novel materials are being sought to replace Si- and Ge-based devices. Devices are needed which operate at higher temperatures, powers, and frequencies than before. Radiation hardness is also a valued trait. Potential materials are diamond, SiC, AlN, and GaN. These wide bandgap semiconductors have the properties needed to realize these goals. Of these materials, SiC appears most advantageous [1]. This material can be readily grown and working devices have been made of SiC [2].

The material studied was an aluminum nitride (AlN) film grown epitaxially on a 6H silicon carbide (SiC) substrate. AlN has a direct optical band gap of 6.2 eV and a wurtzite hexagonal structure with an a-axis lattice constant of 3.11 Å. The growth was achieved by molecular beam epitaxy (MBE). The epitaxial growth is confirmed by RHEED measurements [3]. SiC can be used as a substrate for the growth of AlN due to the close lattice match (3.08 Å vs. 3.11 Å). This allows for the manufacturing of novel structures such as Negative Electron Affinity (NEA) surfaces for UV and X-ray detectors and cold cathode emitters. The possibility for NEA based vacuum collector-emitters also exists [4]. The phenomenon of a negative electron affinity (NEA) occurs at a semiconductor surface when the vacuum energy level lies below the conduction band edge. Since the bonding of common semiconductors are based on sp^3 hybridization, the valance band develops from bonding levels and the conduction band from the antibonding atomic orbitals. Since wide band gap semiconductors have common bonding origin, the NEA phenomenon is more likely to occur for these materials. The consequence of a NEA surface is that any electrons from the valence band promoted into the conduction band can escape from the material. Thus, having an NEA surface enhances cathode operation (emission).

B. Experimental Procedure

The presence of a NEA can be determined by ultraviolet photoemission spectroscopy (UPS) [5-7]. This technique involves directing 21.2 eV light (the He I resonance line) to the surface of the sample and detecting the spectrum of the emitted photo excited electrons as a function of electron kinetic energy. Typically, UPS is used to obtain a profile of the valence band (VB) electronic states. As such, most studies of UPS of semiconductors present data of the most energetic electrons emitted from the surface. Electrons scattered to lower energy and secondary electrons will be displayed in the spectra at lower kinetic energies. In addition, for a semiconductor which exhibits a NEA surface, a distinctive peak may be observed at the low kinetic energy (highest binding energy) end of the photoemission spectra. Fig. 1 depicts a

schematic representation of the photoemission spectra from a semiconductor with a negative or positive electron affinity. The low kinetic energy feature is due to secondary electrons which (quasi) thermalize to the conduction band minimum.

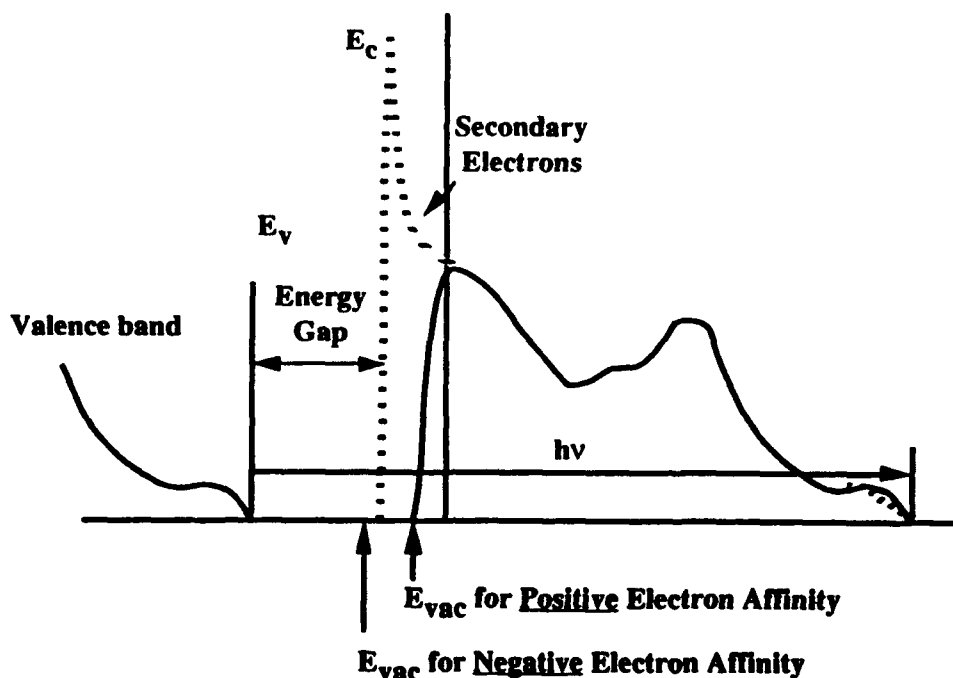


Figure 1. A schematic of the difference in the photoemission spectra of a semiconductor with a positive or negative electron affinity.

The sharp features typical of a NEA have been observed from spectra of (111) and (100) diamond surfaces [5-9]. In the studies of diamond, a correlation was made between the presence of hydrogen and the NEA peak [6,7]. In addition, it was also shown that thin metal layers such as Ti or other low workfunction metals could induce a NEA on the diamond surface [9,10]. These measurements verify that the surface dipole can be influenced by surface processing and that the effects contribute to the observation of a NEA.

For the AlN UPS studies presented here, the SiC substrate is important for two reasons. The first is that from wide bandgap semiconductors there would be charging problems, and the photoemission would be quickly quenched. The reason for this is that, with such a large band gap, the AlN acts as an insulator and will charge up. This problem is avoided by growing a thin layer of AlN on a conducting doped SiC substrate. The n-type SiC substrates used in this study, being more conductive than bulk AlN, provide a source of electrons for photoemission. The second benefit of the SiC substrate is the small lattice mismatch between SiC and AlN (3.08 Å vs. 3.11 Å). The small lattice mismatch enables heteroepitaxial growth.

The AlN/SiC sample was deposited on the SiC substrate by a modified gas source MBE system. The substrate was a vicinal wafer of 6H polytype (0001) (oriented 3-4 degrees towards [1120]) SiC which resulted in the growth of hexagonal (2H) AlN. The MBE system consists of three parts: a load lock (base pressure of 5×10^{-8} Torr), a transfer tube (base pressure of 1×10^{-10} Torr), which also was used for degassing the substrates, and the growth chamber (base pressure of 5×10^{-11} Torr). Knudson effusion cells with BN crucibles and Ta wire heaters were charged with 6N pure aluminum. Ultra-high purity nitrogen, further purified by a chemical purifier, was used as the source gas. The nitrogen gas was excited by an ECR plasma source, which was designed to fit inside the 2.25 inch diameter tube of the source flange cryoshroud. The details of the system can be found elsewhere. [11]

The SiC substrates were obtained from Cree Research Inc. Prior to loading into the chamber, the substrates were cleaned by a standard degreasing and RCA cleaning procedure. After undergoing a degassing procedure in UHV (700 °C for 30 minutes), the substrates were transferred into the deposition chamber. Epitaxial AlN films were deposited under the conditions shown below in Table I. The films examined were roughly 100 Å thick.

Table I. Deposition Conditions for MBE AlN Film Growth

Nitrogen pressure:	2×10^{-4} Torr
Microwave power:	50W
Aluminum cell temp:	1120 °C
Substrate temperature:	1100 °C
Deposition Rate:	1000 Å/hr

The samples were transported in air to the surface analysis system. The analysis system is made up of several chambers linked by a linear UHV transfer line. The details of the system are described elsewhere [8,10]. Among the capabilities available are UPS, XPS, LEED, hydrogen and argon plasma cleaning, thermal programmed desorption, and Auger Spectroscopy.

The UPS chamber has a base pressure of 2×10^{-10} Torr. Operating conditions involve pressures up to 1×10^{-9} Torr, but the higher pressure is due to the helium inflow and does not contaminate the sample. The UPS system utilizes a helium resonance lamp (the He I line) to provide a source of 21.2 eV light. Photoemitted electrons are measured with a 50 mm mean radius hemispherical electron analyzer operated at a 0.15 eV energy resolution and a

2° angular resolution. The analyzer (VSW HA50) is mounted on a double goniometer and can be tilted with respect to the sample in two independent directions. The AlN/SiC samples were fastened with tantalum wire to a molybdenum sample holder. The sample holder is biased by up to 4 V to allow low energy electrons to overcome the work function of the analyzer. The Fermi level of the system (sample and analyzer) is determined by UPS measurement of the sample holder with no sample bias (i.e., grounded). The sample holder can be heated to 1150 °C.

C. Results and Discussion

The UPS measurements were carried out on the AlN/SiC sample as loaded, and after anneals of 700 °C and 1000 °C. Auger Electron Spectroscopy (AES) and Low Energy Electron Diffraction (LEED) were also performed on the sample as-loaded, and after the anneals. The UPS data for the as-loaded AlN/SiC sample are displayed in Fig. 2. The spectra were obtained with different sample bias to overcome the workfunction of the analyzer. In the figure, all spectra have been displaced by the applied bias so that the Fermi level aligns. Two aspects indicate the presence of the NEA. The first is the detection of a low energy peak clearly observable with a sample bias of 3.0 Volts, with onset occurring at a bias of 1.5 Volts. The two low energy peaks of roughly the same height present at the 3.0 Volt bias are attributed to the normal secondary emission typical of UPS while the low energy feature is

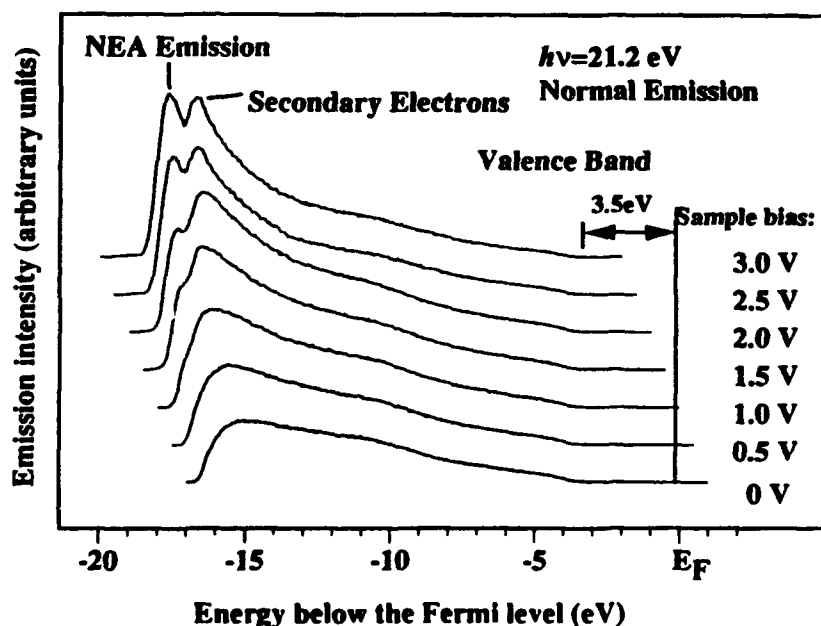


Figure 2. The uv-photoemission of AlN on 6H-SiC. The spectra were obtained at different sample bias to overcome the workfunction of the electron analyzer.

attributed to electrons thermalized to the conduction band minimum. This second peak is considered as the NEA peak since the electron count drops off so quickly. The large (~3V) bias is needed because the workfunction of the AlN is apparently less than that of the analyzer. The analyzer workfunction is between 4 and 5 eV.

The second indication of the NEA is that the widths of the photoemission spectra are consistent with the model described in Fig. 1. Here the width $W = h\nu - E_g$ where W extends from the low energy limit to the valence band maximum. We have used this relation to determine the position of the valence band maximum in the spectrum obtained with a 3V bias. The low energy limit was determined by linear extrapolation of the back edge to zero intensity. Then using the band gap of AlN as 6.2 eV and the 21.2 eV photon energy, the valence band maximum should then occur at 15.0 eV above this limit. The vertical line labeled Valence Band was obtained in this way. As is evident from the spectra, the valence band emission extends to this energy. We also note that the results indirectly verify that the band gap of the AlN film is the same as the bulk value of 6.2 eV. As mentioned earlier, the Fermi level is determined from the onset of electron emission from a metal sample.

The effect of annealing in vacuum was explored. After annealing to 700 and 1000 °C the photoemission spectra showed a decrease in the relative intensity of the NEA related peak (Fig. 3). Auger Electron Spectroscopy (AES) of the as-loaded surface showed oxygen and carbon contaminants in addition to the Al and N signals. After an anneal of 700 °C the AES showed a small reduction of the oxygen and a similar scale increase in the surface carbon, a trend that continued with the 1000 °C anneal. A LEED pattern was not visible from the sample as loaded or after the anneals of 700 °C and 1000 °C. We note that after a short H-plasma clean a faint 1×1 pattern was visible with an electron beam energy of 80 eV and the C signal was removed. The lack of a LEED pattern for the as-loaded and the annealed samples is possibly related to the carbon and oxygen on the surface. The reduction of the NEA related features indicates that the effect is related to the surface structure and termination of the AlN.

The second sample investigated was capped with a thin (<10Å) layer of silicon to prevent oxidation during transit. While the processing parameters were similar [14], the photoemission spectra were different as can be seen in Fig. 4. A peak sharper than that of the NEA surface in Fig. 2 appeared with a bias of 3.0 Volts, but the width of the spectra was not consistent with the known band gap. As such, we do not believe this to be a NEA surface. We attribute this to the presence of the silicon. Even after two plasma exposures, one of which was a deep etching exposure, we were unable to remove all of the silicon.

In comparison to the UPS spectra obtained from diamond surfaces which exhibit a NEA, [3-8] the feature in diamond is significantly sharper than that observed here for the AlN. There are several possible causes that could contribute to a broader signature. These could be

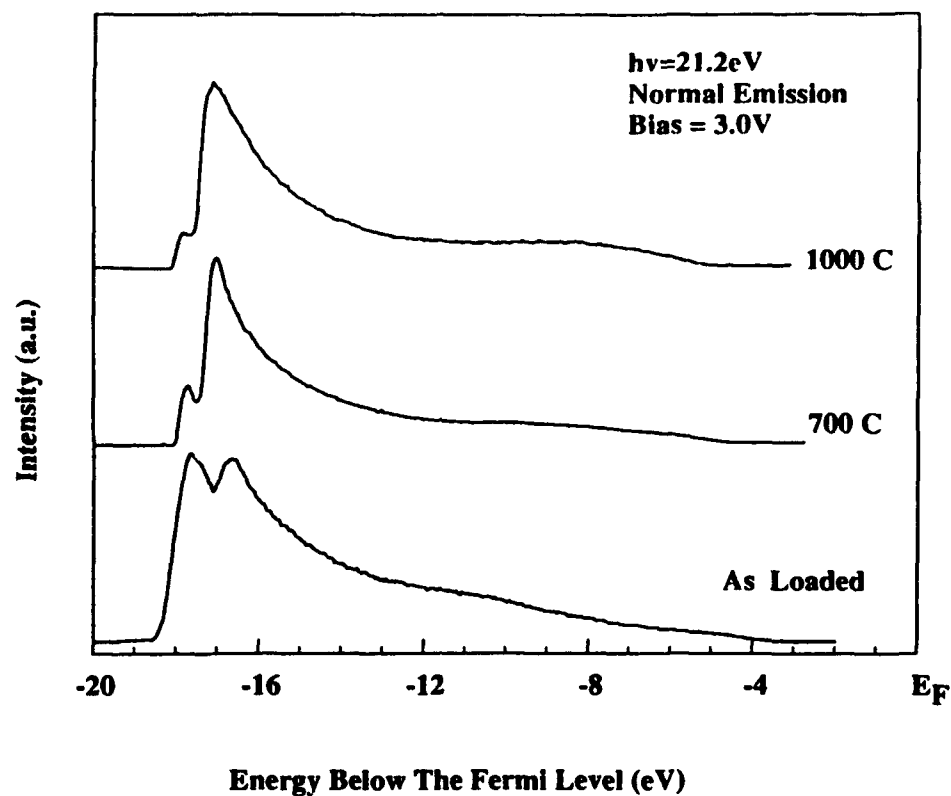


Figure 3. The uv-photoemission spectra of AlN on 6H-SiC as-loaded and after vacuum annealing at the indicated temperatures. All spectra were obtained with a sample bias of 3.0 kV.

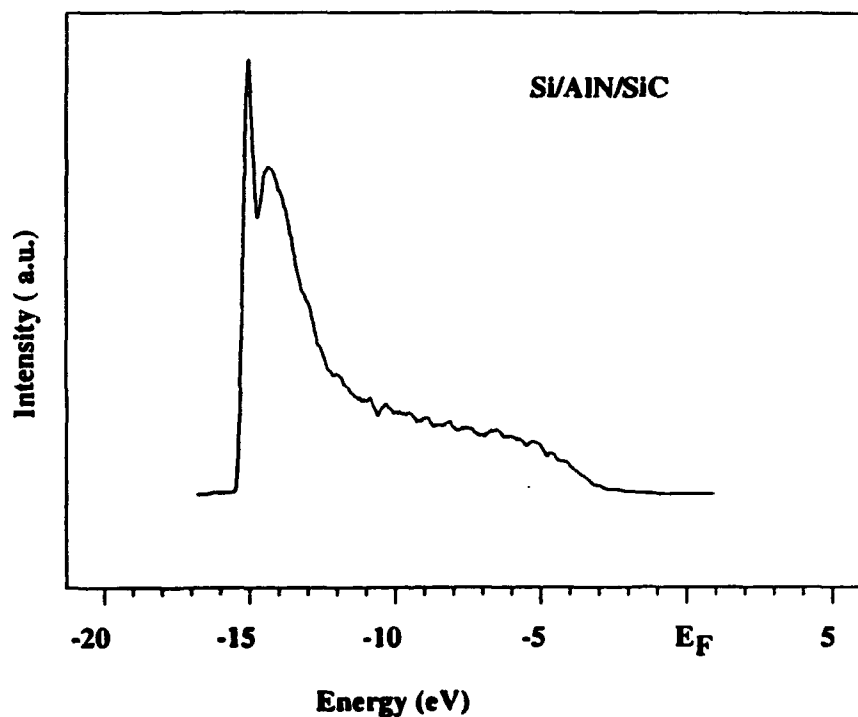


Figure 4. The uv-photoemission spectra of the second AlN on 6H-SiC sample studied. This spectrum was obtained with a sample bias of 3.0 kV.

related to a more disordered surface or to the intrinsic properties of the AlN (e.g., direct bandgap). Future research will explore these issues.

The last point that we address in this report is the position of the Fermi level in the AlN. From Fig. 1, it is evident that the surface Fermi level occurs at ~ 3.5 eV above the valence band maximum. This is near the center of the 6.2 eV bandgap. From this data we suggest a possible band alignment of AlN and SiC. Here we have assumed that there is no band bending in the AlN or in the SiC near the interface. Because of the wide band gap of the AlN, it seems unlikely that there is significant band bending in the thin film. The bulk Fermi level of the SiC has been determined from the doping level of the substrates to be ~ 0.3 eV below the SiC conduction band edge[12]. The results are summarized in Fig. 5. The band offsets are -0.8 eV at the valence band and 2.4 eV at the conduction band. The largest uncertainty in this proposed band offset is probably in the band bending in the SiC. Such band bending would result in an increase in the magnitude of the valence band offset and a decrease in the conduction band offset. While we are not aware of any calculations of the heterojunction band offsets of wurtzite AlN on 6H-SiC, there has been a calculation of the offsets of the (110) interfaces of cubic AlN/SiC [13]. The theoretical results also indicate a type I offset with band discontinuities of 1.5 eV at the valence band and -1.2 eV at the conduction band. This is qualitatively similar to the results presented in Fig. 5.

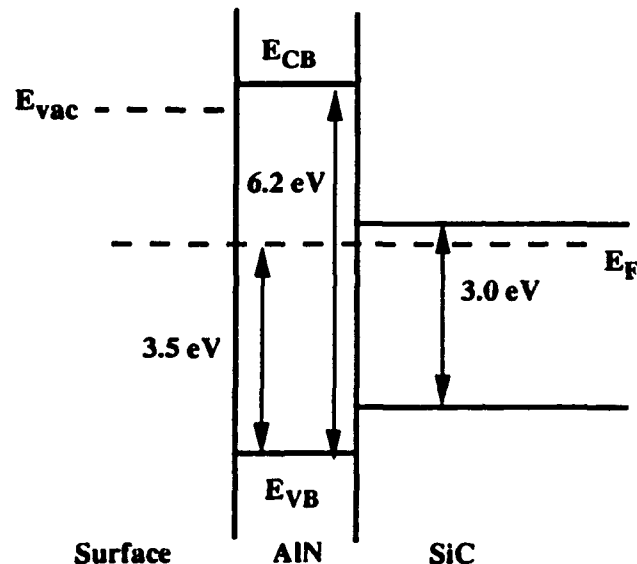


Figure 5. A schematic of the possible band alignment of AlN on 6H-SiC. The text describes the assumptions and related measurements.

D. Conclusions

In summary, we have observed features in the UPS spectra indicative of a NEA surface on as-loaded and annealed AlN on SiC. The measurements were made possible by the development of MBE heteroepitaxial growth of AlN on 6H-SiC. The NEA features are dependent on surface processing. The surface Fermi level of the AlN is found to be ~ 3.5 eV above the valence band maximum, and we have suggested a model for the band offsets assuming no band bending.

E. Future Plans

The preparation of the AlN films will be studied to determine the effect on the observed NEA. The aim will be to understand what parameter in the process has the greatest effect on the electron affinity. We will seek to understand if the observed behavior is latent or due to a surface contaminant lowering the workfunction. Films of various thicknesses will be studied.

F. References

1. J. H. Edgar, *J. Mater. Res.*, **7**, 235 (1992)
2. H. S. Kong, J. W. Palmour, J. T. Glass, and R. F. Davis, *Appl. Phys. Lett.* **51**, 442 (1987)
3. C. Wang, R. F. Davis, *Appl. Phys. Lett.* **63**, 990 (1993).
4. M. D. Williams, M. D. Feuer, S. C. Shunk, N. J. Sauer, and T. Y. Chang, *J. Appl. Phys.* **71**, 3042 (1992).
5. F. J. Himpsel, J. A. Knapp, J. A. van Vechten and D. E. Eastman, *Phys. Rev. B* **20**, 624 (1979).
6. B. B. Pate, *Surf. Sci.* **165**, 83 (1986).
7. B. B. Pate, M. H. Hecht, C. Binns, I. Lindau and W. E. Spicer, *J. Vac. Sci. Technol.* **21**, 364 (1982).
8. J. van der Weide and R. J. Nemanich, *J. Vac. Sci. Technol. B* **10**, 1940 (1992).
9. J. van der Weide and R. J. Nemanich, *Appl. Phys. Lett.* **62**, 1878 (1993).
10. J. van der Weide and R. J. Nemanich, *Phys. Rev. B* **49**, 13629 (1994).
11. Z. Sitar, M. J. Paisley, D. K. Smith and R. F. Davis, *Rev. Sci. Instrum.* **61**, 2407 (1990).
12. J. Pelletier, D. Gervais, and C. Pomot, *J. Appl. Phys.* **55**, 994 (1983)
13. W. R. L. Lambrecht and B. Segall, *Phys. Rev. B* **43**, 7070 (1991).
14. L. B. Rowland, R. S. Kern, S. Tanaka, and R. F. Davis, in *Proceedings of the Fourth International Conference on Amorphous and Crystalline Silicon Carbide*, edited by C. Y. Yang, M. M. Rahman, and G. L. Harris (Springer, Berlin, 1992) p. 84.

XIII. Application of Epitaxial Aluminum Nitride (AlN) in Metal-Insulator-Semiconductor Structures

A. Introduction

The large band-gap (6.2eV) and good thermal stability (0.05 Torr equilibrium vapor pressure of nitrogen at 1500°C) indicate that AlN films have considerable potential as a dielectric in electronic devices. There are several published papers [1-4] which describe the investigations and the applications of AlN films as insulators in several MIS structures containing Si and GaAs. However, in all these studies the AlN films were polycrystalline.

We have shown in previous reports that AlN films with low defect densities can be epitaxially deposited on SiC substrates by the use of a modified gas source MBE system [5]. In this paper, we have investigated the application of epitaxial AlN films as insulators in SiC MIS structures. The electrical properties of the AlN insulator layers have been studied using current voltage (I-V) and high-frequency capacitance-voltage (hf C-V) measurements.

B. Experimental Procedure

The MIS structure was fabricated using a commercial Perkin-Elmer 430 MBE system. This system consists of three parts: a load lock (base pressure of 5×10^{-8} Torr), a transfer tube (base pressure of 1×10^{-10} Torr), which also was used for degassing the substrates, and the growth chamber (base pressure of 5×10^{-11} Torr). A Knudsen effusion cell with a BN crucible and a Ta wire heater was charged with 6N pure aluminum. Ultra-high purity nitrogen, further purified by a chemical purifier, was used as the source gas. The nitrogen was excited by an ECR plasma source, which was designed to fit inside the 2.25 inch diameter tube of the source flange cryoshroud.

The substrates were n-type ($n = 6.4 \times 10^{16} \text{ cm}^{-3}$), vicinal $\alpha(6H)\text{-SiC}(0001)$ wafers oriented $3\text{-}4^\circ$ towards [1120] and supplied by Cree Research Inc. An ohmic Ni contact was deposited on the backside. Prior to deposition, the substrates were cleaned by a standard degreasing procedure, chemically cleaned in a 10% HF solution for five minutes, mounted on a 3-inch molybdenum block, loaded into the system, heated to 700°C for 30 minutes in the transfer tube under UHV conditions to remove surface hydrocarbons and transferred into the deposition chamber.

A 125 Å thick of epitaxial AlN was deposited on the $\alpha\text{-SiC}$ wafer at 1100°C, followed by *in situ* deposition of Al-metal layer at room temperature. The details of the epitaxial deposition conditions of AlN film can be found in Ref. [5]. To form MIS diodes, the top Al-layer was patterned by standard lithographic etching techniques as circular dots of radius 50 μm and annealed at 400°C for half hour in the vacuum. The schematic diagram of the MIS structure was shown in Fig. 1.

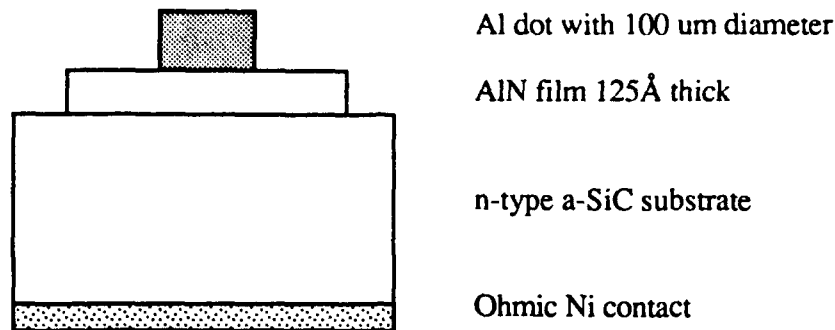


Figure 1. Schematic diagram of AlN MIS diode.

Direct I-V and hf C-V characteristics of the MIS structures at different temperature were characterized using a Hewlett Packard 4145 Semiconductor Parameter Analyzer and a Keithley M590CV Analyzer, respectively.

C. Experimental Results

The experimental I-V curves of the MIS structure at two different temperatures are shown in Fig. 2. Rectifying behavior was observed. The forward bias current increased with an increase of the forward bias voltage. The breakdown field of the AlN MIS structure was ≈ 13.4 MV/cm at room temperature; the value was slightly smaller, 13 MV/cm, at 300°C. The reverse bias currents are very small for both temperatures and no breakdown occurred even for the field larger than 70 MV/cm.

The results of hf C-V measurements of the MIS diode are shown in Fig. 3. These measurements were made using a 100 kHz AC signal. Figure 3 indicates that the diode could be swept from accumulation to inversion. Hysteresis in the C-V trace was observed when the voltage ramp direction was reversed. The diode also exhibited a positive flat band voltage. From the film thickness and accumulation capacitance data, the dielectric constant of AlN insulator layer at 100kHz was estimated as ~ 14 , which is higher than what has been reported [3,6].

D. Discussion

The recent advances of III-V nitride film quality have resulted in the successful fabrication of a variety of III-V nitride based devices [7-9]. It is expected that it will become important to study and develop the proper insulating material for III-V nitride devices. For many years, the potential of using AlN as dielectric insulator due to its large band gap and good thermal stability has been realized. There were several reported investigations of the use of AlN as an insulator in MIS structures. However most of the work conducted to date has

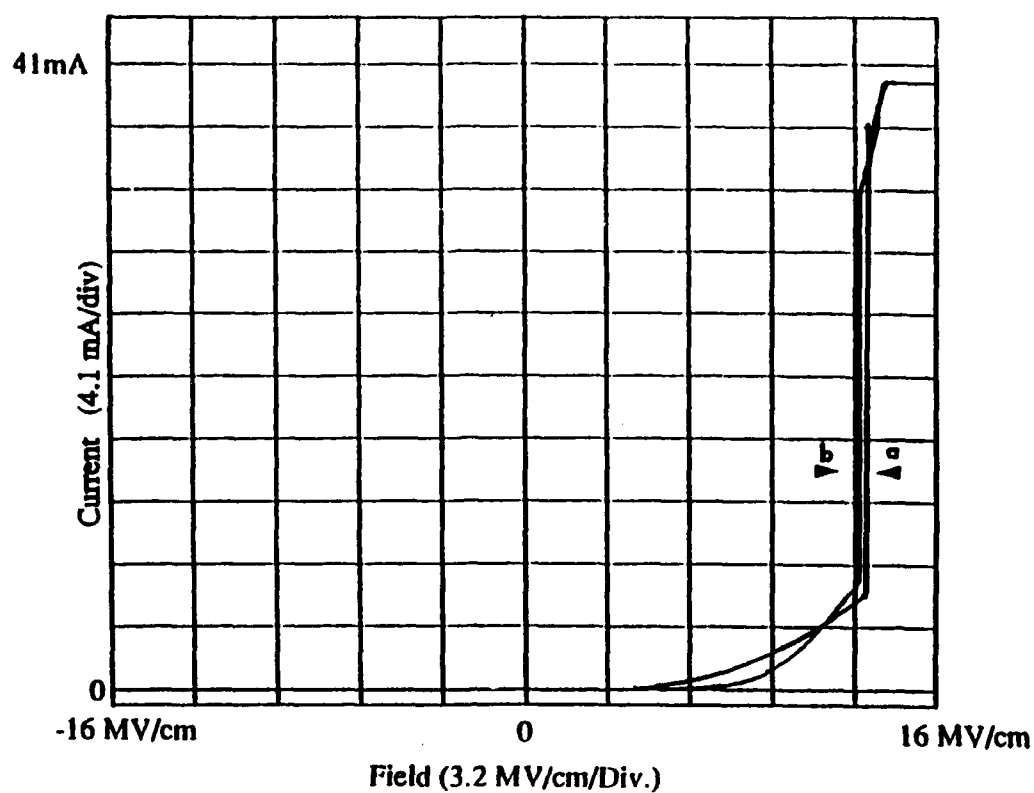


Figure 2. I-V curve for AlN MIS diode measured at (a) room temperature; (b) 300°C.

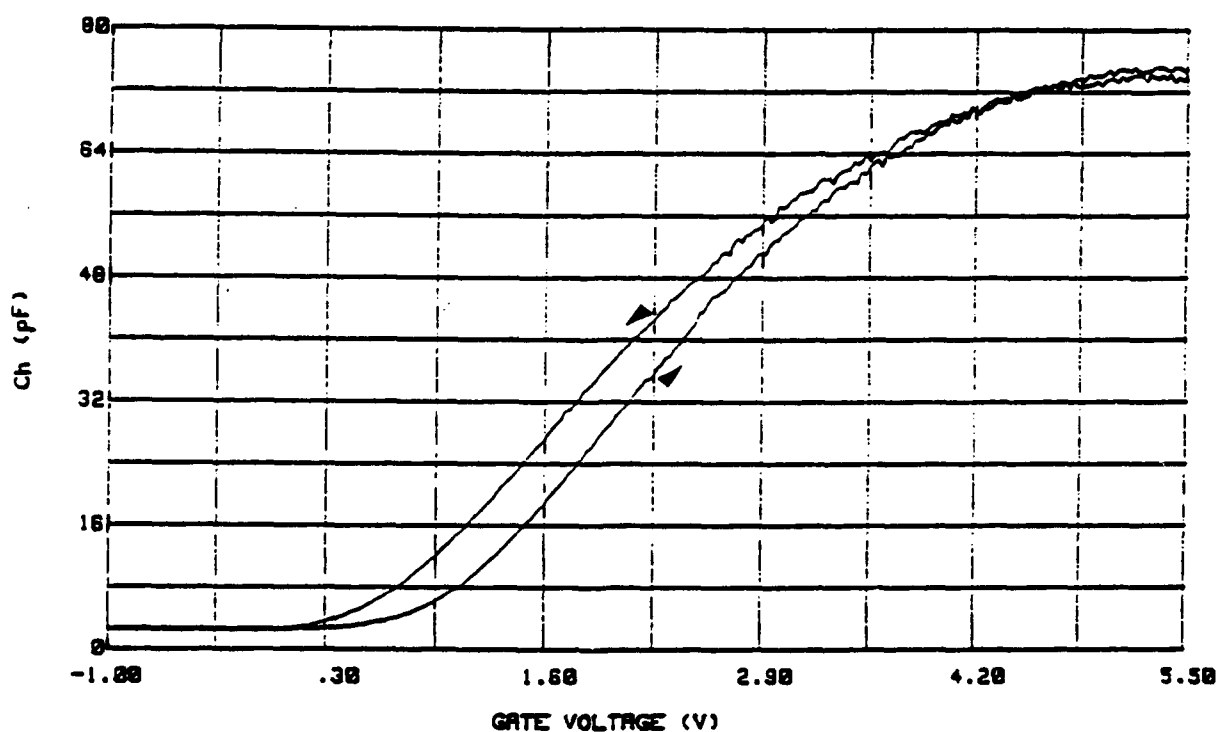


Figure 3. C-V curve of AlN MIS diode measured at 100 kHz of frequency.

been on Si or GaAs substrates, and the AlN film films were polycrystalline. We are for the first time reporting the use of monocrystalline epitaxial AlN films as the insulator in a SiC MIS structure. The dielectric properties of AlN have been studied and the AlN MIS structure has been demonstrated to be operative at high temperature (300°C). The significance of this work is that the application of epitaxial AlN as an insulator can simplify the III-V device process. However, this study is preliminary. More detailed investigations are needed to fully understand the dielectric properties of the AlN films, including the determination of the interface state densities and reducing the methods for the leakage currents before they can be successfully used in device structures.

As we have shown above, the AlN MIS structure exhibited both rectification behavior and unwanted leakage currents. These phenomena may be explained using the band diagram in Fig. 4. Under reverse bias, the SiC semiconductor substrate is in the depletion mode, therefore, the majority of the applied voltage is dropped across the depletion region, as shown in Fig. 4(b). Under forward bias, the semiconductor region is in an accumulation state; therefore, a large part of the voltage is across the barrier, which causes severe band bending at the interface, as shown in Fig. 4(c). This band bending reduces the effective barrier height and increases the probability of tunneling through the thin barrier region. Both of these factors lead to a large leakage currents. It is expected that by increasing the AlN thickness, and using the metals with higher work function, the probability of band bending and tunneling would be suppressed and the leakage current reduced.

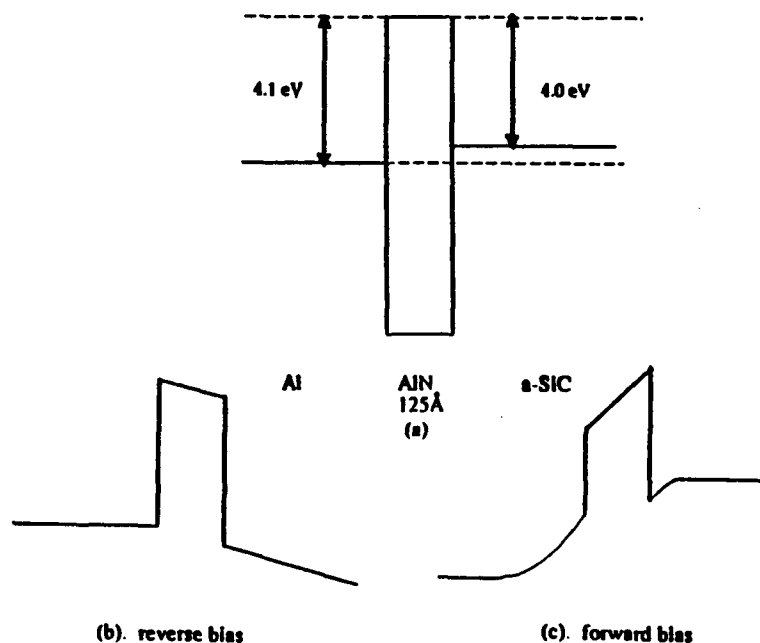


Figure 4. Band diagram of AlN MIS structure under the bias conditions: (a) no bias; (b) reverse bias; (c) forward bias.

E. Summary

A preliminary investigation of the use of monocrystalline epitaxial AlN in an SiC MIS structure has been conducted. The breakdown field of AlN was estimated to be 13.4 MV/cm at room temperature. At 300°C, the breakdown decreased slightly to 13 MV/cm. Capacitance-voltage characteristics showed that the diode could be swept from accumulation to inversion. The dielectric constant has been estimated as ~14.

F. References

1. S. Mirsch and H. Reimer, Phys. Stat. Sol. 11, 631 (1972).
2. E. A. Irene and V. J. Silvestri, J. of Electronic Materials Vol.4, 409 (1975).
3. T. L. Chu and R. W. Kelm, J. Electrochem. Soc. 122, 995 (1975).
4. Y. Mochizuki, M. Mizuta, S. Fujieda and Y. Matsumoto, J. Appl. Phys. 67, 2466 (1990).
5. C. Wang, K. S. Ailey, K. L. More and R.F. Davis, in press (1993).
6. A. T. Collins, E. C. Lightowers and P. J. Dean, Phys. Rev. 158, 833 (1967).
7. R. F. Davis, Proc. IEEE 79, 702 (1991).
8. A. M. Khan, J. K. Kuzina and R. T. Olson, Appl. Phys. Lett. 62, 1786 (1993).
9. S. Strite and H. Morkoc, J. Vac. Sci. Technol. B10, 1237 (1992).

XIV. Application of Epitaxial AlN Films in Surface Acoustic Wave Devices

A. Introduction

The surface acoustic wave (SAW) device applies the SAW bound to the surfaces of piezoelectric materials in electronic devices and is important for various information and communication systems. This is especially true for the high frequency band SAW devices operated in the GHz range due to the increasing volume of information and communication media. Many materials have been studied to make this SAW device and AlN, compared to other conventional materials, is more suitable to this GHz band SAW device due to its high surface wave velocity. Interdigital Transducer (IDT) made of AlN films can be fabricated in the GHz range by using conventional photolithography techniques.

The advantages of applying AlN in SAW devices has long been known, such as very high wave velocity, high electrical resistivity, chemical and thermal stability, as well as the compatibility with semiconductor processing technology [1]. However, the difficulty of producing the heteroepitaxial AlN films with good crystal quality hampered early progress. Now, with the availability of modern epitaxy thin film technology, the crystal quality of AlN films has been remarkably improved. Thus, the interest of applying AlN in SAW devices has once again emerged. In Japan, several research labs have already reported successful fabrication of AlN SAW devices with frequency operated in GHz range [2,3].

In this report, we will discuss initiation of the project of applying epitaxial AlN films in SAW devices. This is a coordinated effort between North Carolina State University and a French Institute. At North Carolina State, we have made epitaxial AlN films by a modified gas source MBE system and processed AlN SAW devices. The structures of SAW devices were designed and the characterization of these SAW devices will be carried out in France.

B. Experimental Procedure

The deposition system employed in this research was a commercial Perkin-Elmer 430 MBE system. This system consists of three parts: a load lock (base pressure of 5×10^{-8} Torr), a transfer tube (base pressure of 1×10^{-10} Torr), which also was used to degas the substrates, and the growth chamber (base pressure of 5×10^{-11} Torr). Knudson effusion cells with BN crucibles and Ta wire heaters were charged with 6N pure aluminum. Ultra-high purity nitrogen, further purified by a chemical purifier, was used as the sources gas. It was excited by an ECR plasma source which was designed to fit inside the 2.25" diameter tube of the source flange cryoshroud. The details of the system can be found elsewhere [4].

Prior to loading into the chamber, the substrates were chemically cleaned, then *ex-situ* cleaned substrates were mounted on a 3" molybdenum block and loaded into the system. After undergoing a degassing procedure (700°C for 30 minutes), the substrates were

transferred into the deposition chamber. Finally, RHEED was performed to examine crystalline quality of the substrates.

As previously reported, we have shown that by modified gas source MBE, the epitaxial AlN films with very good crystal quality can be deposited on $\alpha(6H)$ -SiC(0001) substrates at 1100°C [5]. High resolution TEM studies indicated there are fewer defects in this good crystal quality epitaxial AlN film. Also x-ray rocking curve (XRC) measurements showed that on a (0001) oriented $\alpha(6H)$ -SiC substrate with optimized surface, XRC HWFM of (0004) diffraction peak of AlN epilayer was reached at less than 44 arc seconds [6]. This is the best AlN film seen so far. It is expected that this type of AlN epitaxial film will have a superior performance in SAW devices. The details of AlN SAW device process are described below.

A $\sim 3000\text{\AA}$ thick of epitaxial AlN layer was deposited on SiC or sapphire substrates by modified GSMBE. Typical deposition conditions are listed in Table I. After AlN deposition, a layer of Al metal film, $\sim 3000\text{\AA}$, was *in-situ* deposited on the top of AlN at room temperature. This top Al-layer was masked and patterned by a standard photolithography technique to form Interdigital Transducer (IDT). The IDT Mask was designed and provided the French Institute. The AlN SAW devices have been sent to France and the characterization of these AlN SAW devices will be carried out there.

Table I. Deposition Conditions for AlN SAW Devices

Nitrogen pressure	2×10^{-4} Torr
Microwave power	50W
Aluminum cell temperature	1085°C
substrate temperature	1100°C
Al pre-layer	2 monatomic layer
AlN layer	3000 \AA
Top Al-layer	3000 \AA

C. Discussion and Future Research Plans

Concerning the materials for the Surface Acoustic Wave device application, there are two important parameters: 1) SAW velocity, v , and 2) the electromechanical coupling coefficient, K^2 , a measure of the efficiency of a given piezoelectric in converting an applied electrical signal into mechanical energy associated with a surface acoustic wave. Table II lists these properties for several different materials.

Table II. The SAW Properties of Materials

Material	Crystal Cut	Axis	SAW Velocity (m/s)	K2 (%)
quartz	ST	X	3158	0.11
LiNbO ₃	Y	Z	3488	4.5
LiNbO ₃	128°	X	3992	5.3
Bi ₂ GeO ₂₀	110	001	1681	1.4
LiTaO ₃	Y	Z	3230	0.72
GaAs	<001>	(100)	<2841	<0.06
ZnO/Al ₂ O ₃	0112	1120	5200	4
AlN/Al ₂ O ₃	0112	1120	6680	0.72

As seen in Table II, the SAW velocity of AlN film is much higher than others, which makes a GHz-range SAW device easily fabricated by using conventional photolithography IDT techniques. Also, the compatibility of AlN with semiconductor processing, as well as its unique properties, such as high electrical resistivity, chemical and thermal stability, can simplify the integrated signal processing system.

However, unlike other conventional materials, the piezoelectric properties of AlN have still not been fully studied and the controllability of film quality is far from mature yet. In order to make a practically useful AlN SAW device, there are many issues to be addressed and studied, which we will discuss in the following section.

Substrate Choice. For most materials applied in SAW devices, c-axis possess important piezoelectric coefficient, most SAW devices were made in such way that SAW propagates along c-axis, that is the substrate orientation needed to be chosen so that c-axis of the film lies in the plane of the epitaxial film. As there is no AlN substrate presently available, all AlN films were heteroepitaxially grown on sapphire substrates. Past research has revealed that the orientation of AlN rotated with respect to sapphire substrate due to the very large lattice mismatch between these two. It was found that on R-plane sapphire substrate, c-axis of epitaxial AlN will be in the plane of the film [1]. We have started to make AlN films on the SiC substrate and found that they have much better crystal quality than on sapphire due to smaller lattice mismatch. However, all the research work of AlN has been conducted only on (0001) SiC substrate, therefore, the challenge comes in making an AlN SAW device on (0001) SiC substrate. We have noticed that very recently a Japanese research group has demonstrated an AlN SAW device on (0001) sapphire substrate by just improving the surface morphology of AlN epilayer [7].

Recently, we obtained several SiC substrates with orientations of (1010) and (1120) from Cree Research Inc. We have also processed AlN SAW devices on these substrates, in which we expect the SAW will propagate along c-axis. As shown in Table III, the smallest average lattice constant mismatch, c/n, between AlN and SiC suggested that the AlN epilayer with better crystal quality may be achieved on these substrates. Characterization of these AlN SAW devices are ongoing in France. In the mean time, we are proposing to investigate:

- i) What orientation the AlN epilayer will have with respect to SiC substrate?
Will they parallel to each other, like what has been observed for AlN on (0001) SiC substrate? Therefore c-axis will be in the plane of the films.
Or will AlN rotate with respect to SiC substrate, like what has been observed for AlN on sapphire substrate?
- ii) If the orientation of AlN epilayer is parallel to the SiC substrate, how 2-H AlN align with 6-H type SiC?
- iii) What effect of orientation on the crystal qualities of AlN epilayer?

Table III. The Lattice Mismatch Between AlN Epilayer and SiC Substrate

in-plane direction	Repeat distance		Mismatch
	AlN	SiC	
[1000]/[1000]	3.11	3.07	1.2%
c-constant	4.98	15.08	67%
c/n	2.49	2.51	0.8%

Device Structure Consideration. SAW device is basically a IDT. For the device processing, we use a IDT mask designed by the French Institute. Here, the main concerns from our part are the determination of the thickness range of the films:

- i) AlN epilayer thickness: The epilayer film has to be thick enough to eliminate the acoustic interactions between the film and the substrate and permit a pure SAW to propagate in the film. Ideally, the piezoelectric film thickness should be 1~4 wavelength of SAW. Calculate from the typical wavelength of AlN SAW devices, a 1 μ m thick AlN epilayer is needed. However, there is no data for the piezoelectric properties of SiC, it is unknown so far what type acoustic interaction SiC will have.
- ii). Top Al-metal film: Normally, electrode films should be as thin as possible to reduce the electrical resistance. However, the resistance of the Al IDT electrodes is not significant since this will contribute to circuit-factor loading C(f) and insertion loss.
Typical Al thickness: 500~2000Å

Other Considerations. There are many factors from a materials processing point of view which have a severe effect on the device performance, we need to be aware of them:

- i) Porosity of the epilayer surface: causes an increase of wave guide propagation and insertion losses. Polishing of the epilayer film surface may help to reduce this effect;
- ii) A departure from parallel epitaxy: causes uncertainty in the alignment of transducer patterns for acoustic propagation along the c-axis of the film, it will diminish K2 value;
- iii) Thickness variation: causes the difficulties to tune the input or output power.

G. References

1. M.T. Duffy, *Heteroepitaxial Semiconductors for Electronic Devices*, ed. by G. W. Gullen and C. C. Wang, Springer-Verlag.
2. H. Okano, N. Tanaka, K. Shibata and S. Nakano, *Jpn. J. Appl. Phys.* **32**, 4052 (1993).
3. T. Shiosaki, Sixth US-Japan Seminar on Dielectric and Piezoelectric Ceramics (Lahaina, Hawaii, USA, November 11-12, 1993).
4. Z. Sitar, M. J. Paisley, D. K. Smith and R. F. Davis, "Design and Performance of an Electron Cyclotron Resonance Plasma Source for Standard Molecular Beam Epitaxy Equipment," *Rev. Sci. Instrum.* **61**, 2407 (1990).
5. C. Wang, K. S. Ailey, K. L. More and R. F. Davis, *Material in Electronics*, to be published (1994).
6. R. S. Kern, S. Tanaka and R. F. Davis, *Proceedings of the 3rd International Conference on High Temperature Semiconductors*, Charlotte, NC, 6/14/94.
7. H. Okano, N. Tanaka, Y. Takahasi, T. Tanaka, K. Shibata and S. Nakano, *Appl. Phys. Lett.* **64**, 167 (1994)

XV. Growth and Characterization of GaN Thin Films Grown by OMVPE

A. Introduction

The potential semiconductor and optoelectronic applications of the wide bandgap III-V nitrides has prompted significant research into their growth and development. GaN (wurtzite structure), the most studied in this group, has a bandgap of 3.4 eV and forms continuous solid solutions with both AlN (6.2 eV) and InN (1.9 eV). As such, materials with engineered bandgaps are envisioned for optoelectronic devices tunable from the visible to deep UV frequencies. An AlGaIn/InGaIn/AlGaIn double heterostructure-base blue LED is now commercially available in Japan. The relatively strong atomic bonding of these materials also points to their potential use in high-power and high-temperature devices.

Single crystal wafers of GaN do not exist [1]. Sapphire(0001) is the most commonly used substrate, although its lattice parameter and coefficient of thermal expansion are different than that of GaN. The use of low temperature (450°C-600°C) buffer layers of AlN [2-5] or GaN [6,7] has resulted in improved GaN film quality and surface morphology. Undoped GaN is n-type. To date, p-type behavior has been achieved in chemically vapor deposited Mg- or Zn-doped GaN using either low-energy electron beam irradiation [8] or via thermal annealing in a N₂ atmosphere [9]. Acceptor-type behavior has been obtained directly in molecular beam epitaxially grown films [10].

In the present research, monocrystalline GaN films have been grown directly on vicinal, n-type α (6H)-SiC(0001)_{Si} wafers via organometallic vapor phase epitaxy (OMVPE) in a cold-wall, vertical barrel reactor. GaN film growth on vicinal SiC(0001)_C wafers and sapphire(0001) was also investigated. Triethylgallium (TEG) and ammonia were used as the reactants. The heteroepitaxial growth of GaN on SiC was characterized using reflection high-energy electron diffraction (RHEED), scanning electron microscopy (SEM), transmission electron microscopy (TEM), photoluminescence spectroscopy (PL) and X-ray rocking curve (XRC) and Hall-effect measurements. The following sections describe the experimental procedures, detail the results, provide a discussion and conclusions regarding this research and outline future research plans and goals.

B. Experimental Procedure

GaN thin films were grown directly on off-axis SiC(0001) and sapphire(0001) substrates at 900°C. Low-temperature buffers layers were not employed in this study. The as-received vicinal SiC and sapphire wafers were cut into 7.1 mm squares. The SiC pieces were degreased, dipped into a 10% HF solution for 10 minutes to remove the thermally grown oxide layer and blown dry with N₂ before being loaded onto the barrel-style, SiC-coated graphite susceptor. For the sapphire substrates, prior to being HF dipped, they were cleaned

for 10 minutes in a hot $\text{H}_2\text{SO}_4\text{:H}_3\text{PO}_4$ solution. The reactor was evacuated to $<3 \times 10^{-5}$ torr for one hour prior to initiating growth. The continuously rotating susceptor was heated to 900°C by rf induction in 1.5 slm of flowing N_2 . Nitrogen was also used as the diluent and as the TEG carrier gas. The flow rates of TEG, NH_3 and N_2 diluent were $14.75 \mu\text{mol/min}$, 500 sccm and 1.5 slm, respectively. The system pressure during growth was 45 torr.

The structural, microstructural, optical and electrical characteristics of the epitaxial GaN thin films were analyzed using several techniques. SEM was performed on a JEOL 6400FE operating at 2 kV. The XRCs were obtained using a double-crystal X-ray diffractometer (Siemens D5000) with $\text{CuK}\alpha_1$ line (1.54094\AA) as the X-ray source. XRCs were recorded by plotting the diffracted intensity measured with a scintillation counter versus the specimen crystal rotation angle ω [11]. Conventional and high resolution TEM was performed on a JEOL 4000EX microscope operating at 400 kV. The photoemission properties of the unintentionally doped GaN films of varying thicknesses on vicinal $\text{SiC}(0001)_{\text{Si}}$ substrates were determined using low-temperature ($T = 20\text{K}$) PL obtained using a 15 mW He-Cd laser (325 nm) as the excitation source. GaN films grown on sapphire(0001) with no buffer layer were analyzed for comparative purposes. The unintentionally doped GaN films were characterized by Hall-effect measurements using the Van der Pauw geometry. Thermally evaporated Al was used as the contacts to these films with only linear regions of the current-voltage (I-V) curves being used for taking the Hall measurements.

C. Results and Discussion

A TEM micrograph of an $0.36 \mu\text{m}$ unintentionally doped GaN film on $\text{SiC}(0001)_{\text{Si}}$ is shown in Fig. 1. RHEED patterns for GaN grown on the $\text{SiC}(0001)_{\text{Si}}$ are displayed in Fig. 2.



Figure 1. TEM micrograph of GaN grown directly on $\text{SiC}(0001)_{\text{Si}}$ at 900°C by OMVPE.



Figure 2. RHEED patterns for GaN grown on SiC(0001)_{Si} at 900°C showing the (a) $[11\bar{2}0]$ and (b) $[10\bar{1}0]$ azimuths.

The former shows that the defect density diminishes as film thickness increases. The apparent vertical threading dislocations are believed to originate at the steps in the vicinal SiC surface as a result of the incompatibilities between the ABCACB... stacking sequence of (6H)-SiC and the ABABAB... sequence of (2H)-GaN. Any misalignment at these dislocations is very small, as the lattice images of the GaN bilayers traverse these threading dislocations without loss of contrast.

For the GaN films, XRC data revealed full width at half maximum (FWHM) values as low as 144 arcsec for the GaN(0002) reflection (Fig. 3). The sample from which Fig. 1 was obtained had a value of 148 arcsec for this reflection. In conjunction with the TEM images, these low FWHM values indicate that the film quality of GaN directly on SiC without a buffer layer is at least equal to that of GaN/buffer layer/sapphire(0001) films [12].

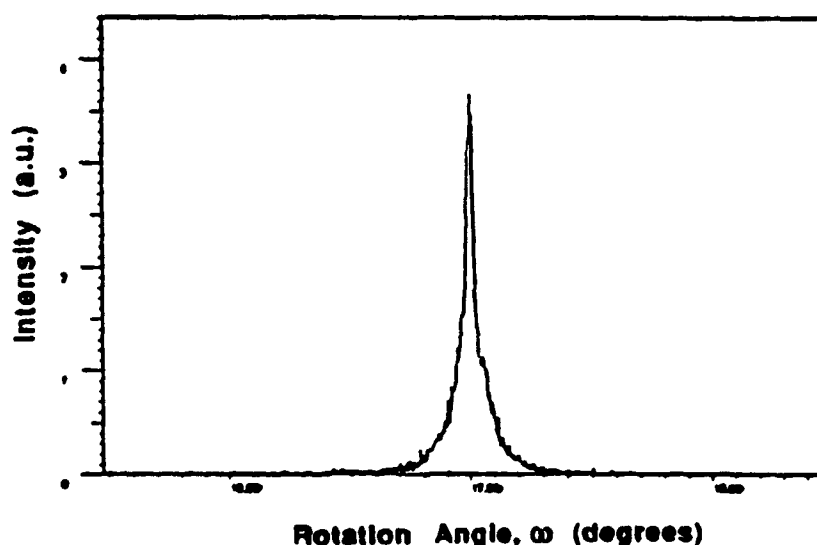


Figure 3. X-ray rocking curve for the GaN(0002) reflection. The FWHM value is 144 arcsec.

The low-temperature PL spectra of the various films are shown in Fig. 4. The lowest wavelength (highest energy) peaks are near-band-edge emissions. These quasi-I₂ lines centered around 357 nm for the thicker films [Fig. 4(D) and (F)] are attributed to the recombinations of excitons bound to neutral donors. The second group of peaks located at higher wavelengths are tentatively assigned to donor-acceptor (DA) transitions [13]. Figure 4 shows the PL peaks of GaN on SiC(0001)_{Si} tend to shift to higher wavelengths (lower energies) with decreasing GaN film thickness. The peak intensities have been scaled appropriately to better facilitate graphical representation. The observed peak shifts are attributed to residual strain in the GaN lattice on SiC at reduced film thicknesses [14]. As the GaN films become thicker, the quality of the volume of material analyzed by PL improves. Thus, the shift in the PL signals originating from the highly defected interfacial region of the GaN/SiC films are not observed in the thicker films. With the large lattice mismatch between GaN and sapphire, strain is relaxed immediately and does not distort the PL spectra as strongly. The residual stress in the GaN/SiC becomes relieved as film thickness increases. Only the thicker 1.2 μm GaN/SiC film [Fig. 4(D)] has PL peaks similar to the GaN/sapphire films [Figs. 4(E) and (F)].

GaN films grown on the different polar planes of SiC(0001), namely the Si- and C-faces, had dissimilar surface morphologies as can be seen in Figs. 5 and 6, respectively. Using X-ray photoelectron spectroscopy, Sasaki [15] determined that GaN polarity changes in

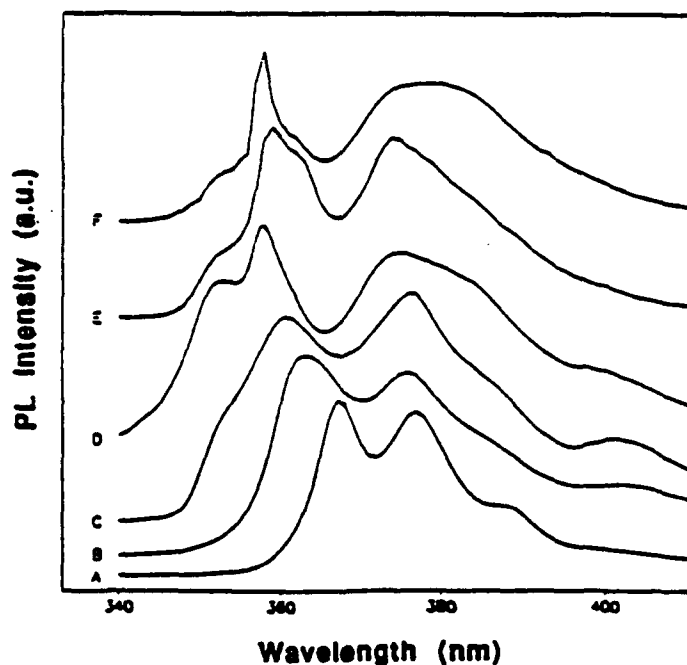


Figure 4. Low-temperature ($T = 20\text{K}$) PL spectra comparing (A) 0.21 μm (B) 0.36 μm (C) 0.5 μm and (D) 1.2 μm GaN films on SiC(0001)_{Si} with (E) 0.24 μm and (F) 1.2 μm GaN films on sapphire.

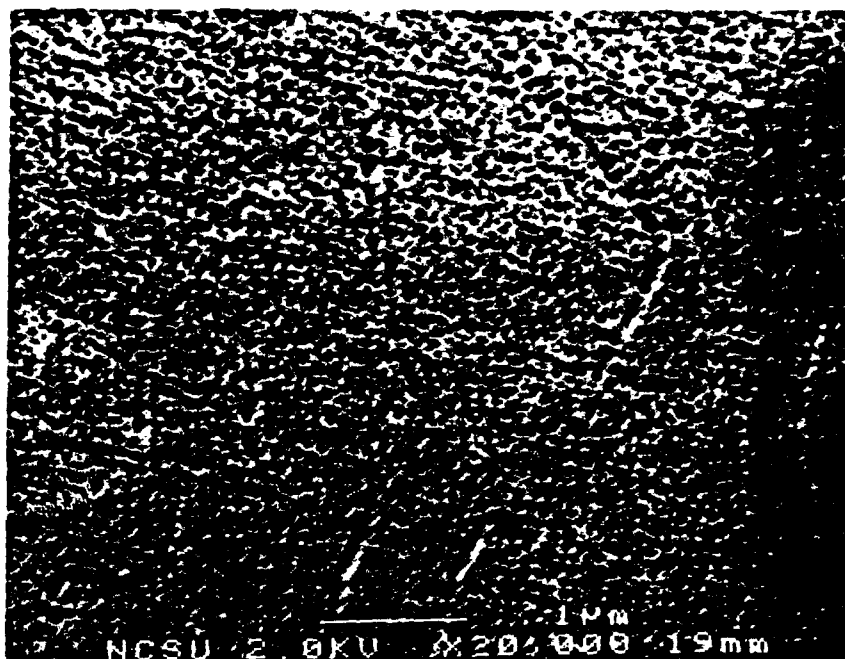


Figure 5. SEM micrograph of GaN deposited on SiC(0001)_{Si} at 900°C.



Figure 6. SEM micrograph of GaN deposited on SiC(0001)_C at 900°C.

accordance with the substrate polarity. He estimated that GaN films grown on sapphire and SiC(0001)_C were Ga terminated whereas films deposited on SiC(0001)_{Si} were N terminated. In agreement with Sasaki's findings, the present research revealed the surface morphologies

and PL spectra of GaN films on sapphire and the C-face wafers were similar to each other but unlike those of films deposited on the Si-face substrates. Although not shown, the PL spectrum for GaN deposited on SiC(0001)_C is nearly identical to spectrum E in Fig. 4 for GaN on sapphire.

Hall-effect measurements using the Van der Pauw geometry revealed that the unintentionally doped GaN films on SiC were highly n-type ($n_D - n_A > 10^{19} \text{ cm}^{-3}$). The highest observed room temperature Hall mobility for these films was $42 \text{ cm}^2/\text{V}\cdot\text{s}$. The average Van der Pauw resistivity was $1 \times 10^{-2} \Omega\cdot\text{cm}$. Residual nitrogen vacancies are likely to be the cause of the high net n-type behavior.

D. Conclusions

High quality GaN thin films have been deposited directly on vicinal, Si-face (6H)-SiC(0001) substrates without the aid of a low-temperature buffer layer. The near-band-edge PL peaks revealed an apparent shift to lower energies with decreasing GaN film thicknesses. These shifts were not observed for films deposited on sapphire. Also, the surface morphologies and PL spectra of GaN films on sapphire and C-face SiC(0001) wafers were similar to each other but unlike those of films deposited on the Si-face substrates.

E. Future Research Plans and Goals

In order to increase the deposition rates of the III-V nitrides, a pancake-style susceptor will be used in place of the current barrel design. Low-temperature AlN and GaN buffer layers will be utilized to investigate their effects on the microstructural and electrical qualities of the films. Both polar planes of SiC(0001) will be examined. Efforts will be made to identify and reduce the causes of the high net carrier concentrations in the unintentionally doped GaN films. Concurrently, a p- and n-type dopant study will be initiated for both GaN and AlN.

F. References

1. R. F. Davis, *Physica B* **185**, 1 (1993).
2. S. Yoshida, S. Misawa and S. Gonda, *Appl. Phys. Lett.* **42**, 427 (1983).
3. S. Yoshida, S. Misawa and S. Gonda, *J. Vac. Sci. Technol.* **B1**, 250 (1983).
4. H. I. Amano, N. Sawaki, I. Akasaki and Y. Toyoda, *Appl. Phys. Lett.* **48**, 353 (1986).
5. I. Akasaki, H. I. Amano, Y. Koide, K. Hiramatsu and N. Sawaki, *J. Cryst. Growth* **98**, 209 (1989).
6. T. Lei, M. Fanciulli, R. J. Molnar and T. D. Moustakas, *Appl. Phys. Lett.* **59**, 944 (1991).
7. S. Nakamura, M. Senoh and T. Mukai, *Jpn. J. Appl. Phys.* **30**, L1708 (1991).
8. H. Amano, M. Kito, K. Hiramatsu and I. Akasaki, *Jpn. J. Appl. Phys.* **28**, L2112 (1989).
9. S. Nakamura, T. Mukai, M. Senoh and N. Iwasa, *Jpn. J. Appl. Phys.* **31**, L129 (1992).
10. C. Wang and R. F. Davis, *Appl. Phys. Lett.* **63**, 990 (1993).
11. F. R. Chien, private communication (1994).

12. N. Kuwano, *et. al.*, J. Cryst. Growth **15**, 381 (1991).
13. M. E. Lin, B. N. Sverdlov and H. Morkoc, Appl. Phys. Lett. **63**, 3625 (1993).
14. I. Akasaki and H. I. Amano, "Photo- & cathodoluminescence of GaN and $\text{Al}_x\text{Ga}_{1-x}\text{N}$," in *Properties of Group III-Nitrides*, J. Edgar, ed., to be published.
15. T. Sasaki, T. Matsuoka and A. Katsui, Appl. Surf. Sci. **41/42**, 504 (1989).

XVI. Luminescence Studies of the GaN, AlN and Their Solid Solutions

A. Introduction

Luminescence is the emission of photons due to excited electrons in the conduction band decaying to their original energy levels in the valance band. The wavelength of the emitted light is directly related to the energy of the transition, by $E=h\nu$. Thus, the energy levels of a semiconductor, including radiative transitions between the conduction band, valance band, and exciton, donor, and acceptor levels, can be measured.[1,2]

In luminescence spectroscopy, various methods exist to excite the electrons, including photoluminescence (photon excitation) and cathodoluminescence (electron-beam excitation). In each technique, signal intensity is measured at specific wavelength intervals using a monochrometer and a detector. The intensity versus wavelength (or energy) plot can then be used to identify the characteristic energy band gap and exciton levels (intrinsic luminescence) of the semiconductor, and the defect energy levels (extrinsic luminescence) within the gap.[1]

Both photo- and cathodoluminescence analysis has been performed on AlN, GaN, and $\text{Al}_x\text{Ga}_{1-x}\text{N}$ semiconductors.[3-15] Much of the work has been in measuring the low temperature GaN luminescence peaks. Work on AlN has been limited by the energy gap of 6.2 eV, which corresponds to a wavelength (200 nm) that is lower than most of the optical light sources. An excimer laser using the ArF line (193 nm) could possibly be used, although no one has attempted this to date. However, cathodoluminescence can be used on AlN.

Few time-resolved luminescence measurements have been performed on AlN and GaN. In a time-resolved measurement a pulsed source is used to excite the sample, and the luminescence is measured at short sampling intervals after the pulse. The result is an intensity vs. time plot. Time resolved spectroscopy is useful for separating the emission bands of the investigated samples with different decay times. It is often used to measure donor-acceptor recombination rates and minority carrier lifetimes.

Depth-resolved information can be obtained using cathodoluminescence, since generation depth varies with beam voltage. This technique is particularly useful for studying ion implanted semiconductors and layered structures.

B. Experimental Procedures

A combined photo- and cathodoluminescence system is used to measure the luminescence from the III-V Nitrides. A schematic view is shown in Fig. 1, and a block diagram is shown in Fig. 2. Each sample is attached to a cryostat that allows for a test temperature range of 4.2 to 400 K. A McPherson model 219 vacuum monochrometer

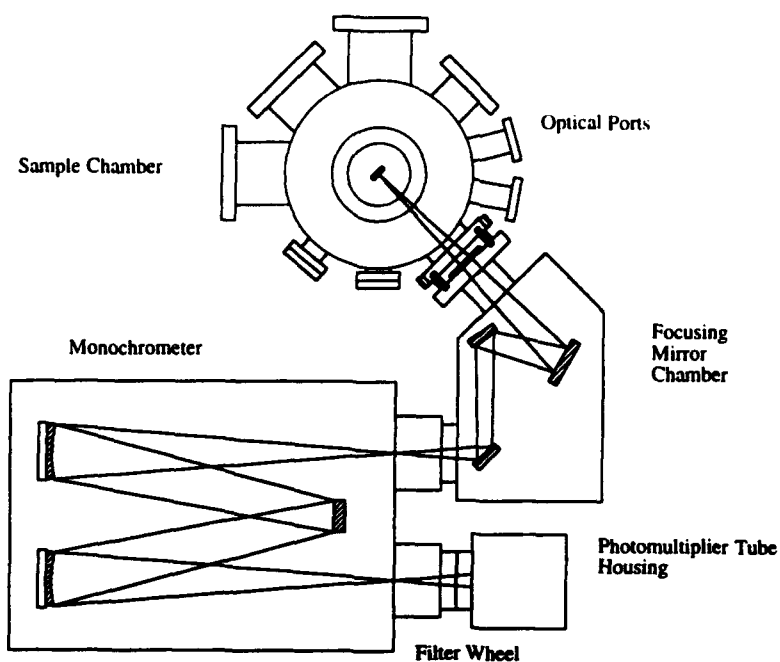


Figure 1. Schematic view of combined photo- and cathodoluminescence system.

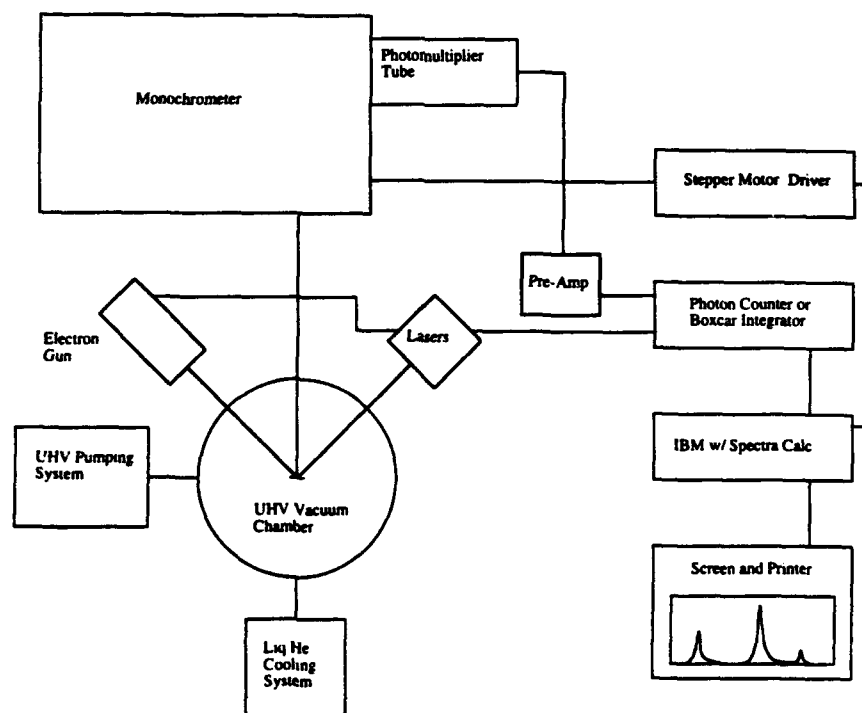


Figure 2. Block diagram of combined photo- and cathodoluminescence system.

with a focusing mirror chamber is used to collect the emitted light. The focal length of the monochromator is .5 m, with a wavelength resolution of .04 nm at 313.1 nm. A photon counting detection scheme is used to measure the light intensity, using a photomultiplier tube that is most efficient from 185-600 nm. A lock-in amplifier will soon be added for wavelength laser that operates at a wavelength of 325 nm (3.8 eV), with a power of 15 mW. It is used for PL tests of GaN, but a lower wavelength source is needed to test the full range of the $\text{Al}_x\text{Ga}_{1-x}\text{N}$ solid solutions. A pulsed excimer laser is proposed as the other optical source; it operates at wavelengths of 193 nm (6.4 eV) and 248 nm (5.0 eV).

A Kimball Physics electron gun is used for cathodoluminescence measurements. It has maximum beam voltage of 10 keV and a maximum beam current of 450 uA. By varying the beam voltage it is possible to perform depth-resolved spectroscopy.

The beam blanking capability of the electron gun will allow for time-delay studies of the semiconductors.

C. Results and Discussion

Photoluminescence measurements were performed on GaN films grown via CVD on both 6H-SiC and sapphire substrates. Each test was performed at 20 K. The results for films of various thicknesses is shown in Fig. 3. For the thickest (1.2 μm) GaN films (Fig. 3 (D) and (F)) the highest energy peaks are at 357.6 nm (3.471 eV). These peaks are attributed to the recombination of donor bound excitons.[3] Figure 3 also shows a shift in this peak to a lower energy (higher wavelength) as film thickness decreases. For the thinnest film tested (210 nm) the peak is at 368 nm (3.37 eV). For GaN on sapphire at a similar thickness the peak shift is not as strong, with the peak at 359 nm (3.457 eV). This result is expected, since the large lattice mismatch of GaN on sapphire results in film relaxation at a lower thickness.

There is also a second, lower energy peak in all of the samples, it is located at 375-378 nm (3.31-3.28 eV) for all the samples. This feature does shift much with film thickness for the GaN films on either substrate. It is tentatively designated as a donor-acceptor (DA) transition. It is also possible that this transition is due to yet unidentified defects within the film, and tests on thicker samples will be needed for positive identification of this feature.

In each of the samples tested there is a broad emission band centered at 2.2-2.3 eV, similar to that seen in Fig. 4. This is a common feature of GaN films, and its origin is still up for debate.[16] Recent work suggests a donor-acceptor pair (DAP) recombination of electrons from N vacancies (deep donor states) and holes from C-related acceptors states.[17]

The photoluminescence of GaN grown on the (0001)_C and (0001)_{Si} planes of 6H-GaN was also investigated. Each film was 210 nm thick, and the tests were performed at 15 K. The results are shown on Fig. 4. The near-band gap peak for the GaN on the C-plane is at 360 nm,

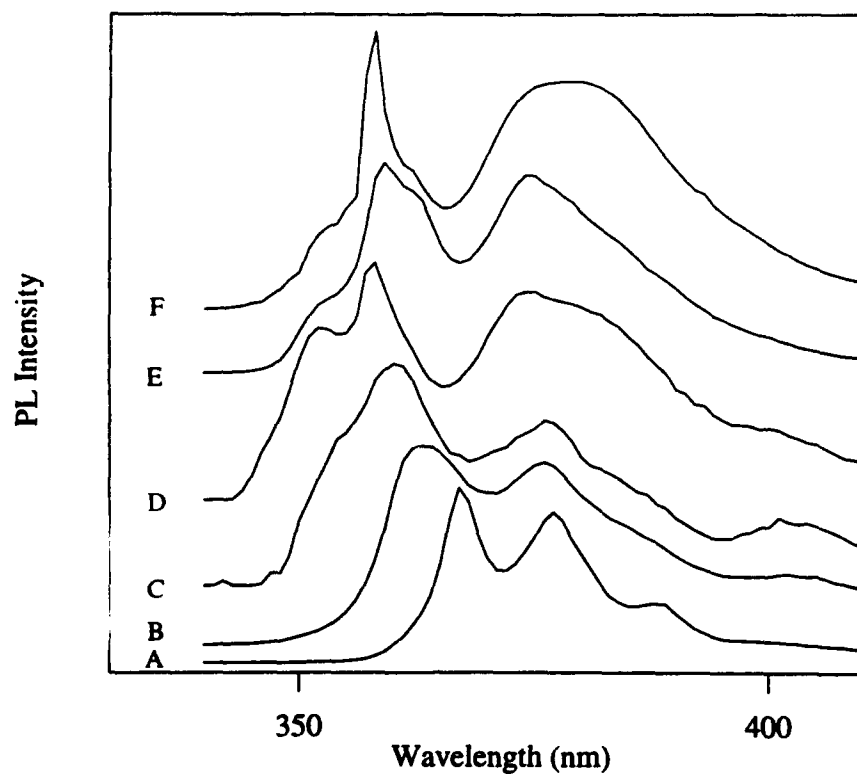


Figure 3. PL spectra comparing (A) .21 μm (B) .36 μm (C) .5 μm and (D) 1.2 μm GaN films on SiC with (E) .24 μm and 1.2 μm GaN films on sapphire.

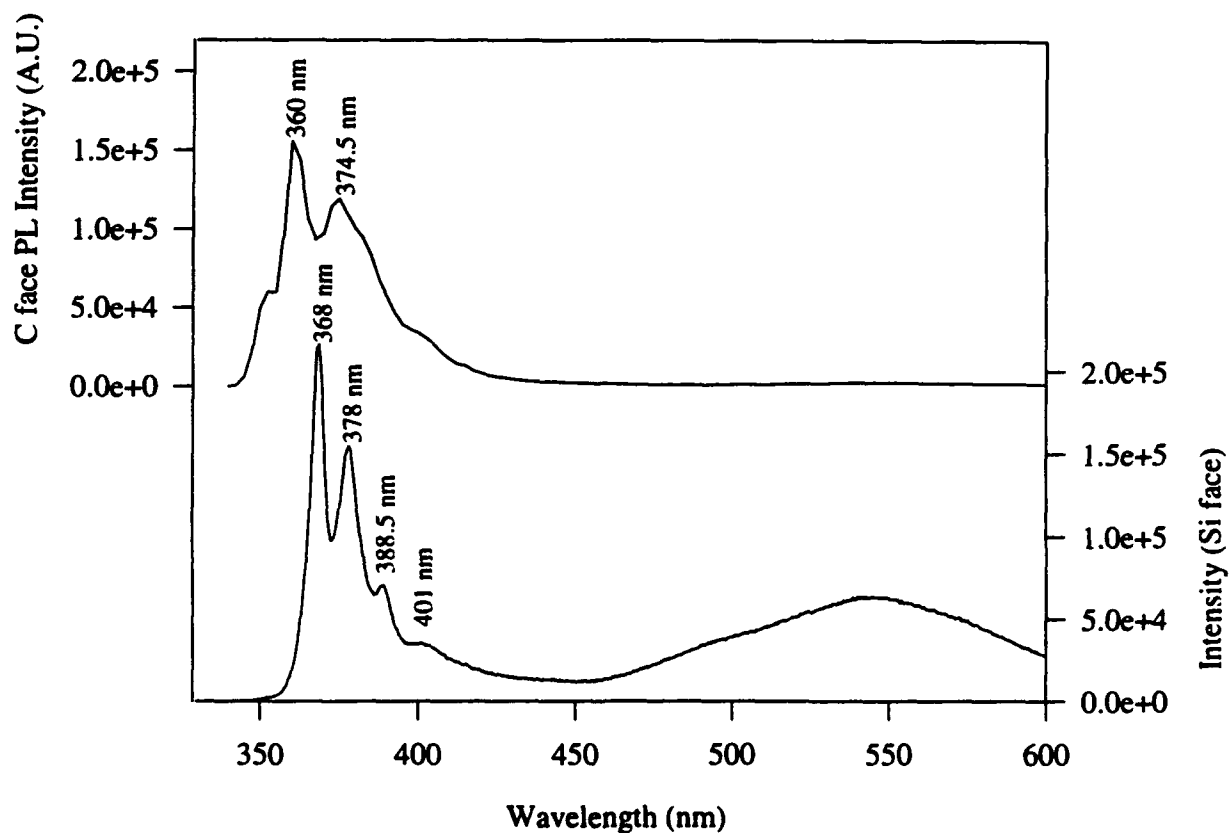


Figure 4. Comparison of the PL spectra for GaN on the Si and C planes of SiC.

and for the Si-plane it was at 368 nm. These results are similar to the GaN films on sapphire and SiC [Figs 3(E) and (A)]. Figure 4 also shows that the broad emission peak at 2.2-2.3 eV is most intense for the film grown on the Si-plane of SiC, and this is also the case when comparing GaN grown on SiC and sapphire (not shown). These results are not unexpected, as similar results for thicker GaN films were seen by other investigators.[18]

The GaN film on the Si-plane of SiC [Fig. 4] also exhibited sharp peaks at 378 nm (3.28) and 388.5 nm (3.2 eV), with a shoulder at 401 nm (3.09 eV). The last two peaks are believed to be phonon replicas of the previously discussed (DA) transition seen at 3.28 eV. These features are not seen in the thicker GaN films because of the broadness of the peak at 3.28-3.31 eV.

D. Conclusions

Photoluminescence tests have been performed on GaN films grown via CVD on both 6H-SiC and sapphire substrates. All of these films were thin, ranging from .21 to 1.2 μm . Tests were performed at 15-20 K. For the thickest samples (1.2 μm) a main peak attributed to recombination of donor bound excitons was seen at 357.6 nm. This peak shifted to higher wavelength as film thickness decreased. A second peak seen at 375-378 nm was seen all the samples, this was tentatively assigned to Donor-Acceptor transitions. A third broad emission band centered at 2.2-2.3 eV was seen in all the samples tests.

E. Future Research Plans and Goals

Thick GaN films ($>2\mu\text{m}$) with buffer layers will be studied at low temperature to test the true film quality. Using these results it will be easier to understand and verify the current data for the films tested to date. The change in luminescence as a function of film thickness will further be investigated, for both SiC and sapphire substrates with and without buffer layers. The effect of temperature on luminescence will also be studied for the range of 10 K to 450 K, and the results will be used to study the activation energy for the donor-bound excitons.

Cathodoluminescence will be used to study $\text{Al}_x\text{Ga}_{1-x}\text{N}$ alloys grown by both CVD and GS-MBE. A excimer waveguide laser will also be added to the system, with a peak emission at 193 nm. This will allow for photoluminescence measurements of AlN, which has not been done yet above the band gap. Cathodoluminescence will also be used to perform depth-resolved spectroscopy of GaN, AlN and their alloys.

F. References

1. B. G. Yacobi and D. B. Holt, *Cathodoluminescence Microscopy of Inorganic Solids*, Plenum Press, New York (1990).

2. M. D. Lumb, Ed., *Luminescence Spectroscopy*, Academic Press, New York (1978).
3. S. Strite and H. Morkoç, *J. Vac. Sci. Technol. B* **10** (4), 1237-1266 (1992).
4. R. A. Youngman and J. H. Harris, *J. Am. Ceram. Soc.* **73** (11), 3238-46 (1990).
5. M. A. Kahn, R. A. Skogman, J. M. Van Hove, S. Krishnakutty, and R. M. Kolbas, *Appl. Phys. Lett.* **56** (9130), 1257-59 (1990).
6. V. F. Veselov, A. V. Dobrynin, G. A. Naida, P. A. Pundur, E. A. Slotensietse, and E. B. Sokolov, *Inorganic Materials* **25** (9), 1250-4 (1989).
7. J. N. Kuznia, M. A. Kahn, D. T. Olson, R. Haplan, and J. Freitas, *J. Appl. Phys.* **73** (9), 4700-4702 (1993).
8. M. R. H. Khan, N. Sawaki and I Akasaki, *Semiconductor Science and Technology* **7**, 472-7 (1992).
9. K. Maier, J. Schneider, I. Akasaki, and H. Amano, *Jpn. J. Appl. Phys.* **32** (6), 846-848 (1993).
10. I. Akasaki, and H. Amano, *J. Crystal Growth* **99**, 375-80 (1990).
11. S. Yoshida, H. Okumura, S. Misawa, and E. Sakuma, *Surf. Sci.* **267** (7), 50-53 (1992).
12. S. Nakamura, T. Mukai, and M. Senoh, *Jpn. J. Appl. Phys.*, **31** (9) 2883-90 (1992).
13. S. Nakamura, N. Iwasa, T. Mukai, and M. Senoh, *Jpn. J. Appl. Phys.* **31** (5), 107-15 (1992).
14. S. Nakamura, T. Mukai, and M. Senoh, *Jpn. J. Appl. Phys.* **30** (12A), 1998-2001 (1991).
15. S. Strite, J. Ruan, Z. Li, N Manning, A. Salvador, H. Chen, D. J. Smith, W. J. Choyke, and H. Morkoç, *J. Va. Sci. Technol. B* **9** (4), 1924-29 (1991).
16. E. R. Glaser, T. A. Kennedy, H. C. Crookham, J. A. Freitas, Jr., M. Asif Khan, D.T. Olson, and J. N. Kuznia, *Appl. Phys. Lett.* **63** (19), 2673-2675 (1993).
17. E. R. Glaser, T. A. Kennedy, J. A. Freitas, Jr., M. Asif Khan, D. T. Olson, and J. N. Kuznia, from the Fifth International Conference on Silicon Carbide and Related Materials in Washington, D.C., Nov. 1993, to be published in the "International Institute of Physics Conferences" Series.
18. T. Sasaki, T. Matsuoka, A. Katsui, *Appl. Surf. Sci.* **41/42**, 504-508 (1989).

XVII. Contact Formation in GaN and AlN

A. Introduction

The formation of ohmic contacts with semiconductor materials and devices is a fundamental component of solid state device architecture. As device size has diminished and the scale of integration has increased, the quality of these interfaces has become an increasingly important concern. In addition, the presence of parasitic resistances and capacitances, such as those existing at contact interfaces, becomes more detrimental at higher operating powers and higher oscillation frequencies. The development of adequate and reliable ohmic contacts to the compound semiconductors, particularly those with wider band gaps, has met a number of challenges. The subject of ohmic contacts to p- and n-type III-V compounds, mostly GaAs, AlGaAs, and InP, has received a great deal of attention over the past decade, and significant advances have been made [1-12]. By comparison, the III-V nitrides have received little attention in this regard. However, interest in these materials has been renewed in recent years as thin film growth techniques have improved, p-type doping in GaN and AlGaN solid solutions has been achieved, and p-n junctions have been fabricated.

The majority of successful ohmic contact systems that have so far been implemented with the more conventional compound semiconductors have relied upon alloying (liquid-phase reaction) or sintering (solid-phase reaction) via post-deposition annealing treatments, and/or the presence of high carrier concentrations near the interface [1,2,6,12]. However, many otherwise successful ohmic contact systems have only limited thermal stability and are subject to degradation, usually in the form of extensive interdiffusion, interfacial reaction, and interphase growth, accompanied by increase in contact resistivity, under subsequent thermal processing steps. It is reasonable to suppose that the cleanliness and preparation of the semiconductor surface prior to contact deposition plays a significant role in the behavior of the interface, and there are indications in the recent literature that support this [2,11-13]. Thorough oxide removal is especially important, though it may well prove to be a persistent challenge with Al-containing compounds in particular.

In this study, two main approaches are being taken in the development of ohmic contacts to GaN and AlN. The first approach is similar to that which has resulted in the majority of successful ohmic contacts to the more conventional compound semiconductors such as GaAs: the creation of high carrier concentrations in the semiconductor at the metal interface by means of alloying, sintering, or implantation of dopant species. The so-called pinning of the Fermi level at this surface, particularly with GaAs, results in a more or less fixed potential barrier at the metal interface. In the case of the pinned Fermi level of GaAs, the approach has generally been to shrink the width of the depletion layer by means of increasing the carrier concentration to the point where carrier tunneling through the barrier occurs readily. Even

with optimization of contact composition and annealing times and temperatures, the lowest contact resistivities (ρ_c) have been obtained only on the most heavily doped materials. Though there are indications that high doping levels and extensive interfacial reactions through alloying and sintering are not essential for ohmic contact formation in all cases, these processes have proven useful for minimizing ρ_c [2,11-13].

The other approach toward ohmic contact formation to be taken in this study involves the Schottky-Mott-Bardeen (SMB) model of semiconductor interfaces [14,15]. In this model the relative values of work function of the materials involved determine the band structure of the interface and thus the nature of any potential barriers present. The presence of interfacial states at the semiconductor surface can interfere with the alignment of the Fermi level across the interface and overshadow the effect of the inherent difference in work function between the two materials. The III-V nitride compounds are more ionically bonded than their phosphide and arsenide counterparts, as a result of larger electronegativity differences between the component elements. According to the observations of Kurtin *et al.* [16], this fact indicates that the nitrides should experience less Fermi level stabilization or "pinning" at the surface than do the more covalent compounds. Thus, the barrier heights of contacts to the nitrides should be more dependent on the contact material than is the case with the more conventional and more covalent semiconductors such as Si, GaAs, InP, SiC, etc. With the work of Foresi and Moustakas [17,18], this concept is beginning to be investigated. The SMB model also indicates that the cleanliness of the interface plays an important role in its electrical behavior, particularly in the minimization or elimination of any insulating layers at the interface.

To date, several alloyed and sintered contact strategies, having demonstrated effectiveness with GaAs and, in the case of Au, with GaN, have been undertaken with GaN and AlN. The tighter bonding of Ga and Al to N, in comparison to As, suggests that higher temperatures and possibly longer times are required for interfacial reactions to take place, and that some reactions may be inhibited or prevented. The behavior of the systems examined so far has been consistent with these suppositions. Contact strategies involving the concentration of active dopant species at the contact interface will continue to be characterized in this study, as well as the investigation of the roles of work function differences and interfacial cleanliness. In the present reporting period, both of these approaches to contact formation were continued.

One area of contacts development that has received a significant amount of attention is that of the metal silicide compounds. Silicide thin films have been extensively studied and applied as contacts and interconnects, mostly for silicon-based technology [19-24]. In comparison, the properties of the metal germanides are not well documented. As a general rule, germanides have been found to be more resistive than silicides and their chemistry with

Si-based materials more complex. However, in a series of studies, M. O. Aboelfotoh *et al.* have shown that a particular phase of copper germanide, specifically the ordered monoclinic phase ϵ_1 -Cu₃Ge, is an exception to these rules [25-28]. Thin films of Cu₃Ge exhibit remarkably low resistivities, unlike Cu₃Si, and unlike both Cu and Cu₃Si, are surprisingly stable with respect to oxygen and air exposure. As such, Cu₃Ge presents itself as a potentially useful contact metal. Indeed, preliminary experimentation with Cu₃Ge contacts on GaAs and GaN, primarily on n-type and heavily-doped p-type material, has produced some favorable results in terms of ohmic contact formation. For these reasons copper-germanium contacts were investigated during this reporting period as possible candidates for high-quality, low-resistivity ohmic contacts.

B. Experimental Procedure

Film Deposition. Doped GaN and AlN films for contact studies were grown on 6H-SiC substrate crystals, supplied by Cree Research, Inc., by means of ECR plasma-enhanced molecular beam epitaxy (MBE). Magnesium was grown into the films as the p-type dopant and Ge was used to grow n-type materials, as described in other sections of this report.

Two different contact systems were deposited and examined during this reporting period: single Al layers and an alloyed compound of CuGe. The single Al layers were 2500Å thick; the Cu/Ge contact consisted of 800Å layers of Cu followed by 1200Å of Ge. Contact metals were deposited by means of electron beam evaporation using a Thermionics evaporation system having a 3 kW 5-source electron gun. The 5-source capacity of the e-beam hearth allowed the deposition of multiple layers of different metals in the same vacuum run. Prior to metals deposition, the nitride films were cleaned with a 50:50 HCl:H₂O dip and carefully pulled dry from the solution. A shadow mask was used during deposition to create rectangular-bar TLM (transmission line model) patterns for contact resistivity (ρ_c) measurements, as described in the earlier semiannual report of June 1993. Film thicknesses were monitored using a quartz crystal oscillator.

Contact Characterization. After deposition, I-V measurements were taken between separate pads of the TLM patterns, using tungsten probe tips and an HP 4145C Semiconductor Parameter Analyzer. Measurements were made at room temperature, 200°C, 350°C, and 500°C. Annealing treatments were performed in a flowing N₂ atmosphere at successively higher temperatures using a Heatpulse 410 rapid thermal annealing (RTA) furnace. TLM measurements were taken by measuring the total resistance between identical contact pads as a function of separation distance. The contact resistivity was obtained from the plot of $R(l)$ vs. l , as described by Reeves and Harrison [29]. The simplifications inherent in this model yield values for ρ_c that represent an upper limit; thus, the measured values are conservative assessments of performance.

In addition to electrical characterization, the contact samples in this study were also prepared for cross-sectional TEM analysis by Dr. Moon Kim and Dr. Yi Huang at the Center for Solid State Science at Arizona State University. At the time of the writing of this report, preliminary microstructural and crystallographic characterization had been performed and compositional analysis by means of energy-dispersive x-ray analysis (EDS) and electron energy loss spectroscopy (EELS) was being undertaken.

C. Results

Al contacts on Ge:GaN. Aluminum contacts deposited on germanium-doped GaN were ohmic and exhibited low contact resistivity in the initial as-deposited condition. The I-V behavior of the as-deposited contacts is plotted in Fig. 1. As the plot shows, the I-V relationship of the Al contacts on Ge:GaN is completely linear. In addition, this contact system, at temperatures below 550°C, exhibited a much lower contact resistivity than others yet investigated in this study: from TLM measurements the contact resistivity ρ_c was found to be $1 \times 10^{-4} \Omega \text{ cm}^2$ at room temperature and $< 7.5 \times 10^{-6} \Omega \text{ cm}^2$ at 500°C. These results compare very favorably with those reported by Foresi and Moustakas [17,18], and, more recently, Lin *et al.* [30], who obtained ρ_c values of 1×10^{-3} and approximately $1 \times 10^0 \Omega \text{ cm}^2$ respectively. The samples were heat-treated at 450°C, 550°C, and 650°C for 3 min at each temperature; TLM measurements were performed at room temperature and elevated temperatures, 200°C, 350°C, and 500°C, after every heat treatment. The effects of this heat treatment on the contact resistivity is plotted in Fig. 2. As would be expected from basic semiconductor principles, the measured resistances and contact resistivities were generally lower at higher temperatures due to the greater availability of free charge carriers. After annealing at 450°C, the behavior of the Al contacts was essentially unchanged. However, the 550°C and 650°C anneals resulted in an overall increase of contact resistivity, even with the reduced resistances that occurred at higher measurement temperatures. After annealing to 650°C, the contact resistivity stabilized at $2 \times 10^{-3} \Omega \text{ cm}^2$.

CuGe contacts on Ge:GaN and Mg:GaN. As the Cu and Ge components of this contact system were deposited sequentially, the as-deposited contacts consisted of a layer of Cu forming the interface to the GaN surface. The designation Cu/Ge, using a slash between the contact metals, is used here to indicate the initially distinct and separate layers of the metals; the designation CuGe is used to refer to the contact layers after alloying of the two had taken place. The unalloyed Cu/Ge contact layers produced ohmic but fairly high-resistivity contacts, as shown in Fig. 3. As can be seen in the I-V plots, the Cu/Ge contact layer on the Mg-doped GaN produced a noticeably more conductive contact than it did on the Ge-doped GaN. After some experimentation with Cu/Ge test films, an alloying RTA heat treatment of 475°C for 15 s was chosen and the samples were thus treated. After the alloying treatment,

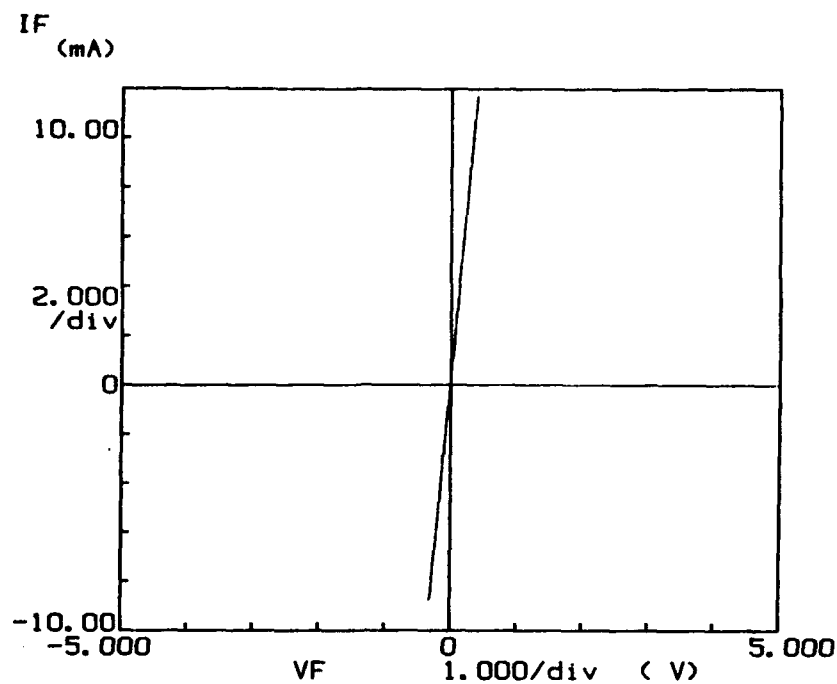


Figure 1. I-V data for as-deposited Al contacts on Ge-doped GaN.

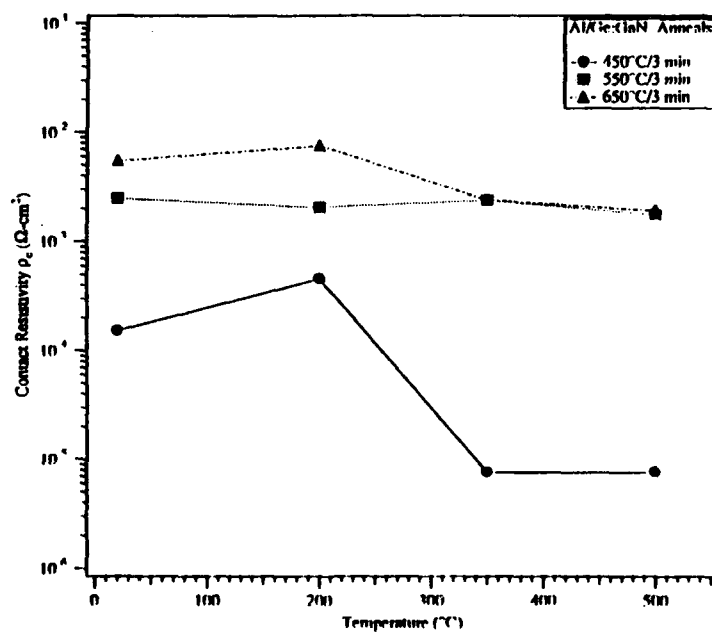


Figure 2. Contact resistivities of Al/Ge:GaN from high temperature TLM measurements, as a function of heat treatment.

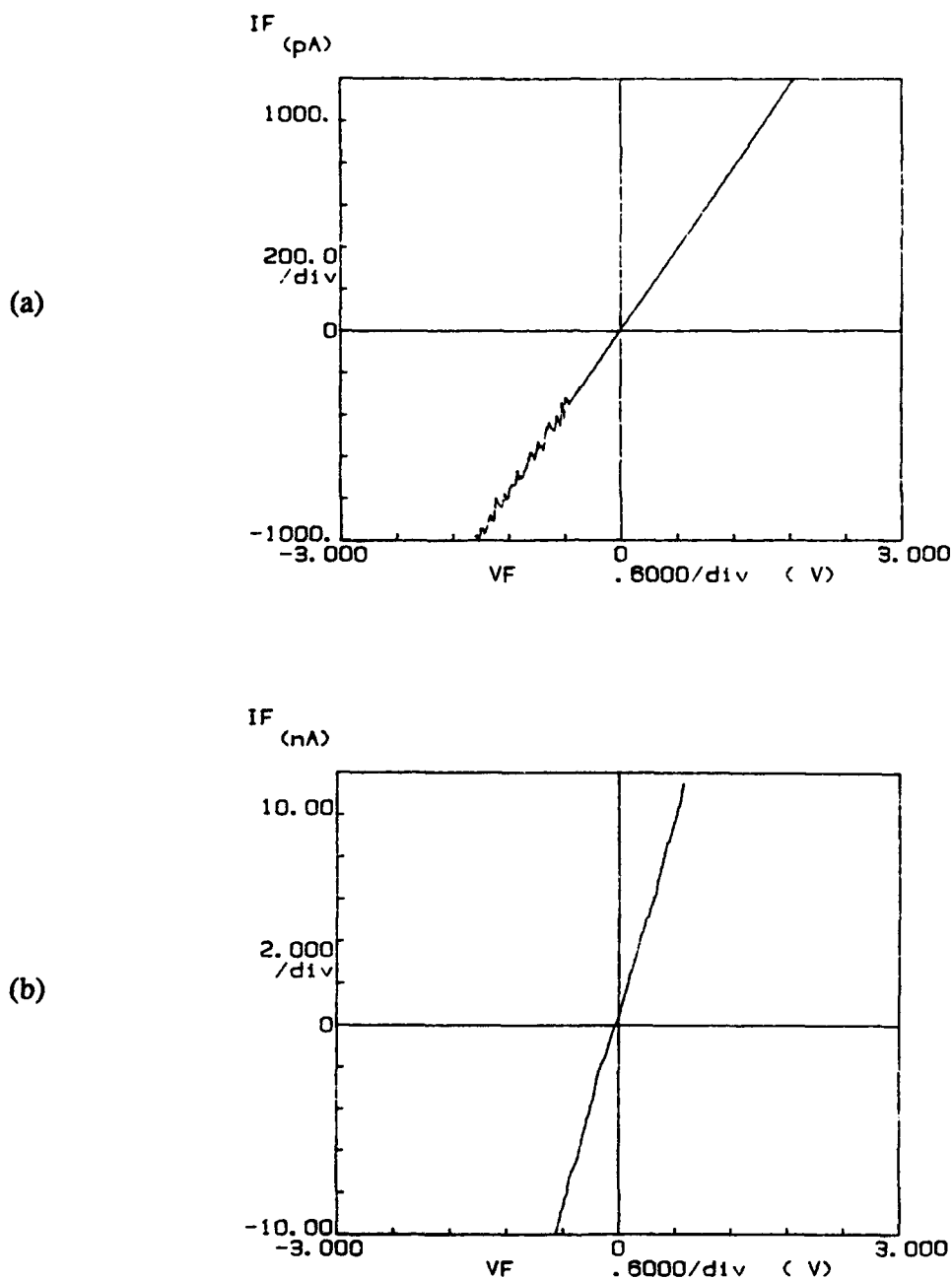


Figure 3. As-deposited I-V data for CuGe contacts on GaN: (a) on Ge:GaN (b) on Mg:GaN.

I-V measurements revealed that the total resistances and the ρ_c of the contact samples increased substantially, though the behavior in both cases remained essentially ohmic. Further annealing of the alloyed contacts did not improve the contact resistivity of either system; both remained highly resistive, and the CuGe contact metal did not appear to be stable at temperatures above 600°C.

An SEM image of the as-deposited Cu/Ge contacts is shown in Fig. 4, which is representative of the contacts on both the Ge-doped and the Mg-doped GaN films. At this stage the two separate metal layers can be distinguished, and the Ge top surface is very smooth. After the 475°C alloying treatment, however, the contacts became substantially different in appearance. The alloyed CuGe contacts on Ge:GaN are shown in Fig. 5. In this image the two metal layers are much less distinguishable than before; the "beading up" of the metal near at the edge of the contact pad indicates that the metal species experienced a significant amount of mobility, and also that the surface free energy difference between the metal and the semiconductor is not favorable for good "wetting" and adhesion. The metal films peeled at the edges when subjected to thermal stresses, but in general the CuGe films on Ge:GaN adhered fairly well. By comparison, the alloyed CuGe contacts on Mg:GaN, shown in Fig. 6, experienced a significant amount of metal debonding and peeling due to poor adhesion of the metal layer to the GaN surface. The surface of each contact pad indicated that the entire pad layer had experienced buckling and wrinkling, permitted by its lack of adhesion to the GaN surface. Overall each contact pad buckled, but on a finer scale the CuGe metal surface remained relatively smooth.

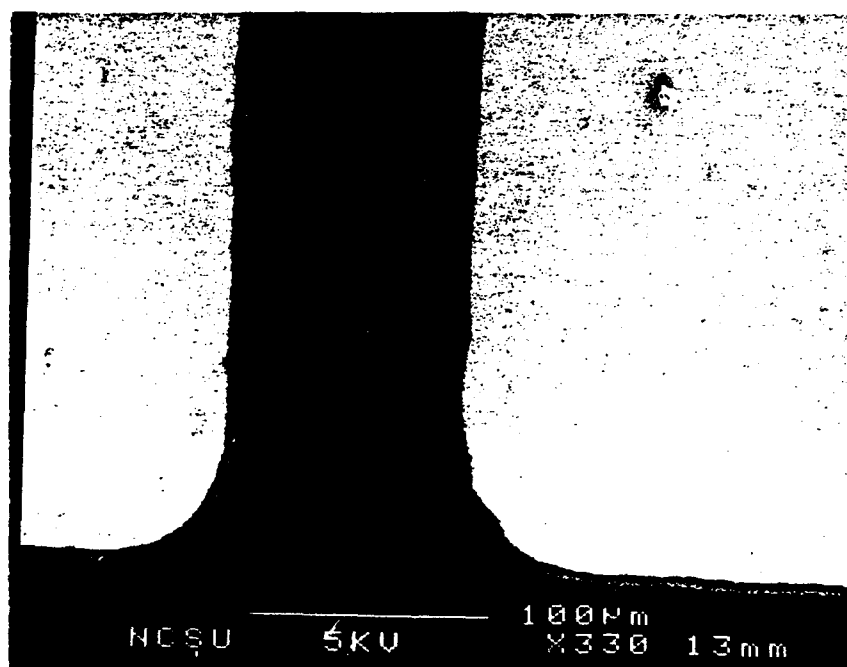


Figure 4. SEM image of the surface of unalloyed Cu/Ge contact pad on Ge:GaN.

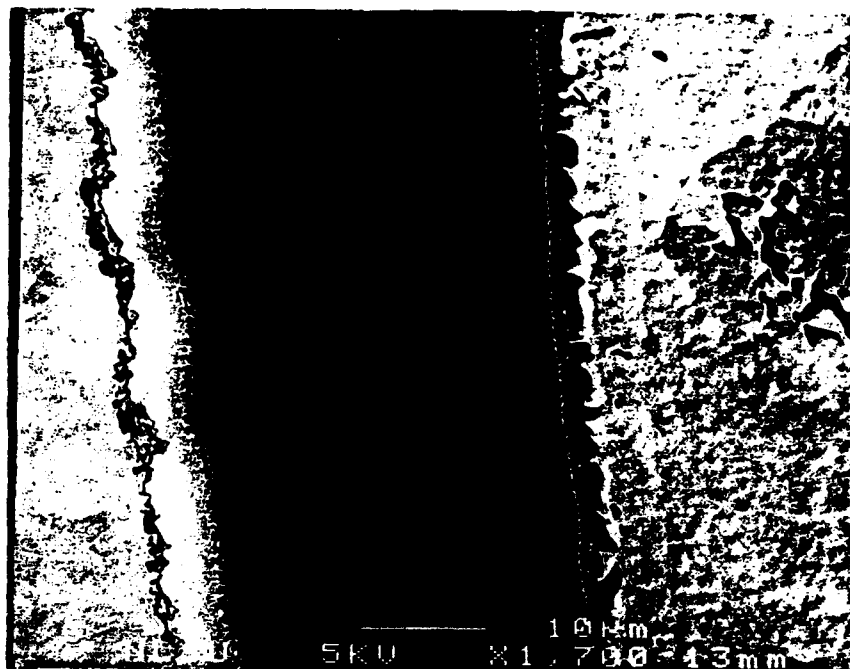


Figure 5. SEM image of CuGe contact pad on Ge:GaN, after alloying at 475°C for 15 s.

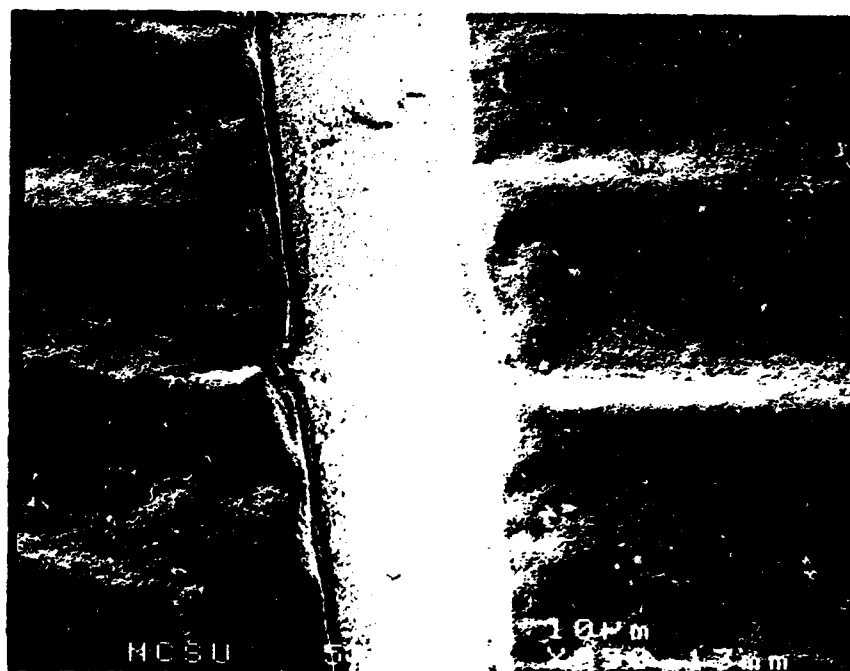


Figure 6. SEM image of CuGe contact pad on Mg:GaN, alloyed at 475°C for 15 s.

D. Discussion

Al contacts on Ge:GaN. That the as-deposited Al contacts on Ge-doped GaN would prove to be ohmic is consistent with the Schottky-Mott-Bardeen model, based on the relationship of the work functions of the two surfaces. Aluminum is a relatively low-work function metal ($\phi_{Al}=4.2$ eV) and thus may provide a favorable band offset for ohmic contact formation to an n-type semiconductor (ϕ_{GaN} estimated to be 4.1 eV). However, it should be pointed out that the exact value for the work function and/or electron affinity of GaN and their dependence upon doping levels have not been reproducibly and precisely established as yet. As stated above, the results of these contact resistivity measurements compare very favorably with those reported by Foresi and Moustakas [17,18], and, more recently, Lin *et al.* [30]. The GaN materials used by both of these groups were different than those used in this study; theirs were unintentionally doped and inherently n-type, indicative of high background carrier concentrations (about 10^{17} cm⁻³ in both cases) and defect densities. Hall measurements of Ge:GaN films similar to those used for contact deposition and TLM measurements in this study yielded carrier concentrations of about 3×10^{19} cm⁻³ with mobilities of approximately 100 cm² V⁻¹ cm⁻¹. Given the fact that contact resistivities tend to be strongly affected by bulk and surface carrier concentrations, it is not surprising that these highly doped Ge:GaN films produced low-resistivity contacts. However, contacts need to be made to more lightly doped material as well, and steps can be taken to improve the performance of such contacts, as described above.

The samples were annealed for short periods of time in an RTA furnace under flowing N₂. The purpose of performing the annealing under N₂ at atmospheric pressure for short times was to reduce the likelihood of generating N vacancies which are believed to be shallow donors that contribute to the background carrier concentration. While increasing the background carrier concentration may contribute to greater current transport in the semiconductor and across the contact interface and apparently reduce the ρ_c , in general such behavior would be detrimental to overall electronic properties and device performance. More extensive characterization of the electronic properties of our nitride films is needed to better correlate and understand the relationship between dopant concentration, carrier concentration and mobility, Fermi levels, and contact behavior. Improvements in our measurement capabilities, in terms of both equipment and sample preparation techniques, are underway.

Characterization by means of cross-sectional TEM (X-TEM) is being performed to investigate the interfacial structure in detail. The preliminary results of this analysis indicate that an intermediate phase formed at the Al/GaN interface, possibly a form of GaAl or GaAlN, as a result of annealing. The appearance of this interfacial phase as a result of annealing correlates with an increase in contact resistivity, which suggests the formation of higher-resistivity materials at the interface and thus may indicate the presence of Al or GaAl

nitride formation. Aluminum nitride has a very large and negative free energy of formation and thus the reaction is energetically favored where there is sufficient thermal mobility. Interfacial reactions with contacts on GaAs typically play important roles in the electrical properties of the contacts. The roughening of the interface due to reaction and phase formation may help to lower ρ_c by increasing the area of contact between the metal layer(s) and the semiconductor. Gallium nitride lacks the very mobile As species and has stronger interatomic bonding, but sufficiently high temperatures and favorable chemistry can nevertheless free the Ga and N from one another. Depth profiling and cross-sectional examination will allow further clarification of these issues.

CuGe contacts on Ge:GaN and Mg:GaN. To date, the properties of Cu_3Ge films have been documented by Aboelfotoh *et al.*, but the interfacial properties of CuGe contacts to semiconductor surfaces are only beginning to be investigated. The results of TLM measurements show that CuGe, and also Cu contacts, in the as-deposited state, form ohmic contacts on both Ge:GaN and Mg:GaN. At the present time the work function and electron affinity properties of CuGe compounds have not yet been studied, so it is not known how this contact system compares with the Schottky-Mott-Bardeen model. It is possible that even if a pure contact metal does not have a favorable work function relationship to a semiconductor for ohmic contact formation according to the Schottky model, some of the interfacial compounds that may form could be more favorable. The time interval and temperature of the alloying and/or contact annealing steps evidently have a significant effect on the resulting current-carrying abilities of the contacts, by influencing the rate and amount of any interfacial diffusion that can take place and the reactions that can occur at the interface. Further refinement of the alloying/annealing procedures may improve the performance of the contacts considerably.

The weak adhesion of the CuGe layers to the GaN surfaces probably compromised the performance of the contacts, but is not particularly surprising given the fact that there is little likelihood of chemical bonding of the Cu layer, which was deposited first, to the GaN layer. Copper does not form nitrides readily, while the CuGe compounds form very readily at fairly low temperatures. The SEM images of both alloyed CuGe contact samples show evidence that the originally distinct Cu and Ge layers formed a single metal film after a relatively quick, low-temperature anneal. The fact that the films debonded more easily as a result of thermal stresses indicates a significant difference in thermal expansion characteristics between the CuGe and the GaN surface. All of these factors have an effect on the behavior of the contacts; there is still a greater range of heat treatment parameters yet to be studied, which may result in substantial improvements in contact performance.

E. Conclusions

The work conducted in this study so far has shown that it is possible to form metal contacts with ohmic, linear I-V behavior to doped GaN and AlN films. The Al contacts on Ge-doped GaN had very good low-resistivity characteristics and remained stable to at least 500°C; so far this contact system exhibits better performance characteristics than any other investigated in this study to date, and better characteristics than most contacts yet reported for GaN. As yet the CuGe contacts exhibit high contact resistivities, even on the higher carrier concentration Ge:GaN material, but it is reasonable to expect that refinement of contact metals choice, surface cleanliness, and deposition procedures will result in substantial improvements. In the contact systems studied to date, there are indications that interfacial reactions took place during annealing that correlated with the development of linear I-V behavior and reductions in ρ_c . Further characterization of these contacts, particularly the compositional information obtained from X-TEM analysis, is needed to understand the chemical and structural changes that took place in the contacts as a result of thermal treatment.

F. Future Plans and Goals

In addition to further chemical and structural characterization of the contact systems described in this report, other promising contact candidates will be investigated. Titanium nitride as an ohmic contact candidate for n-type nitride semiconductors was described in a preceding semiannual report (June 1993), and will be examined along with the more conventional metal systems. Another contact approach to be investigated involves the deposition of high carrier concentration, moderate band gap InN as an interlayer to provide improved band offsets and better carrier transfer across the metal-nitride interface, as proposed by Abernathy *et al.* [31]. Combined with the search for improved contacts to the III-nitrides is the ongoing investigation of Fermi-level pinning and defect states, and the role played by work function and electron affinity differences in contact properties. The evidence examined to date indicates that GaN does indeed experience much less Fermi-level pinning than its more covalently bonded relatives such as GaAs; further work will help to clarify this issue and assist the development of advanced microelectronic and optoelectronic devices.

G. References

1. T. C. Shen, G. B. Gao, H. Morkoç, J. Vac. Sci. Technol. B 10(5), 2113 (1992).
2. R. Williams, *Modern GaAs Processing Techniques* (Artech House, Norwood, MA, 1990).
3. M. Murakami, Materials Science Reports (5) 273 (1990).
4. A. Piotrowska and E. Kaminska, Thin Solid Films 193/194, 511 (1990).
5. A. Piotrowska, A. Guivarc'h and G. Pelous, Solid-St. Electron. 26(3), 179 (1983).

6. V. L. Rideout, *Solid-St. Electron.* **18** 541 (1975).
7. K. Tanahashi, H. J. Takata, A. Otsuki and M. Murakami, *J. Appl. Phys.* **72**(9), 4183 (1992).
8. H. J. Takata, K. Tanahashi, A. Otsuki, H. Inui and M. Murakami, *J. Appl. Phys.* **72**(9), 4191 (1992).
9. M. C. Hugon, B. Agius, F. Varniere, M.F. roment and F. Pillier, *J. Appl. Phys.* **72**(8), 3570 (1992).
10. W. O. Barnard, G. Myburg and F. D. Aurret, *Appl. Phys. Lett.* **61**(16), 1933 (1992).
11. G. Stareev, *Appl. Phys. Lett.* **62**(22) 2801 (1993).
12. E. D. Marshall and M. Murakami, in *Contacts to Semiconductors*, edited by L. J. Brillson (Noyes, Park Ridge NJ, 1993).
13. F. W. Ragay, M. R. Leys and J. H. Wolter, *Appl. Phys. Lett.* **63**(9), 1234 (1993).
14. H. K. Henisch, *Semiconductor Contacts*. (Clarendon Press, Oxford, 1984).
15. E. H. Rhoderick, *Metal-Semiconductor Contacts* (Oxford University Press, New York, 1988).
16. S. Kurtin, T. C. McGill and C. A. Mead, *Phys. Rev. Lett.* **22**(26), 1433 (1969).
17. J.S. Foresi, *Ohmic Contacts and Schottky Barriers on GaN*, M.S. Thesis, Boston University (1992).
18. J. S. Foresi and T. D. Moustakas, *Appl. Phys. Lett.* **62**(22), 2859 (1993).
19. B. L. Crowder and S. Zirinski, *IEEE Trans. Electron Devices* **ED-26**, 369 (1979).
20. S. P. Murarka, *Silicides for VLSI Applications*, Academic Press, New York (1983).
21. L. Krusin-Elbaum, J. Y.-C. Sun, and C.-Y. Ting, *IEEE Trans. Electron Devices* **ED-34**, 58 (1987).
22. J. C. Hensel, R. T. Tung, J. M. Poate, and F. C. Unterwald, *Appl. Phys. Lett.* **44**, 913 (1984); *Phys. Rev. Lett.* **54**, 1840 (1985).
23. P. H. Woerlee, P. M. Th. M. van Attekum, A. A. M. Hoeben, G. A. M. Hurkx, and R. A. M. Wolters, *Appl. Phys. Lett.* **44**, 876 (1984).
24. M. T. Huang, T. L. Martin, V. Malhotra, and J. E. Mahan, *J. Vac. Sci. Technol. B* **3**, 836 (1985).
25. L. Krusin-Elbaum and M. O. Aboelfotoh, *Appl. Phys. Lett.* **58**(12), 1341 (1991).
26. M. O. Aboelfotoh, H. M. Tawancy, and L. Krusin-Elbaum, *Appl. Phys. Lett.* **63**(12), 1622.
27. M. O. Aboelfotoh, K. N. Tu, F. Nava, and M. Michelini, *J. Appl. Phys.* **75**(1), (1994).
28. M. O. Aboelfotoh, H. M. Tawancy, *J. Appl. Phys.* **75**(4) (1994).
29. G. K. Reeves and H. B. Harrison, *IEEE Electron Device Lett.* **EDL-3** 111 (1982).
30. M. E. Lin, Z. Ma, F. Y. Huang, Z. F. Fan, L. H. Allen, and H. Morkoç, *Appl. Phys. Lett.* **64**(8), 1003 (1994).
31. C. R. Abernathy, S. J. Pearton, F. Ren, and P. W. Wisk, *J. Vac. Sci. Technol. B* **11**(2), 179 (1993).

XVIII. Reactive Ion Etching of GaN, AlN and InN

A. Introduction

Semiconductor devices are the principle components of electronic and telecommunications systems [1]. In order to densely pack these microscopic components, unidirectional, or anisotropic, etching techniques are required to produce a fine network of uniformly thick lines. Wet etching processes found in many semiconductor manufacturing steps produce a multi-directional, or isotropically, etched features with variable thickness through its depth. This is undesirable for microcircuitry since the goal is to produce the smallest devices possible. Therefore, plasma-assisted processes, such as reactive ion etching (RIE), combine the physical characteristics of sputtering with the chemical activity of reactive species to produce a highly directional feature. RIE has the added advantage of providing a more uniform etch and a higher degree of material etch selectivity.

RIE has been employed to etch a wide variety of semiconductor materials including silicon-based materials [2-11], metals, like aluminum [3, 12-18] and III-V compounds, such as GaAs and InP [19-21]. Plasma-assisted etching of newer III-V compounds, such as GaN, AlN and InN, has been conducted by several investigators [20-24]. There has been wide spread interest in using these nitrides for semiconductor device applications requiring visible light emission, high temperature operation and high electron velocities [21]. Since these materials possess wide bandgaps and optical emissions spectra in the blue to near ultraviolet range, they are prime candidates for ultraviolet detection devices.

The objectives of this report are to discuss recent progress made in the field of reactive ion etching of gallium, aluminum and indium nitride. In the following sections, a brief review of pertinent literature on plasma-assisted etching of gallium and aluminum compounds is provided along with a brief description of the reactive ion etching system and process gases.

B. Literature Review

Reactive Ion Etching of GaN. Since GaN is a direct transition material with a bandgap ranging from 3.4-6.2 eV at room temperature, it is an ideal candidate for the fabrication of shortwave length light emitters [21, 25]. High quality GaN films have been successfully grown by MOVPE [25], ECR-MBE [26, 27], MOCVD [28] and a layer-by-layer process [29] on a number of substrate. In order to fabricate complete device structures, reliable etching processes need to be developed. Since GaN is nearly inert to most wet etching solutions, with the exception of highly concentrated hot NaOH and H₂SO₄ [30], RIE may prove to be an effective method for the production of fine line patterning in semiconductor materials.

There have been a few reports of etching GaN by plasma-assisted processes [20-24]. Foresi [20] investigated fabrication techniques for ohmic contact and Schottky barriers on

GaN. One of the highlights of his work was the successful etching of GaN on sapphire substrate in Freon 12 (CCl_2F_2) and in hydrogen atmospheres operating at about 10 mTorr and 40 and 60 W of RF power. Results from SEM photographs showed that in the CCl_2F_2 plasma, GaN had been completely removed from areas that were not covered by photoresist, and that the sapphire substrate was nearly unetched. Foresi was able to obtain an etch rate of approximately 140 Å/min in the CCl_2F_2 plasma at 60 W, while the hydrogen plasma produced insignificant etching results. Etch selectivity between the GaN and photoresist was found to be 3:1. In another investigation, conducted by Tanaka *et al.* [21], reactive fast atom beam etching was employed to etch GaN on sapphire in a Cl_2 plasma at substrate temperatures ranging between 80-150°C. Etch rates of 1000-1200 Å/min produced relatively smooth surfaces and a well defined pattern of elongated rectangular bars on the sapphire substrate. More recently, S.J. Pearton *et al.* [22, 23] have produced smooth, anisotropically etched GaN and AlN in low pressure ECR discharges of BCl_3/Ar , $\text{CCl}_2\text{F}_2/\text{Ar}$ and $\text{CH}_4/\text{H}_2/\text{Ar}$. The etch rates of these nitrides were highly dependent on the DC bias voltage and ranges of 25-175 Å/min and 0-100 Å/min were reported for GaN and AlN, respectively. It is noted that hydrogen was added to the chlorine plasmas to facilitate removal of nitrogen from the surfaces of the nitride samples, thus producing smoother features. Also, Adesida *et al.* [24] employed reactive ion etching to produce 4000 Å thick lines in GaN with SiCl_4 plasmas. They found that the etch rate was independent of pressure but increased with self bias voltage. They obtained slightly overcut features with fairly smooth sidewalls at etch rates up to 500 Å/min. Experimental etching was also conducted with SiCl_4/Ar and $\text{SiCl}_4/\text{SiF}_4$, but the addition of Ar and F atoms to the plasma had no effect on the etch rate. In addition, residual Si and Cl were found on the GaN surfaces after etching.

Reactive Ion Etching of AlN. Aluminum nitride is a candidate material for optoelectronic devices because it possess a high electrical resistivity, high thermal conductivity, low dielectric constant and has a direct transition bandgap of 6.3 eV [31]. AlN films have been grown by several techniques including CVD, MBE and ALE, and on a variety of substrate materials including sapphire, silicon, spinel, silicon carbide and quartz [32]. Etching fine features in the AlN films is an important step in the fabrication of such devices. Though, only one report of etching of AlN is available in the open literature at this time [22], much work has been conducted on etching of metallic aluminum thin films [3, 12-18]. As a result, analogies to well established data for etching of aluminum are made. Although aluminum and AlN are very different materials, the chemistry and reactions in the plasma may be similar. So, it is proposed that reactive ion etching may also be an effective means for the application of fine line patterning of AlN.

A review of the literature shows that there are two primary methods employed for etching aluminum. Bruce and Malafsky [12] employed a parallel plate configuration (RIE) to

investigate the effects of Cl_2 on aluminum. They found that two processes are involved, namely, the removal of the oxide layer and etching the metal below it. For those experiments, it was hypothesized that BCl_3 gas was necessary for the removal of the oxide layer because it was responsible for the initiation of a reduction reaction with the oxide. In the RIE etching configuration, aluminum etched with a chlorinated gas is a purely chemical reaction with little contribution from ion bombardment. This conclusion was made as a result of the insensitivity of RF power to the etch rate [12]. Therefore, anisotropic etching was thought to have been the result of a sidewall passivation mechanism whereby a protective layer is formed on the vertical walls of the trench by reaction of H_2O or carbon containing species with the aluminum. Since ion bombardment is normal to the surface, the walls remained unetched. This mechanism was produced by the addition of CHCl_3 to the mixture of gases. Feature widths of $2.25\ \mu\text{m}$ were produced by a gas mixture of Cl_2 , BCl_3 , CHCl_3 and He at about 1.2 mTorr. Helium gas was added to the mixture to reduce the amount of erosion of the photoresist.

The combination of an isotropic flux of reactive species with a highly directional beam of energetic ions, so called ion beam assisted etching (IBAE), has been employed for the anisotropic etching of aluminum by many investigators [13-15, 18]. For IBAE, the aluminum oxide layer can be physical removed by sputtering with Ar^+ or Xe^+ ions, whereas with RIE the oxide is removed chemically [13]. However, etching takes place again by chemical reaction of Cl_2 with the aluminum as determined by the lack of dependence of the etch rate on the ion energy and current [14, 15]. From a mechanistic point of view, Cl_2 adsorbs onto and diffuses into the aluminum resulting in the formation of aluminum chlorides. Al_2Cl_6 is the dominant etch product at lower temperatures (33°C), while AlCl_3 was observed at higher temperatures (210°C) [15]. Saturation of the etched surface with chlorine atoms occurs prior to desorption of AlCl_3 .

The etch rate is dependent upon several parameters including the presence of residual gases in the chamber, substrate temperature, Cl_2 flux, ion beam and the presence of carbon containing species. Impurity gases in the chamber (i.e. H_2O , O_2 , N_2 , etc.) can react with the aluminum films and impede the etching process by leaving a residue on the etched surface. This reduces the amount of Cl_2 available for reaction and consequently lowers the etch rate [13]. The substrate temperature is another parameter that affects the etch rate of aluminum. Efremow *et al.* [12] observed a two-fold increase in the etch rate by heating the substrate from 0° to 100°C . It was hypothesized that the increase in temperature led to a higher evaporation rate of the product AlCl_3 . In addition, they found that an increase in the Cl_2 flux produced a significant amount of undercutting due to the nondirectional flow of the Cl_2 gas. A higher degree of anisotropy was achieved by the combination of ion beam and Cl_2 flux. Efremow *et al.* suggested that sidewall passivation (by reaction of H_2O with the aluminum)

was partly responsible for the production of the very fine features in their samples. Submicrostructures of 80 nm wide lines were etched into a 100 nm thick aluminum film with 0.3 mTorr Cl_2 gas and 0.1 mA, 1 keV Ar^+ beam. Lastly, Park *et al.* [14] found that chemisorption of the halocarbon gas molecules, such as CCl_4 and CBr_4 , onto the aluminum surface formed halogenated aluminum species along with an aluminum carbide. Therefore, a significant reduction in the etch rate was observed due to the difficulty encountered in removing the carbide from the surface.

C. Experimental Procedure

Experimental Apparatus. A schematic of the RIE system is shown in Figure 1. The main components of the system include gas handling/storage, etcher, gas scrubber and mass spectrometer. Since toxic gases, such as BCl_3 and Cl_2 , may be used to etch GaN and AlN, the system is designed for safe shutdown in the event of a power or water failure and/or inadvertent shutdown of the exhaust systems in the building.

The gas handling/storage sub-system consists of the gas storage cabinets, gas bottles, bottle regulators and necessary valves and tubing. Dry nitrogen is used to purge the gas lines before and after every run to remove moisture and chlorine from the lines, thus reducing the probability of corrosion of the gas lines. Mass flow controllers are employed for accurate control of the process gases. In the event of a power failure, interruption of the water supply

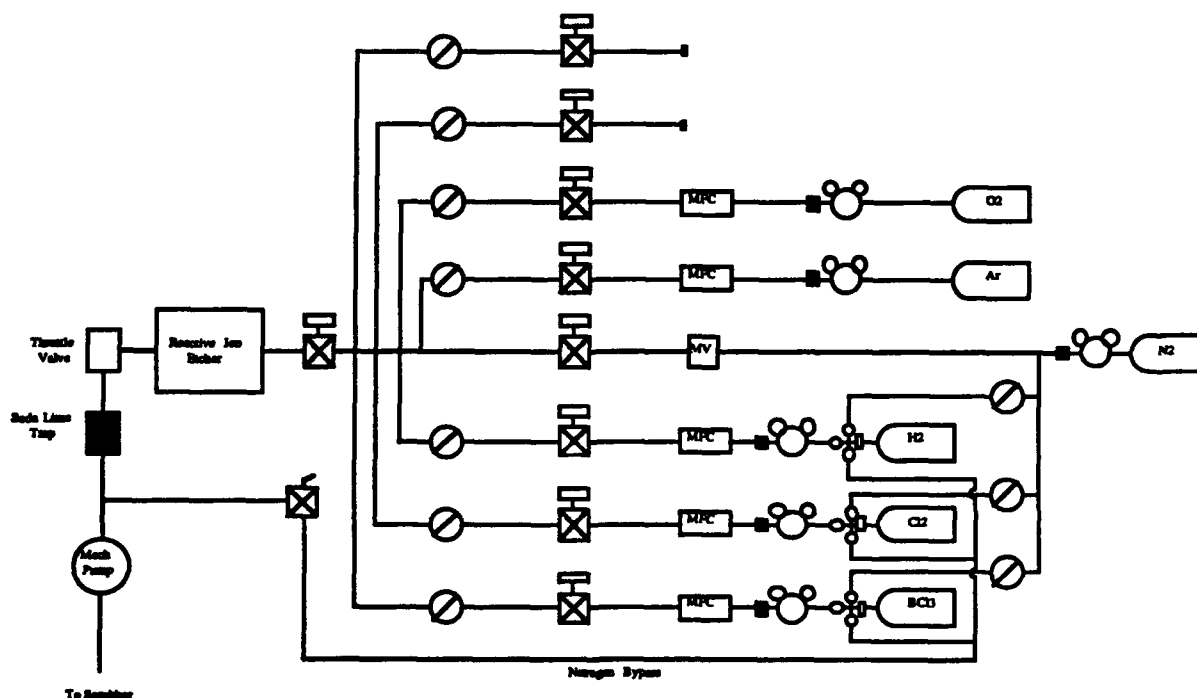


Figure 1. Reactive Ion Etching System

or shutdown of the exhaust system, the solenoid actuated pneumatic valves will isolate the gas lines from the etch chamber.

The design of the etcher is based on that of the standard parallel-plate diode configuration in which the bottom electrode is powered by a RF power supply (see for example Ref. [10]). The etcher, a Technics 85 series RIE, consists of an anodized aluminum chamber with an anodized aluminum water-cooled, driven lower electrode. A 350 Watt, 13.56 MHz RF generator with auto impedance matching network produces the power required to maintain a glow discharge in the chamber. Safety interlocks are supplied by Technics to disable the power when the system is vented or a panel is removed. The chamber pressure is measured by a corrosion-resistant capacitance manometer (absolute pressure) which is mounted to the underside of the chamber. The six channels of process gas (made from stainless steel tubing) are isolated from the injection manifold by means of air-operated electrically actuated isolation valves. In addition, an 11 CFM two-stage corrosive-series direct drive rotary vane pump is supplied with the etcher.

Residual process gases and reaction by-products from the etcher will pass through a soda lime trap and a wet scrubber, which is equipped with a water recirculation line. These lines are monitored for water flow and exhaust ventilation and are an integral part of the control system. Interruption of the water flow or inadequate ventilation will trip the pneumatic valves and close the gas lines. In addition, the pH level of the scrubber water is tested and monitored prior to each days etching runs.

Finally, a mass spectrometer may be employed in the future for the detection and characterization of chemical species produced by the etching processes. It could also be used as a means for end-point detection. It is further hoped that this analytical instrumentation could provide a basis for an understanding of the etching mechanisms.

Choice of Process Gases. There are a number of process gases that can be used to produce anisotropically etched features. For GaN, AlN and InN, fluorine plasmas are impractical because involatile fluorides are formed with Ga and Al at the surfaces, therefore limiting desorption of reaction species from the surface [33]. Chlorine plasmas, on the other hand, have been used extensively for etching these compounds, see Section B above.

Based on the success of Pearton *et al.* [22, 23] and others [20, 21, 24] Cl_2 and BCl_3 are currently being used to etch GaN. Experimentation with other combinations of gases, such as iodine- and/or bromine-containing gas mixtures) is possible in order to obtain smooth, anisotropic features with reasonably high etch rates. As for AlN, chlorine containing gases with additions of O_2 , carbon containing gases and or noble gases (i.e. Ar, He, etc.) are likely to be chosen as RIE process gases. It is noted that for RIE, sidewall passivation may be an important mechanism for anisotropic etching of AlN and may produce relatively large features.

Etching Procedure. Prior to etching, the nitride samples are RCA cleaned and subsequently dipped in 10% HF/90% H₂O for 2-5 minutes to remove any residual contamination. Photoresist is spun onto the samples, hard baked, masked and developed to produce the desired patterns. The RIE system is checked for proper water, air and exhaust supply. Samples are loaded into the etching chamber and process gas lines are pumped down to 5×10^{-4} torr. A typical etch run includes the following steps:

1. Oxygen plasma to remove water vapor and contamination from the etch chamber;
2. Nitrogen purge to remove oxygen from etcher;
3. Cl₂ or BCl₃ plasma for processing;
4. Nitrogen purge to remove chlorinated process gases from the chamber;
5. Vent chamber to atmosphere with nitrogen.

After the samples are removed from the etcher, the photoresist is removed in acetone and the step heights are measured with a Dektak stylus profilometer. In addition, SEM is used to observe the surface roughness and etched steps, and XPS and AES are used to observe the residual gas species on the sample surface.

D. Results

GaN has been etched in Cl₂ and BCl₃ plasmas with varying flow rates, pressures, power and DC bias. Typical etching parameters are: 1-10 sccm total gas flow, 35-75 mtorr, 125-200 W power and -(200-300)V bias. Etch rates of up to 180 Å/min and 150 Å/min have been achieved with Cl₂ and BCl₃ plasmas, respectively.

E. Future Research

In the immediate future, complete parametric studies will be conducted to determine how the power, pressure, gas load and flow rates affect the etching rate of these nitrides in BCl₃/Ar and Cl₂/Ar plasmas. Alternative Cl-containing gases such as methyl and nitrosyl chloride may be used in the future in order to establish etch rates of the nitrides and to study the underlying etch mechanisms. Surface analysis techniques such as AES and XPS will be employed to determine the contamination levels and surface condition of the nitrides before and after etching. In addition, experimentation with different cathode materials (such as graphite and quartz) is possible if there is any micromasking from the cathode material.

F. References

1. *Plasma Processing of Materials: Scientific Opportunities and Technological Challenges*, National Research Council - Panel on Plasma Processing of Materials, Eds. (National Academy Press, Washington, D.C., 1991).
2. J. W. Palmour, R. F. Davis, T. M. Wallett, K.B. Bhasin, J. Vac. Sci. Technol. A 4, 590 (1986).
3. D. L. Smith, P. G. Saviano, J. Vac. Sci. Technol. 21, 768 (1982).

4. D. L. Smith, R. H. Bruce, J. Electrochem. Soc. 129, 2045 (1978).
5. C. J. Mogab, A. C. Adams, D. L. Flamm, J. Appl. Phys. 49, 3796 (1978).
6. S. Matsuo, J. Vac. Sci. Technol. 17, 587 (1980).
7. L. M. Ephrath, Solid State Technol., (July 1982), 87.
8. Y. H. Lee, M. M. Chen, J. Appl. Phys. 54, 5966 (1983).
9. L. M. Ephrath, J. Electrochem. Soc., (August 1979), 1419.
10. A. J. van Roosmalen, Vacuum 34, 429 (1984).
11. M. Zhang, J. Z. Li, I. Adesida, E.D. Wolf, J. Vac. Sci. Technol. B 1, 1037 (1983).
12. R. H. Bruce, G. P. Malafsky, J. Electrochem. Soc. 136, 1369 (1983).
13. N. N. Efremow, M. W. Geis, R. W. Mountain, G.A. Lincoln, J.N. Randall, N.P. Economou, J. Vac. Sci. Technol. B 4, 337 (1986).
14. S. Park, L. C. Rathburn, T. N. Rhodin, J. Vac. Sci. Technol. A 3, 791 (1985).
15. H. F. Winters, J. Vac. Sci. Technol. B 3, 9 (1985).
16. D. A. Danner, D. W. Hess, J. Appl. Phys. 59, 940 (1986).
17. R. J. A. A. Janssen, A. W. Kolfchoten, G. N. A. van Veen, Appl. Phys. Lett. 52, 98 (1988).
18. Y. Ochiai, K. Shihoyama, T. Shiokawa, K. Toyoda, A. Masuyama, K. Gama, J. Appl. Phys. 25, L527 (1986).
19. G. Smolinski, R. P. Chang, T. M. Mayer, J. Vac. Sci. Technol. 18, 12 (1981).
20. J. S. Foresi, M.S. Thesis, Boston University, Boston, MA, 1992.
21. H. Tanaka, Optoelectron. Dev. Technol. 6, 150 (1991).
22. S. J. Pearton, C. R. Abernathy, F. Ren, J.R. Lothian, P.W. Wisk, A. Katz, Semiconductor Sci. Technol. 8, 310 (1993).
23. S. J. Pearton, C. R. Abernathy, F. Ren, J.R. Lothian, P.W. Wisk, A. Katz, J. Vac. Sci. Technol. A 11, 1772 (1993).
24. I. Adesida, A. Mahajan, Appl. Phys. Lett. 63, 2777 (1993).
25. I. Akasaki, H. Amano, Physica B 185, 428 (1992).
26. C. Eddy, Ph.D. Thesis, Boston University, Boston, MA, 1990.
27. T. Lei, T. D. Moustakis, J. Appl. Phys. 71, 4933 (1992).
28. Z. J. Yu, B. S. Sywe, A. U. Ahmed, J.H. Edgar, J. Electr. Mater. 21, 782 (1992).
29. J. Sumakeris, Z. Sitar, K. S. Ailey-Trent, Thin Solid Films 225, 244 (1993).
30. CRC Handbook of Metal Etchants, Editor, Eds. (CRC Press, Boca Raton, LA, 1991).
31. E. S. Dettmer, B. M. Romenesko, H. K. Charles, B.G. Carkhuff, D.J. Merrill, IEEE Trans. Comp. Hybrids Manuf. Technol. 12, 543 (1989).
32. L. R. Rowland, Ph.D. Thesis, North Carolina State University, Raleigh, NC, 1992.
33. V. M. Donnelly, D. L. Flamm, Solid State Technol., (April 1981), 161.

XIV. Growth System for the Metalorganic Chemical Vapor Deposition of InN and InGaN Solid Solutions for Optical Semiconductor Device Applications

A. Introduction

InN and InGaN compounds have potential for applications in optical semiconductor devices. With band-gap energies of 1.9 and 3.4 eV for InN and GaN, respectively, devices can be made covering the blue and blue-green light emission ranges. Work had been done in making blue LED devices using a double-heterostructure architecture, among others. Nakamura *et al.* report an output power of 124 μW and a quantum efficiency of 0.22% with a peak wavelength of 440 nm for their device [1]. Other works have reported film growth, although characterization of the films has been limited [2-4]. The main problem with growing the InGaN films has been the indium incorporation, due to the high equilibrium vapor pressure of nitrogen over InN, which is several orders of magnitude higher than either GaN or AlN. At low processing temperatures, epitaxial InGaN compounds have been grown successfully, although film quality and optical properties have been poor. At higher processing temperatures film quality is good and optical properties improve, however, the incorporation efficiency of indium goes down as shown in Fig. 1. As a result, typical high temperature processing ($>800^\circ\text{C}$) requires high ammonia flow rates and V/III ratios as large as 20,000 [2,3]. Compositional control in InGaN films has only been achieved for relatively low growth temperatures, up to 650°C [2].

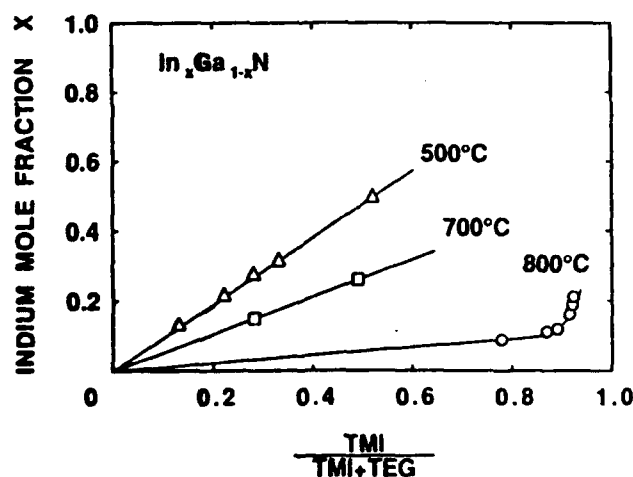
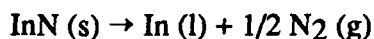


Figure 1. Relation between indium mole fraction of InGaN and the flow ratio of indium source to the sum of group III sources [3].

It has been shown that InN undergoes the following decomposition:



Other work has shown decomposition starts as low as 350°C [5,6]. As a result, it is easy to see why at higher temperatures the growth of InN films becomes difficult and why the indium incorporation in InGaN films decreases. As higher processing temperatures are required for better optical properties, a processing technique addressing the problems of the InN/InGaN system is needed. In this paper we introduce a chemical vapor deposition system in which the thin film growth problems are addressed.

B. Experimental Procedure

Figure 2 shows a schematic of the CVD system we will use to grow the films. The design is a vertical cold wall reactor with metalorganic source gases. Using nitrogen as a carrier gas, the source gases and dopants enter a radial manifold where they mix and enter the reactor. Unlike conventional systems the source gases will enter at the bottom of the reactor and flow

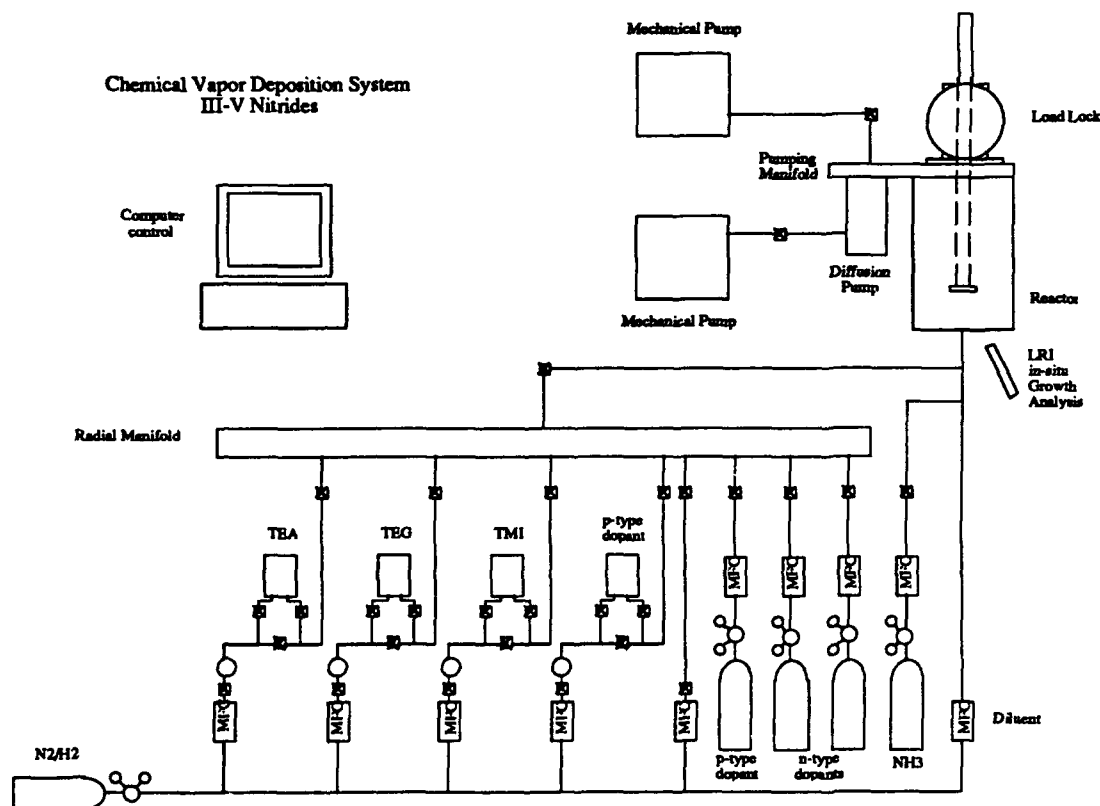


Figure 2: Chemical Vapor Deposition System Schematic.

to the top. The source gases react with ammonia in the reactor on a resistance heated rotating substrate perpendicular to the flow direction. Excess hydrogen or nitrogen act as diluents in the reactor. The entire system will be computer controlled with an computer. This will allow for abrupt interfaces and good control in growing complex devices. InN and InGaN compounds will be grown on different substrates, including SiC and sapphire, at various temperatures and compositions. As mentioned before, previous work has shown that high V/III ratios and large flow rates are required to grow quality films. In addition to varying the flow rates and ratios, the pressure of the system can be varied up to approximately 2500 torr. This will allow us to investigate the effects of processing pressure on the film quality.

Laser Reflection Interferometry (LRI) will be used for *in-situ* monitoring of film growth. This measurement technique involves detecting a laser beam reflected off the surface of the sample. As the film grows, the superpositioning of two light waves reflected from the surface of the film and the film-substrate interface generate a periodic interference pattern which corresponds to the thickness of the film, depending on the wavelength and incident angle of the light, and the index of refraction of the material. From this technique, growth rate and film thickness can be measured [7, 8].

A target composition for the nitride compound is $\text{In}_{0.2}\text{Ga}_{0.8}\text{N}$ which corresponds to an emittance wavelength of 470 nm (bandgap of 2.64 eV), the wavelength used in blue LEDs for flat panel displays [3]. Figure 3 shows a representation of one of the device structures we will investigate in making an LED device. The structure is a p-GaN/n-InGaN/n-GaN double heterostructure LED. It will be grown on a SiC substrate with an AlN buffer layer. The n- and p-type dopants are Si and Mg, respectively. This and other devices will be investigated once film growth in the system has been characterized.

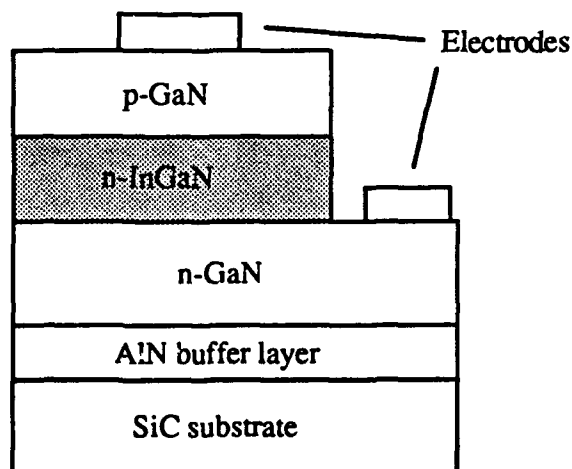


Figure 3. Structure of the DH blue LED (After [1]).

C. Discussion

The choice of reactor design comes from investigating the transport phenomena in the CVD process. The reactor geometry has considerable impact of the flow structure and by appropriately designing the reactor it is possible to minimize the detrimental flow characteristics of vertical cold wall CVD systems. Examining several of the factors governing the transport phenomena in CVD we can see why an inverted geometry design lends itself to the InN/InGaN system.

Thermal Effects and Flow Patterns. Complex flow structures develop in CVD reactors due to large thermal gradients between the heated substrate and the cold walls. This leads to buoyancy-driven secondary flows superimposed on the forced flow of gases entering the reactor. Recirculation cells form above the suceptor in conventional flow reactors as result of these recirculations [9]. This effect can be controlled using high inlet flow rates, but there are limits to how close the inlet can be to the heated substrate without unwanted decomposition or predeposition in the inlet. However close the inlet is to the substrate, there will be a sudden increase in cross-sectional area as the gases enter the reactor, resulting in a decrease in linear flow velocity. This increases the potential for buoyancy-driven recirculation. Inverting the reactor so the buoyancy and inlet flow directions are aligned eliminates the major cause of thermal convections [10]. Radial temperature gradients may still drive flows, but with good temperature uniformity across the substrate this effect can be reduced. With an inverted geometry the flow from the gas inlet to the suceptor becomes controlled by the inlet flow rate which improves film thickness uniformity.

Suceptor Rotation. A rotating suceptor is often used in CVD systems to produce more uniform films. Rotation of the suceptor at high speeds emulates a rotating-disk flow which is advantageous in creating a uniform mass-transfer layer. As a result, the film thickness and growth rate are increased. The suceptor rotation also stabilizes the flow through the reactor by assisting the forced flow [9].

System Pressure. To obtain uniform deposition and abrupt interfaces CVD systems are often operated at reduced pressure with high flow rates. This is a result of a need to decrease the residence time of the reaction gases in the reactor. In conventional systems, residence time increases with increasing pressure as thermally driven convection flows increase [10]. With an inverted geometry the recirculation effect is virtually eliminated due to the alignment of the buoyancy and flow directions, allowing for the operation of the reactor at higher pressures without flow deterioration at higher pressures. This, combined with a rotating suceptor, should allow forced flow conditions at higher pressures than allowed by conventional systems. This is especially pertinent in the InN system, where the equilibrium vapor pressure of nitrogen is high. Using a higher pressure of nitrogen in the system we should be able to better control the decomposition of the InN films at higher temperatures.

We will be able to investigate the effect of an increased system pressure on the growth of single crystal InN films at higher temperatures without having to compensate for decreased flow stability.

Junctions/Interfaces. Abrupt junctions and interfaces are necessary in producing complex devices for optoelectronics applications. As mentioned above, good interfaces require abrupt changes in gas sources, which depends on the gas residence time in the reactor. With the inverted geometry, residence times can be decreased, even at increased pressures. Computer control will also give good timing precision.

D. Future Research Plans and Goals

The system described in this report is currently being built and assembled. Once assembled, preliminary work will involve characterizing the growth of InN and GaN films in the system and achieving a level of reproducibility. A study we plan to perform is a series of InN film growths at a set temperature over a range of pressures. Once the growth of these films is characterized, growth of the $\text{In}_x\text{Ga}_{1-x}\text{N}$ alloys will lead to the development of optical devices.

E. References

1. S. Nakamura, M. Senoh, T. Mukai: Jpn. J. Appl. Phys. **31** L8 (1993).
2. N. Yoshimoto, T. Matsuoka, T. Sasaki, A. Katsui: Appl. Phys. Lett. **59** 2251 (1991).
3. T. Matsuoka, N. Yoshimoto, T. Sasaki, A. Katsui: J. Elect. Matls. **21** 157 (1992).
4. T. Nagatomo, T. Kuboyama, H. Minamino, O. Omoto: Jpn. J. Appl. Phys: **28** L1334 (1989).
5. Q. Guo, O. Kato: J. Appl. Phys. **73** 7969 (1993).
6. R. Jones, K. Rose: J. Phys. Chem. Solids. **48** 587 (1987).
7. B. R. Stoner, B. E. Williams, S. D. Wolter, K. Nishamura, and J. T. Glass. J. Mater. Res., **7**(2), (1992).
8. Ching-Hsong Wu, W. H. Weber, T. J. Potter, and M. A. Tamor. J. Appl. Phys. **73**(6) 15 March 1993.
9. Jensen, K. *Microelectronics Processing: Chemical Engineering Aspects*; American Chemical Society; Washington, DC; 1989; p. 199.
10. K. Jensen, E. O. Einset and D. I. Fotiadis, *Annual Review of Fluid Mechanics*; Annual Reviews Inc.; Palo Alto, CA; 1991; p. 197.

Phosphorous-based Materials

XV. Determination of Excess Phosphorous in Low-Temperature GaP Grown by Gas Source Molecular Beam Epitaxy

A. Introduction

GaAs grown at a low temperature (LT) of $\sim 200^\circ\text{C}$ by molecular beam epitaxy (MBE) and then annealed at high temperatures has been found to be semi-insulating. It exhibited several applications in GaAs devices.[1,2] The most important structural characteristic of this material is the excess arsenic on the order of 1 at.% incorporated during the LT growth[3]. Recently, the preliminary studies on LT GaP also revealed the presence of excess phosphorus in the epilayers, as indicated by transmission electron microscopy (TEM) and x-ray analyses.[4] One of the differences between LT GaAs and LT GaP is that high temperature annealing is required for the former material to become semi-insulating while it is not necessary for the latter material, where both as-grown and annealed samples exhibited semi-insulating properties. The semi-insulating nature of LT GaP was proposed to be mainly a result of excess-phosphorus-related deep levels.[4] In this report, we will discuss the quantitative determination of the nonstoichiometry of LT GaP grown at $\sim 200^\circ\text{C}$. Several characterization techniques were used such as analytical scanning transmission electron microscopy (STEM), double-crystal x-ray diffraction (DCXRD), particle-induced x-ray emission (PIXE), and Raman scattering measurements.

B. Experimental Procedure

LT GaP epilayers were grown using a Riber 32RD gas source molecular beam epitaxy (GSMBE) system. Solid Ga and 100% PH_3 precracked at 950°C were used as III-V sources. The growth rate was $1\ \mu\text{m/h}$ and all the samples used in this work had a mirror-like morphology. GaP substrate is used as a reference for all characterizations in this work. More detailed experimental conditions were reported earlier[4].

Analytical STEM technique was used to determine the excess phosphorus in the LT GaP films. The analysis was performed in a TOPCON EM-002B ultra-high resolution analytical electron microscope equipped with an electron probe. The TEM facility was operated at 120 KV with the probe diameter set at 4.9 nm throughout the analysis. The nonstoichiometry of the LT material was also evaluated using PIXE technique in University of California at Berkeley. The measurements were performed by employing a 0.5 MeV H^+ beam with samples tilted at 65° with respect to the ion beam. Raman scattering measurements were carried out in backscatter configuration at room temperature using the 514.5 nm line of an Ar^+ ion laser. The laser power was 250 mW, and the spot size was $\sim 2\ \text{mm} \times 80\ \mu\text{m}$ obtained using a cylindrical lens. The signal was detected with a photomultiplier tube operated in photon counting mode. The spectrometer slits were set to $80\ \mu\text{m}$ corresponding to a

resolution of $\sim 0.4 \text{ cm}^{-1}$. Both laser power and laser spot size were kept constant from run to run for the consistency of the experiment.

C. Results and Discussion

The cross sectional TEM samples used in this work were prepared in such a way that each sample includes a substrate piece serving as a reference for the material of interest. Excess phosphorus in LT GaP films were determined by using the analytical STEM technique. This technique measures phosphorus and gallium x-ray signals, the K_{α} signals of which are used to get the $[P]/[Ga]$ atomic ratio. The excess phosphorous concentration in the material can then be calculated using this ratio. The excess phosphorus is defined as $([P]-[Ga])/([P]+[Ga])$ similar to the calculation of excess arsenic in LT GaAs[5]. In order for the analysis to be statistically accurate, about ten data points were taken by setting the electron probe at different locations within the same layer. The values of the atomic ratios thus obtained were then numerically averaged, and this averaged atomic ratio would be used for the excess phosphorus calculation. As an example, the LT film grown at 190°C showed the $[P]/[Ga]$ atomic ratios ranging from 1.0189 to 1.0346. The average atomic ratio is 1.0243, which is equivalent to an excess phosphorus amount of 1.20 at.%. It must be noted that the average atomic ratio of a LT film is normalized by that of the substrate. With the same approach, the STEM analyses on the LT films grown at 180 and 200°C yielded 1.47 and 0.73 at.% excess phosphorus, respectively.

DCXRD analyses revealed that the excess phosphorus atoms incorporated into LT GaP caused a lattice expansion with respect to bulk GaP. The lattice expansion is manifested as a Bragg angle splitting with epilayer reflection peak located at a lower angle relative to the substrate peak. Hence, in principle, the Bragg angle splitting of an as-grown LT GaP can be related to the quantity of excess phosphorus in the lattice. Shown in Fig. 1 is a typical rocking curve of (113) reflections obtained on the unannealed sample grown at 180°C . The epilayer peak at lower Bragg angle position has a splitting of 220 arc sec from the substrate peak. For the simplicity of the excess phosphorus calculation from the splitting, two assumptions have been made. Firstly, the lattice is assumed uniformly and elastically expanded, that is, the LT GaP still has a cubic lattice. This assumption, although not exact, can be considered as an approximation. Secondly, the excess phosphorus are incorporated as misfitting particles (both as interstitials and antisites). Let ϵ be the elastic strain of the LT GaP lattice induced by the incorporation of the excess phosphorus in the lattice, and δ the net lattice mismatch (strain effect corrected) between the LT GaP and bulk GaP lattices. Then, the two parameters ϵ and δ can be related by the Bullough and Newman equation:

$$\epsilon = \frac{\delta (1 + \nu)}{3 (1 - \nu)}, \quad (1)$$

where ν is Poisson's ratio[6]. Note that ν is about 1/3 for almost all III-V semiconductors. Therefore, the ϵ - δ relation can be simplified as

$$\epsilon \approx \frac{2}{3} \delta. \quad (2)$$

Now, let δ_m denote the measured lattice mismatch (strain effect included) between the LT GaP and bulk GaP lattices. In theory, it is composed of the elastic strain and net lattice mismatch, i.e.,

$$\delta_m = \epsilon + \delta. \quad (3)$$

Substituting eq.(2) into eq.(3), and solving for δ gives the following approximate relation between δ and δ_m :

$$\delta \approx \frac{3}{5} \delta_m. \quad (4)$$

Let a_e be the lattice constant of LT GaP for which the elastic strain effect is corrected according to eq.(4) and, a_s the lattice constant of bulk GaP. Then the net volume increase of a unit cell of the LT GaP lattice can be calculated by $\Delta V = a_e^3 - a_s^3$. Considering phosphorus atom as a hard sphere with a radius of 1.23 Å,[7] and that there are four phosphorus atoms in a unit cell of a stoichiometric GaP, one can now calculate the percentage of excess phosphorus incorporated in ΔV . Such calculation yielded 1.89 at.% excess phosphorus in the film grown at 180°C. DCXRD also showed that the films grown at 190 and 200°C had

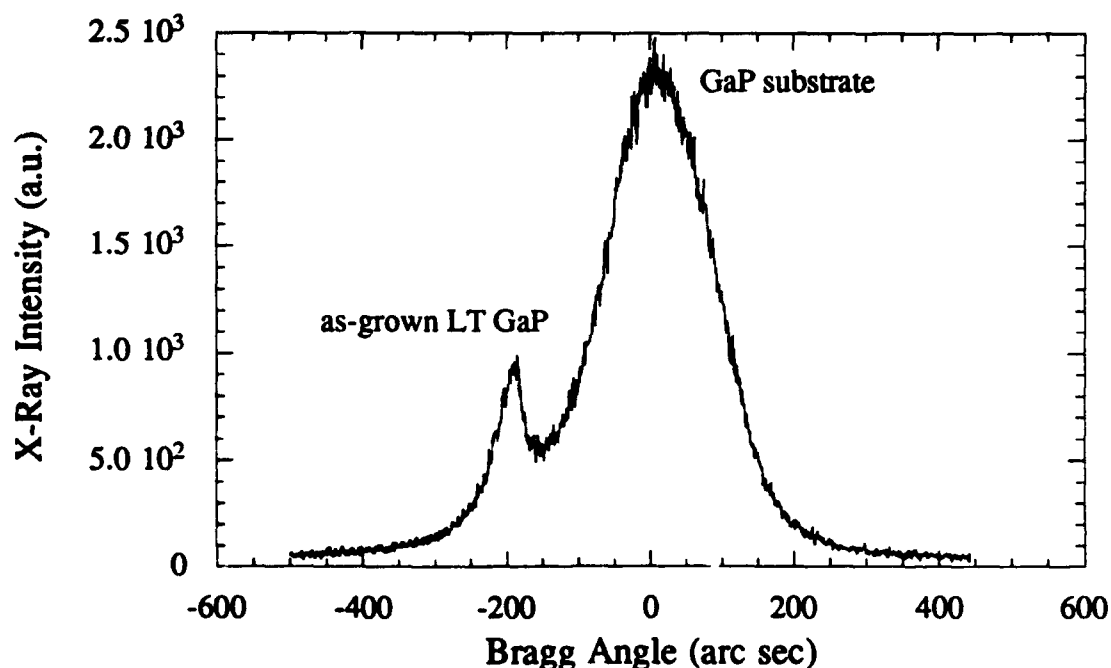


Figure 1. Double-crystal x-ray diffraction from (113) reflection planes of the unannealed LT GaP sample grown at 180°C.

splittings of -230 and -70 arc sec, respectively. The amounts of excess phosphorus causing the splittings were calculated to be 1.97 and 0.60 at.%, respectively. As expected, this approach of nonstoichiometry determination using DCXRD is convenient and it gives a relatively reasonable estimation.

The PIXE technique also measures the $[P]/[Ga]$ atomic ratios using K_{α} x-rays. The overall statistical error of this technique on the measurement of the atomic ratios was estimated to be about 0.4%. A $[P]/[Ga]$ ratio of 1.025 was obtained for the LT GaP film grown at 190°C, indicating the excess phosphorus of 1.23 at.%. This value is in good agreement with that obtained from the same sample by STEM technique. The PIXE measurements made on the LT film grown at lower temperature of ~160°C yielded a $[P]/[Ga]$ ratio of 1.045, corresponding to the excess phosphorus of 2.2 at.%. Shown in Fig. 2 is the superimposed P(K_{α}) x-ray signals of that sample (top) and GaP substrate (bottom). Both spectra were obtained under identical conditions. The intensity difference of the two spectra shown in Fig. 2 indicates a higher phosphorus content in the LT GaP sample. The Ga(K_{α}) x-ray signals of the sample and the substrate were totally overlapped and thus not shown here. Note that this sample showed high dislocation density by TEM, but was still crystalline as determined by electron diffraction pattern.

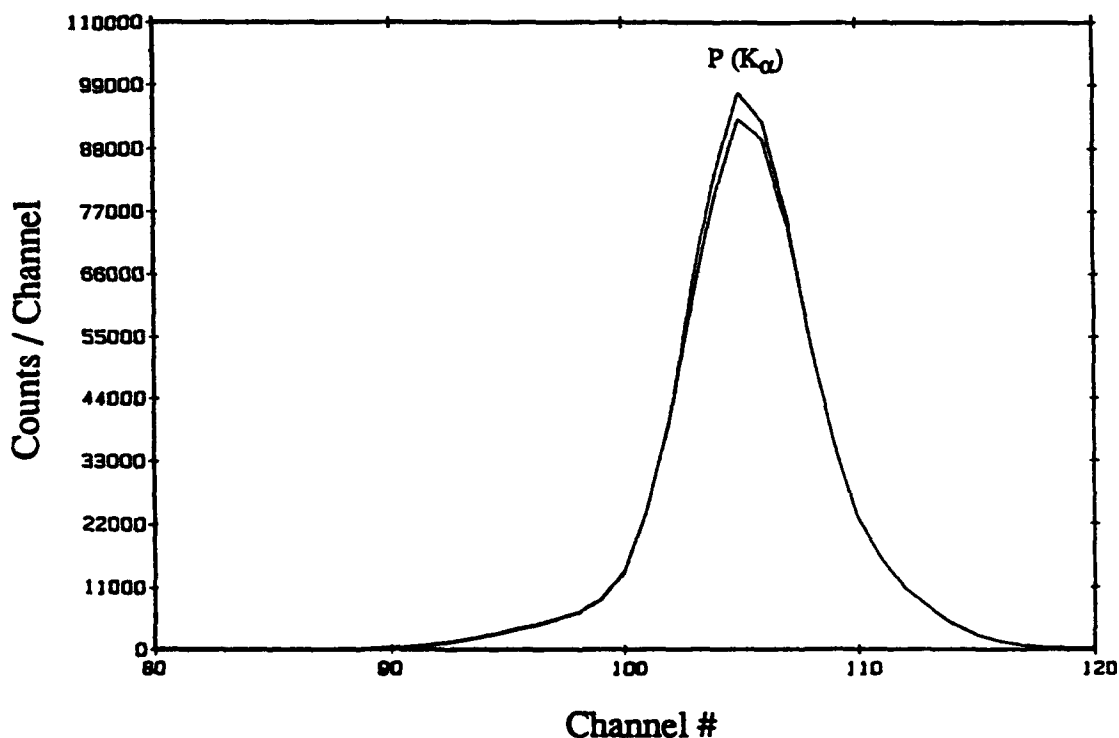


Figure 2. 0.5 MeV H^+ PIXE superimposed P(K_{α}) x-ray signals from the as-grown LT GaP epilayer grown at ~160°C (top) and GaP substrate (bottom). Note that the difference in intensity of the two spectra indicates a higher excess phosphorus content in the LT GaP epilayer.

Raman scattering measurements were performed on the as-grown, annealed LT GaP, and bulk GaP under identical conditions. Shown in Fig. 3 are the Raman spectra of the as-grown, annealed (at 700°C for 1 hr) LT GaP, and bulk GaP. The TO phonons of the three samples have much weaker intensities since they are not allowed in the (100) orientation. More significantly, they do not show any substantial frequency shift. The LO phonons of the as-grown sample, however, shift down in frequency from the bulk material by 2.2 cm⁻¹. The frequency of the annealed sample showed a small shift from that of the as-grown sample within margin of the resolution error, indicating a negligible effect of annealing on the frequency. The peak frequencies for the spectra in Fig. 3 are listed in Table I. The LO phonon frequency downshift or the reduction of LO-TO splitting of the as-grown LT GaP with respect to that of the bulk GaP may mainly be a result of the reduction in the effective charge

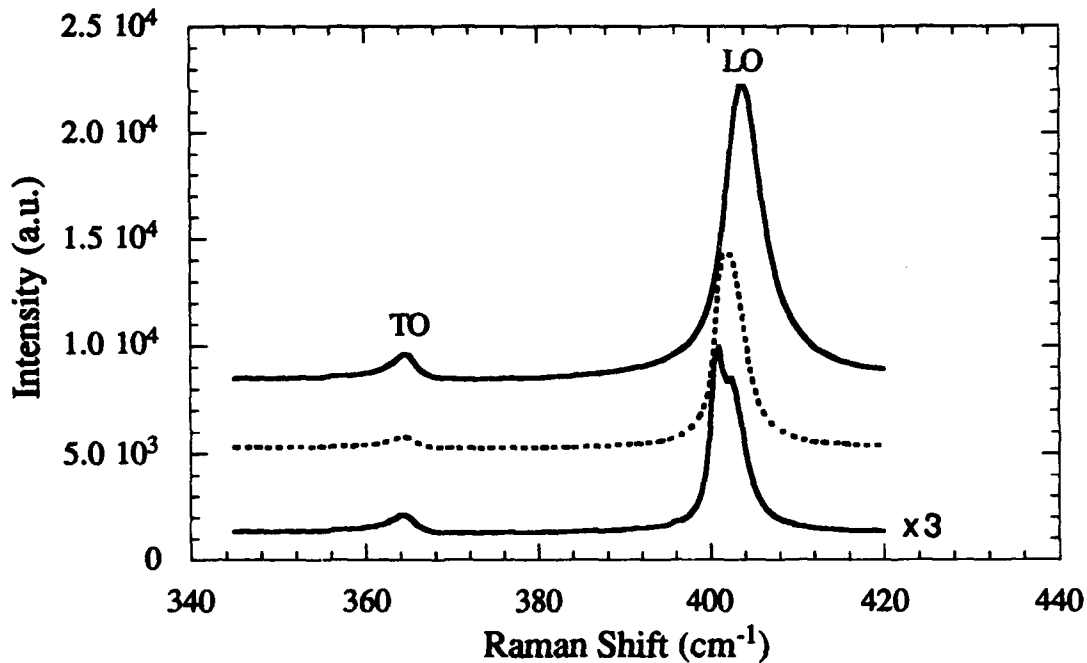


Figure 3. Raman spectra of: bulk GaP (top), annealed LT GaP (middle), and as-grown LT GaP (bottom).

for P_{Ga} antisite defects by analogy with the similar study of LT GaAs.[8] Hence, the excess phosphorus incorporated in LT GaP as antisites can be correlated to the LO-TO splitting. The calculation equation was established simply by following the similar approach proposed for LT GaAs.[8] Let x denote a fraction of P substituting Ga, implying a nonstoichiometry of Ga_{1-x}P_{1+x}, $\mu(x)$ the average value of the reduced mass of the unit cell due to the fraction x of P_{Ga} antisites and, $q(x)$ the average value of the effective charge on the ions. Then we have

$$\mu(x) = (1 - 0.3848x) \mu_{\text{GaP}} \quad (5)$$

with the values 69.72 and 30.97376 amu for the masses of Ga and P, respectively, and

$$q(x) = (1-x) q_{\text{GaP}}. \quad (6)$$

Therefore, the LO-TO splitting as a function of x can be expressed as

$$\frac{[\omega_L^2 - \omega_T^2]_{\text{Ga}_{1-x}\text{P}_{1+x}}}{[\omega_L^2 - \omega_T^2]_{\text{GaP}}} = \frac{(1-x)^2}{(1-0.3848x)}, \quad (7)$$

where ω_L and ω_T are the LO and TO phonon frequencies, respectively.

Table I. LO and TO phonon peak frequencies of the Raman spectra in Fig. 3. The resolution of these measurements is about $\pm 0.4 \text{ cm}^{-1}$.

Sample	TO frequency	LO frequency
Bulk GaP	364.8	403.8
Annealed LT GaP	364.6	402.0
As-grown LT GaP	364.4	401.6

Substituting the frequencies listed in Table I for the as-grown LT GaP and bulk GaP samples into the above equation and solving for x , we get $x \sim 0.03$. Note that the resolution of the Raman measurements on phonon frequencies is about $\pm 0.4 \text{ cm}^{-1}$ and this error in frequency can produce an error of approximately ± 0.01 in x . The value of x is fairly close to those results obtained from STEM and PIXE if the lower limit is considered.

TABLE II. Excess phosphorus in LT GaP grown at various temperatures. The values of stoichiometry were determined by STEM and DCXRD techniques.

T_s (°C)	STEM (at.%)	DCXRD (at.%)
180	1.47	1.89
190	1.20	1.97
200	0.73	0.60

D. Conclusions

In conclusion, LT GaP films grown at 180-200°C by GSMBE exhibit a quantity of excess phosphorus ranging from ~ 0.6 to 2 at.%. The results of the excess phosphorus determined by the different approaches discussed above (namely, STEM, DCXRD, PIXE and Raman

scattering) are in general agreement. To compare values of excess phosphorus vs growth temperature, the results determined by STEM and DCXRD from the samples grown in the aforementioned temperature range are tabulated in Table II. As a whole, the quantity of excess phosphorus appeared to vary inversely with growth temperature. At this point, a question may be raised about how the excess phosphorus are incorporated in the crystal lattice. Raman measurements showed the reduction of LO-TO splitting for the as-grown LT GaP, implying the existence of P_{Ga} antisite defects. DCXRD indicated a lattice expansion, suggesting that the excess phosphorus may be incorporated also as interstitials. Since x-ray measures the change in lattice constant, which may be caused by both interstitials and antisites, we conclude that both defects exist in the lattice at this time. More work needs to be done for the quantitative determination of each type of defects.

E. Future Research Plans

For a complete nonstoichiometric analysis of LT GaP, further investigation is needed about where these excess phosphorus are and how annealing that, we know, causes some segregations can affect these results.

GaP has several promising properties for device applications. These properties include a wide bandgap of 2.27 eV at room temperature, a high Schottky barrier of 1.3 eV for Au/GaP, and no surface Fermi level pinning. Now that LT GaP has been observed to have semi-insulating nature, its strained film may be used as a passivating layer in GaAs MESFETs to improve the gate-drain breakdown voltage of the device. Therefore, a lot of work is required for further characterization of the device application of LT GaP. In addition, the critical layer thickness (CLT) of LT GaP on GaAs also needs to be determined so that the strained layer thickness can be controlled within its CLT to avoid the degradation of the device performance by the generation of misfit dislocation defects.

F. References

1. F. W. Smith, A. R. Calawa, C.-L. Chen, M. J. Manfra, and L. J. Mahoney, *IEEE Electron Device Lett.* **9**, 77 (1988).
2. L.-W. Yin, Y. Hwang, J. H. Lee, R. M. Kolbas, R. J. Trew, and U. K. Mishra, *IEEE Electron Device Lett.* **11**, 561 (1990).
3. M. Kaminska, E. R. Weber, Z. Liliental-Weber, R. Leon, and Z. U. Rek, *J. Vac. Sci. Technol. B* **7**, 710 (1989).
4. J. Ramdani, Y. He, M. Leonard, N. El-Masry, and S. M. Bedair, *Appl. Phys. Lett.* **61**, 1646 (1992).
5. Z. Liliental-Weber, W. Swider, K. M. Yu, J. Kortright, F. W. Smith, and A. R. Calawa, *Appl. Phys. Lett.* **58**, 2153 (1991).
6. R. Bullough and R. C. Newman, *Rep. Prog. Phys.* **33**, 101 (1970).
7. *Table of Periodic Properties of the Elements* published by Sargent-Welch Scientific Company.
8. T. A. Grant, H. Shen, J. R. Flemish, and M. Dutta, *Appl. Phys. Lett.* **60**, 1453 (1992).

XVI. Distribution List

Mr. Max Yoder Office of Naval Research Electronics Division, Code: 314 Ballston Tower One 800 N. Quincy Street Arlington, VA 22217-5660	3
Administrative Contracting Officer Office Of Naval Research Resident Representative The Ohio State University Research Center 1960 Kenny Road Columbus, OH 43210-1063	1
Director, Naval Research Laboratory ATTN: Code 2627 Washington, DC 20375	1
Defense Technical Information Center Bldg. 5, Cameron Station Alexandria, VA 22314	2